CHARACTERIZATION OF TE SECONDARY PHASES IN CADMIUM ZINC TELLURIDE USING IR TRANSMISSION MICROSCOPY

By

W. GITAU MUNGE, II

A thesis submitted in partial fulfillment of

the requirement for the degree of

MASTERS OF SCIENCE IN MATERIAL SCIENCE AND ENGINEERING

WASHINGTON STATE UNIVERISTY

School of Mechanical and Material Engineering

MAY 2010

To the Faculty of Washington State University

The Members of the Committee appointed to examine the thesis of W. Gitau Munge, II find it satisfactory and recommend it be accepted

_____

Kelvin G. Lynn, Ph.D., Chair

_____

David P Field, Ph.D.

_____

Amit Bandyopadhyay, Ph.D.

_____

Indranath Dutta, Ph.D.

ACKNOWLEDGEMENTS

First, I would like to thank Dr. Kelvin for taking me under his wing and giving me the opportunity to complete this program. His unique way of motivating me has led me to this final success. He encouraged me to dig in deep and investigate all options and this launched the motivation which fueled the completion of this thesis. To my committee members, you have all provided the support without which I would have never made it this far. To my CMR coworkers, Raji Soundararajan, Santosh Swain, Amlan Datta, Chandra Minnal, Manchanahalli S Rohan Rao, Daniel Trump, and Kelly Allan Jones, you have been my support group and my sounding board, not to mention my inspiration. Raji S., you have pushed me through this journey and I am honored to have worked with you. Special thanks goes to other members of CMR including: Abraham E. Jones, Roger Saunders, Becky Griswold, Yuliya A. Bunakova, Marc Weber, and Dennis Solodovnikov. To my dear girlfriend and close friend Sarah Stanton, your effort can never go unnoticed. Your outstanding mastery of the English language has provided the core of this thesis and has made me a better writer. Finally, I would like to thank my family and friends all over the world for their support, blessing, prayers, and love, not just in the course of this accomplishment, but others met and others to come.

This Thesis was sponsored by the Savannah River National Laboratory, contract LLC AC695380 & US department of Energy, contract DE-FG52-06NA27497 and DE-FG52-08NA28769.

CHARACTERIZATION OF TE SECONDARY PHASES IN CADMIUM ZINC TELLURIDE USING IR TRANSMISSION MICROSCOPY

Abstract

by W. Gitau Munge, II

Washington State University

May 2010

Chair: Dr. Kelvin G. Lynn

CZT is considered a competitive room temperature semiconductor capable of detecting high-energy radiation such as X-rays and gamma-rays. However its maximum efficiency has yet to be attained due to extended defects such as twins, grain/multi boundaries, and other secondary phases present in a grown ingot. One of these secondary phases present in designed detectors is Te secondary phases, which is the focus of this study. Te secondary phases fall into two categories: Te precipitates and Te inclusions with average diameter of 1-75um. A fraction of a void may surround a visible Te inclusion. Otherwise observed isolated voids and Te inclusions seem present in most CZT detectors as well. These Te inclusions and voids serve as impurity sinks capable of trapping electrons. We have employed IR transmission microscopy to study Te inclusions. This study assumes that all lone Te inclusions and voids as well as inclusions surrounded by voids are simply "Te inclusions". We then found that Te inclusions with average

diameter >4um are major inhibitors of electron mobility-lifetime (MT) in a CZT detector. Te inclusions, however, are considered a litmus test which confirms favorable stiochiometry. A favorable stiochiometry can produce a better compensation scheme necessary in improving detectors' resistivity and MT value. This is because their shape, size, and distribution (SSD) make a reliable pattern for projected detector quality. While some CZT ingots grown at CMR with no count of Te inclusions have failed to produce grade radiation detectors, those with density ratio of Te inclusions with average diameter <4um to that of all counted inclusions expressed in percent ($Den_{<4um}/Den_{Total}$ %) > 99%, have recorded MT value close to 10^{-2} cm^2/V. Based on this information, a correlation between Te inclusions' SSD and MT values of detectors within an ingot and on various ingots was established. The variation of volume % of these detectors was further established to strengthen the correlation in cases where ($Den_{<4um}/Den_{Total}$ %) matches and/or is relatively close. These correlations are only relevant if the crystal purity and high resistivity ($>10^9$ Ω.cm) are produced.

TABLE OF CONTENTS

Page

LIST OF TABLES

TABLE

LIST OF FIGURES

FIGURE

LIST OF GRAPHS

GRAPH

LIST OF CHARTS

CHART

DEDICATION

This thesis is dedicated to my Nephew, B. Munge Wachu.

CHAPTER 1

I Introduction

Today Cadmium Zinc Telluride (CdZnTe/CZT) as a high Z semiconductor material is used in a broad range of applications: from medical imaging, industrial process monitoring, national security and treaty verification, environmental safety and remediation, to basic science [1]. In comparison with detectors such as Germanium detector, which functions at cryogenic temperature [2], CZT is currently operated at room temperature with high detection efficiency [1]. It is built to detect and perform energy-dispersive spectroscopy of high-energy radiation such as X-rays and gamma-ray [1].

However, the response of a CZT detector to X-rays and gamma rays is potentially degraded by factors such as secondary phases, grain boundaries, dislocation density, and foreign impurities present in the detector [3&4]. Ongoing studies at Center for Material Research (CMR) at Washington State University suspect Tellurium (Te) secondary phases in CZT detectors (among other factors) as both a positive and negative factor in the advancement of better-performing CZT detectors. Possible secondary phases include Te, Zinc (Zn), and Cadmium (Cd) "precipitate" or "inclusions" and other defects [4]. Recently, proceedings from Savannah River National Lab (SRNL) has identified Te secondary phase and/or voids as the majority defect on CZT detectors. [5]. Based on A.E. Bolotnikov *et al*. phenomenological model, Te secondary phases inhibit electron mobility in CZT detectors [6]. This decreases bulk resistivity due to partially depleted layer hence lowering electron mobility-lifetime (MT) of a detector. Though according to data from processed detectors at CMR presented in this thesis, a controlled presence

of Te "inclusions" would show higher MT values and subsequent *improved* spectroscopic performance of a detector.

Concerning experiments on MT values of detectors from crystals grown at CMR, Size Shape and Distribution (SSD) of Te secondary phases are investigated via IR Transmission Microscopy with an average wavelength of 881nm. SSD analysis will show that detector quality depends on Te secondary phases' SSD. The presence of Te secondary phases in a detector is never a positive factor, but it is an assurance that a favorable stiochiometry took place. A demand for excess Te in CZT growth necessary to supply significant charges for better resolution is consistently reflected in formation of Te secondary phases [7].

Te reacts with Cd and Zn to form CZT. Te_{Cd} act as a deep donor, which pin the Fermi-level close to the center of the detector's band-gap [7]. This results in increased resistivity necessary to the production of grade quality detectors. Net cadmium vacancies (V_{Cd}) are essentially compensated by In to form more stable shallow level acceptor (A-center) [8]. This further contributes to an effective compensation scheme which strongly favors production of high-resistivity CZT detectors with better resolution to both holes and electrons. A standard measure of dopants, however, is significant as oversaturation of these dopants in an ingot results in surplus charge that undermines the detector's charge carrier transport mechanism. This defined role of Te inclusions as a litmus test for stiochiometry and subsequent compensation scheme is verified in various grown samples from CMR which exhibited no Te inclusions; they measured low resistivity, trivial and/or nil MT value, high leakage current, and poor resolution to electrons and holes (little to no peak to valley (P/V) ratio).

These inclusions in CZT detectors have thus far been unpredictable and uncontrollable. Past evaluation of Te inclusions' SSD has failed to predict better grade CZT detectors for

spectroscopic performances in grown ingots. Past compensation schemes of earlier dopants used to grow CZT at CMR failed to produce a standard measure of resistivity $>10^9$ Ω.cm. Fiederle *et al*. claims that a minimum of $>10^9$ Ω.cm is necessary for a high grade detector [8]. Moreover, detectors from various ingots grown at CMR that were impurity-rich and/or grown with different dopants did not show sufficient variation in MT values to allow for establishment of a correlation between MT values and Te inclusions' SSD. A standardized evaluation system of MT values combined with insufficient information about the cause and effect of Te secondary phase as an impurity sink have thus far inhibited a better interpretation of the link between Te inclusions' SSD and detector properties.

According to Tewari *et al.*, "experimental measurement of particle/grain size distribution is useful to verify the theoretical models for microstructure evolution [9]." Given this, and the fact that an earlier mapping probe "had much wider excitation areas (200-400 um diameter) than typical size of Te inclusion," small-sized Te inclusions <20 um were yet to be thoroughly characterized [6]. Te secondary phases include Te precipitates and inclusions. "Te inclusions are formed by melt-droplet capture near the growing interface at the growth temperature," while Te precipitates are a result of "retrograde solubility of native point defects during the cooling process of the solidified crystal." [1]. Ruston *et al.* proposes that the average diameter of a Te precipitate is between 10-30nm, while that of Te-rich inclusions is between 1-50um [10]. Te secondary phases that have been observed from IR images at CMR are between 1-75um. Thus, this study proposes Te inclusions, but not precipitates, as the subject of interest. These observed inclusions, however, ignores the fact that inclusions are intertwined with void an instead classify them as simply "Te inclusion." In support of this assumption, studies at SRNL found no contrast

between Te secondary phase and its surrounding void; the conductivity of the two was relatively uniform and higher than that of CZT bulk [5].

A collective analysis of other CZT detector parameters, such as leakage current, resistivity, structure, composition, growth rate, cool-down period, purity, surface preparation, and contacts, is necessary, in conjunction with Te inclusions' SSD analysis. Study and better comprehension of these parameters can result in improved predictions for progressive spectroscopic performances of detectors grown at CMR-WSU. This further aides in supporting correlations between Te secondary phase's SSD and its electrical properties such as MT values and P/V ratio for better resolution. MT values are estimated from equation 1:

$$\mu\tau_e E = d; \quad MT = \mu\tau = \frac{d}{E}\ ; units\ cm^2/V \qquad \text{Equation 1}$$

where E stands for measured electric field in a given detector. In most cases, a high MT value ($>10^{-2}$ cm^2/V) results: first in better visibility of 14KeV peak that shows how effective a detector can effectively resolve an electron; and then a higher P/V ratio for better resolution of both holes and electrons.

In simple terms, the main focus of this research is to correlate the MT values of varied single crystal detectors from different ingots grown in identical conditions (uniform use of dopants and raw materials, growth rate, temperature, and cool-down period) to SSD parameters of Te secondary phases present, while considering other parameters such as the resistivity and purity of the ingot in question.

This thesis will show that a single-crystal detector with resistivity of $>10^9$ Ω.cm and a low level of impurity have a projective correlation between Te inclusions' SSD and MT values. In

the case of detectors cut from the same ingot, the size-range distribution of Te inclusions which increases from the tip to the heel of the ingot, correlate with decreasing MT values and resistivity. In case of detectors from various ingots, it is the density ratio of Te inclusions with average diameter <4um (or sometimes <6um) to that of all counted inclusions expressed in percent ($Den_{<4um}/Den_{Total}$ %) which is pertinent to MT values. $Den_{<4um}/Den_{Total}$ > 99% will give a MT value close to or $>10^{-2}$ cm^2/V; a population of which $Den_{<4um}/Den_{Total}$ is greater than 80% will give a MT value $>2*10^{-3}$ cm^2/V. Furthermore, it will be demonstrated that an even and a narrow distribution of inclusions will also lead to a higher MT value, although this relationship is less clearly defined. Finally it reclaims that a standard presence of Te inclusions in a detector acts as a litmus test confirming favorable stiochiometry and subsequent better compensation necessary to improve detector's resistivity and MT value. Tailoring of smaller sized Te inclusions with average diameter <4um contributes a much smaller percentage (volume %) of entire volume of the detector and instead help to maximize the detector's properties, i.e., MT value.

II Background Information: Parameters and crystal growth overview

CZT crystals grown at CMR using the Modified Vertical Bridgman Method (MVBM) are partly homogeneous all around the ingot. Its growing direction, which start from the tip of the ingot, is given in figure 1. $Cd_{1-x}Zn_xTe$ is the stiochiometric name for CZT, where x stands for overall percent value of Zn concentration in CZT composition. It has been reported that most ingots grown with x value > 0.07, makes the crystal a p-type material [11]. But, addition of

dopants to a grown ingot at CMR may make a crystal less p-type and instead helps to pin the Fermi level in its rightful position.

In any given ingot, especially unpolished cut slices, one can easily see twins and grain/multi boundaries. Cracks, voids, wires, and pipes can be seen as well (in exclusive cases and/or in low percent). A deviation of materials composition and properties from grain to grain in an ingot due to these extended defects weakens or alters possible correlations between a sample's MT and its Te inclusion SSD's results [4]. Hence, it is necessary to review the ingot growing process and the source of the above-named extended defects.

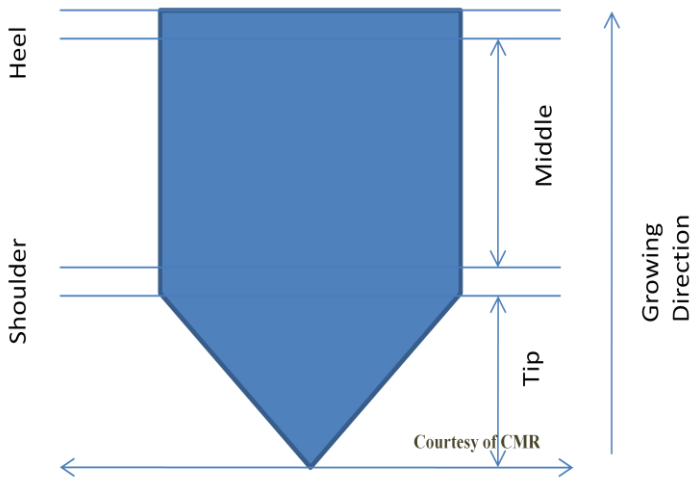

Figure 1: Schematic image of CZT ingot.

CG65 Ingot, (+/-) a factor of 2			
Name of Element	Tip	Mid	Heel
Cd	*Matrix*	*Matrix*	*Matrix*
In	*1200*	*1900*	*11000*
Zn	*5.8 %*	*5.7 %*	*3.0 %*
Te	*Matrix*	*Matrix*	*Matrix*

Table 1: Partial GDMS Report for CG65 in parts per billion (ppb). **[Courtesy of GDMS report]**

Beside applicable dopant such as indium (In), the main raw materials used in CZT growth include: CdTe, ZnTe, Zn, and Te. As seen in Table 1, the composition of the ingot varies significantly between the tip and the heel. In general, one would expect the gravitation of this

ingot in the furnace during "vertical" crystal growth to favor settlement of high density materials at the bottom or the tip of the crystal boule. According to the Glow-Discharge Mass Spectrometry (GDMS) ingot report for CG65, the heel has a higher concentration of In [12] (see table 1).

An important factor that, which is the causes of this disorder in the variation of existing CZT's native elements or impurities concentration, is the segregation coefficient. Particle segregation of separate elements from raw materials, dopants, and foreign materials present during CZT growth and cool-down tends to occur according to particles' SSD and other properties inherent to their composition [13]. The segregation coefficients for Zn, In and other impurities have been studied [1&14]. Given a complete mixing of particles in the ampoule, segregation coefficient k_0 is derived from the Scheil equation:

$$C_s(x) = k_0 C_0 \left(\frac{1 - \mathrm{x}}{\mathrm{L}}\right)^{k_0 - 1}$$

where $C_s(x)$ is the impurity concentration at point x, which is the distance from the solid ingot tip (where the growth of the ingot starts). L is the ingot length from its tip to the heel, C_0 is the pre-growth impurity concentration, and k_0 is the impurity segregation coefficient [1&14]. This equation can also be used to calculate k_0 for In given in table 1. Understanding of dopant or impurity segregation mechanism is necessary during crystal growth as it results to favorable growth mechanism that increases solubility. This lowers formation of defects such as precipitates and oversaturation of dopants [15].

CMR uses MVBM with a stationary furnace and multi zone-temperature profile to heat the ampoule containing the raw materials and dopants. These zones are first set at a fixed

temperature >1180 °C to superheat the ampoule. The growth rate of most CZT-grown ingots at CMR ranges from 0.5mm/hr - 4mm/hr. A positive segregation coefficient that is greater than 1 results in higher concentration of Zn at the tip [14]. Zn decreases as growth progress as it tends to settle in the solid phase rather than the liquid phase [14]. A standard gradient, which is imposed throughout the growth process, is first applied on the first two zone-temperature profiles according to the growth direction. The first zone-temperature profile is dropped to a minimum temperature, while the second zone maintains a relatively higher temperature with the gradient. The rest of the zone-temperature profile remains at the maximum imposed temperature until the ingot fraction at the first zone solidifies. After the ingot is fully grown and solidified, the cool-down process begins. This process can be either fast or slow, using retrograde quenching, horizontal gradient, and/or regular cool-down.

The initial melting point of the CZT (which decreases with decreasing Zn concentration), is estimated to be a temperature greater than that of the second reduced temperature profile but less than the imposed maximum temperature. Hence nucleation and growth rate are both minimized in a region within and surrounding the tip, but they increase towards the shoulder and towards the heel. Note that the melting point of CdTe is 1092 °C and that of CZT is 1102 °C (with a 10 % standard error) [16]. The variation of the ingots melting point from tip to the heel and temperature difference at zone interfaces leads to instantaneous growth rate. Hence the ingot nucleates homogenously in stages. It also grows uniformly in stages as the rate slows down in between interfaces. This leads to formation of multiple grains throughout the ingot. The tip has a higher percentage of multi-grained crystals with higher Zn concentration, which raises the bulk resistivity [17&18] inhomogenously.

From the GDMS report discussed earlier and the fact that Zn has a segregation >1, one can infer that In, which increases in concentration towards the heel, have a segregation coefficient that is less than one. Accordingly, it tends to settle in the liquid phase rather than the solid phase; since the zone within and around the heel is the last region in the ingot to solidify, it is logical that it should have the highest concentrations. On the contrary, Li. *et al* reported that In has a segregation coefficient of 1.3 (when Zn concentration, x, was 0.1) which is close to that of Zn [11]. This report remains suspicious and fails to correlate with GDMS report for 0.1 Zn concentrated CG65 given above. If that were the case, then the part having homogenous Zn distribution in $Cd_{0.9}Zn_{0.1}Te$, would also have a homogenous In distribution.

Given the function of dopants, which is to compensate for V_{Cd} or Te_{Cd}, regions of high resistivity can change in relation to beginning concentrations of dopants. Presence of multiple grains fluctuate the distribution of impurities in the ingot; concentration of impurities is superior at the grain boundary, but more evenly distributed inside the grain of an ingot [14]. This changes the resistivity of cut samples or detectors, hence affecting their consistency and energy resolution of x-ray and gamma-ray. The tip of the ingot tends to have a higher resistivity, but poor 122-KeV peak due to deficiency of Te_{Cd}(s) and a high concentration of V_{Cd} resulting in poor transportation of both holes and electron (poor compensation scheme) [14].

Terterian *et al* suggest that the heel of the ingot, with low Zn concentration, measures a relatively lower resistivity [14]. As for Te-rich grown ingots, high concentrations of Te precipitates and, at times, high concentrations of inclusions at the heel result in poor detector resolution during testing. Te-rich precipitates increase the dark current of the detector in-test as their low band gap, 0.33eV, easily ionizes even at low voltage supply. Te precipitate or

inclusion sites trap electrons and holes of detectors in-test, resulting in a poor signal peak [6]. It is then logical that the region around the shoulder and above the shoulder may measure higher resistivity relative to the heel and subsequent good ^{57}Co spectrum (for better resolution). With a given crystal grain, Zn concentration is relatively uniform in the mid section of the ingot, as is the distribution of Te secondary phases. The extent of the region with higher resistivity and better resolution may vary from ingot to ingot, yet it is conclusive that the highest quality detector is to be found in regions within the shoulder and just above [13].

Some major factors that affect the spectroscopic performance of CZT detectors include transformation rates (mainly growth rate), reaction and composition, and the cool-down process. The unexpected intrusion of cracks, pipes, wires, twins and grain/multi boundaries, besides a high yield of dislocations and Te secondary phases [19], alter the material and device properties as well.

The region affected by a crack, whose average width is approximately 1-10 microns, extends as far as 10 mm [20]. This may result in high current leakage in any region (10x10) mm^2 bordering the crack. This effect relates to the fact that impurities such as carbon from used graphite lid and melted Zn (which are metallic in nature) during growth, may have infiltrated the crack hence increasing the leakage current. This effect lowers the resistivity of the region under discussion. It is also possible that the gold solution which is deposited around the crack for better contact of the detector in test, did infiltrate the crack, hence short-circuiting current flow leading to creation of dark current. This effect should drop the MT value. The fact that these extended defects (independent of Te inclusions, which further aggravate their negative effect on a CZT detector), can be isolated as the cause for a drop in MT value suggests that it is necessary

to study a single crystal that is free from them. These defects act as foreign impurity avenues that weaken the CZT ideal compensation scheme and hence drop the MT value. In the end, this weakens the correlation between Te inclusions' SSD and measured MT value.

A wire is a densely packed string of Te precipitates that may or may not continue across grain boundaries, while a pipe runs through and parallel to the growth axis in irregular intervals [20]. Wires and pipes tend to be present in ingots that are multi-grain dominated, but not in single crystals. The impact of wires and/or pipes mimics that of a micro-crack [20].

Generally, the impact of a wire, crack, pipe, or grain boundaries affects electric field distribution within and around these defects [21]. This may be a result of inhomogeneous CZT composition and bandgap variation and also, to a limited extent, a result of partial detector depletion which degrades a detector's electric field. Effective compensation of impurities is weakened by the generation of various sites which attract other known or unknown foreign impurities, altering a detector's in-test resistivity or spectroscopic performance [18,22,&23]. This then necessitates the importance of studying single crystals detectors that are relatively free from most of these extended defects. This may eventually rule out a stronger correlation between Te inclusions' SSD and measured MT value (and sometimes P/V ratio).

Furthermore, grain boundaries act as low energy sites, which attract Te secondary phases [20]. Excess Te, with melting point ~ 450 °C, is highly diffusive at CZT growth temperature > 1050 °C with a small temperature gradient. This limits the number of Te atoms from melt-droplet (due to growth instability), which will reach a critical size [24]. Growth of these Te solvents, which nucleated as a liquid as the ingot grew, can later increase during cool-down resulting in transformation of Te inclusions [24]. The formed inclusions are also intertwined

with void fractions generated at phase-separation temperature (see figure 2); Te inclusion or precipitate volume fractions drop at phase separation temperature and vacancies are generated with increasing elastic interaction as fractions of these voids increase [25]. The population of Te secondary phases and void, though, is higher within a grain boundary.

Growth of Te precipitates relates to formation of Te interstitials and other intruding point defects at low-energy sites, especially within a grain boundary [20]. Pressure is applied on the surrounding CZT as Te inclusions grow [20]. Depending on the size of grown precipitates or inclusions and other impurity matrix avenues (including, but not limited to, Te) which relieve the pressure from the molten Te, the total exerted pressure may exceed a threshold value and generate dislocations [20].

Te and vacancy mobility is reported to affect growth kinetic, volume fractions and morphology of Te "inclusions" /precipitates and voids [25]. Te controlled diffusion growth has low Te concentration, while vacancy controlled

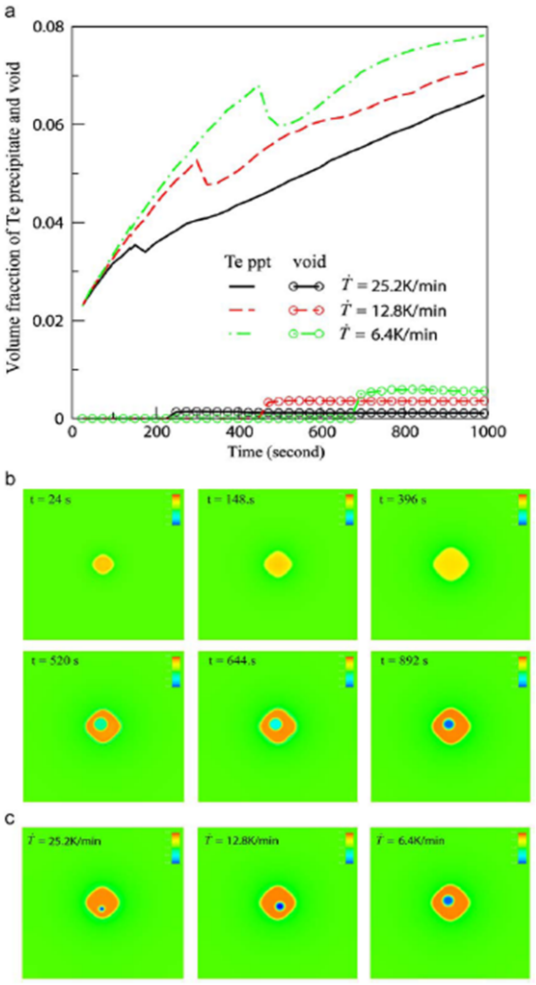

Figure 2: The effect of cooling rate on growth kinetics as the system cools from 1000 to 900 K with three cooling rates. (a) Volume fraction of the phases as a function of time. (b) The evolution of Te precipitate and void for cooling rate T`= 6.4 K/min. Red ~ precipitate; blue ~ void (c) Final morphology of precipitate and void at t = 892 s for three cooling rates.

Courtesy of S. Hu et al.

diffusion growth has high concentration of Te. While Te controlled diffusion growth has high vacancy mobility, vacancy controlled growth has low vacancy mobility. Void formation at phase transition temperature are persistent in Te precipitate with low Te concentration and can eventually grow if its size is greater than that of critical nucleus, otherwise it shrinks [25]. Overall, Te precipitates/inclusions migrate towards regions surrounding the low-energy grain boundaries and this has been confirmed at CMR in that regions in close proximity to a grain boundary tend to have a low percent of Te precipitates or inclusions [see CG92 results].

Both Cd-rich and Te-rich grown ingots maintain a high Zn concentration at the tip. In the case of Cd-rich grown ingots, a significant decrease of Te secondary phases and formation of Cd inclusions and/or vacancies can easily ruin the detector. However, a standard measure of excess Cd could standardize or control the amount of excess Te in CdTe charge (CdTe charge in CZT growth at CMR are artificially Te-rich) during growth without forming into Cd inclusions; Cd reacts with Te resulting in formation of CdTe during cool-down, which is also integrated into the CZT matrix. This can further improve the detector's spectroscopic performance. Furthermore, the concentration of Te inclusions throughout the ingot would decrease significantly. This can result in improvement of detectors extracted even at a region just below the heel (and increasing overall yield) as resistivity increases, and subsequently, its MT value. Contrary, a decrease of $Te_{Cd}(s)$ may affect the capability of these detectors to resolve characteristic radiation peaks of ^{241}Am and ^{57}Co [7]. This deficit of $Te_{Cd}(s)$ can also result in low resistivity and subsequent poor MT value.

CHAPTER 2

I The Role and Effect of Te: The Impact of Te secondary Phases in CZT

The intrinsic defects associated with CZT growth are unavoidable. These defects include Te_{Cd} and V_{Cd} among others. V_{Cd} and Te_{Cd} are considered both shallow and deep donors [Figure 3&4]. Other defects include deep donors $(Ge, Sn, V)_{Cd}$ [26]. Shallow donors from group IIIA include $(Al, Ga, and\ In)_{Cd}$ and $(Cl, Br, and\ I)_{Te}$ from group VIIA. Shallow acceptors include $(Li, Na, and\ K)_{Cd}$ from Group IA and $(Cu, Ag, and\ Au)_{Cd}$ from group IB. $(N,P, and\ As)_{Te}$ from group VA can be classified as both shallow donors and acceptors [26]. Stabilization of the Fermi level depends upon the complete compensation of shallow and deep donors and acceptors [8&26]. The list of known energy levels in Cd-based compounds is given in figure 4 [26].

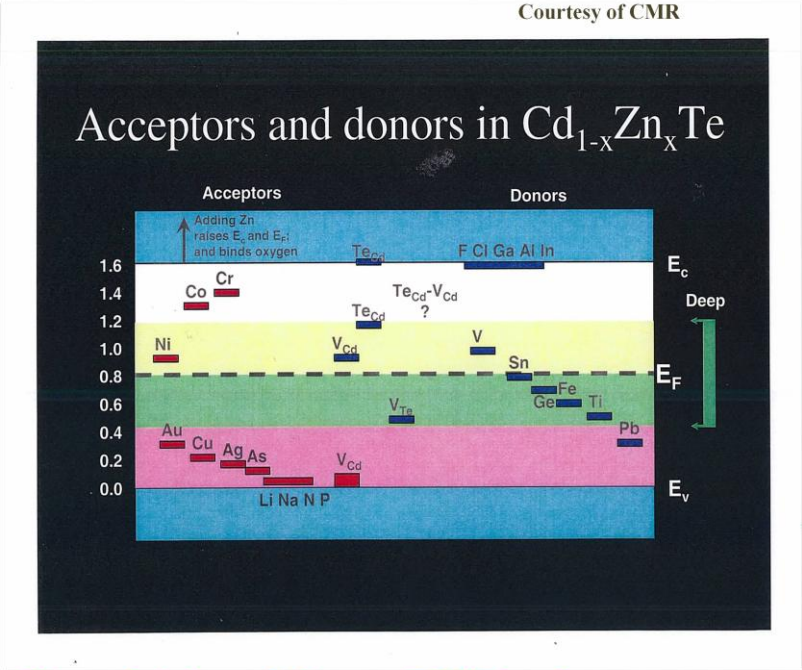

Figure 3: Schematic image of CZT bandgap

In addition, the essence of Te inclusions' SSD projects the nature of large inclusions that trap electron clouds and overturn the effect of a well-compensated scheme. Fluctuation in

inclusions' size can result in spatial variation of the ingot and this can negatively affect the bond length between CdTe and ZnTe as well as their energy bandgap [27].

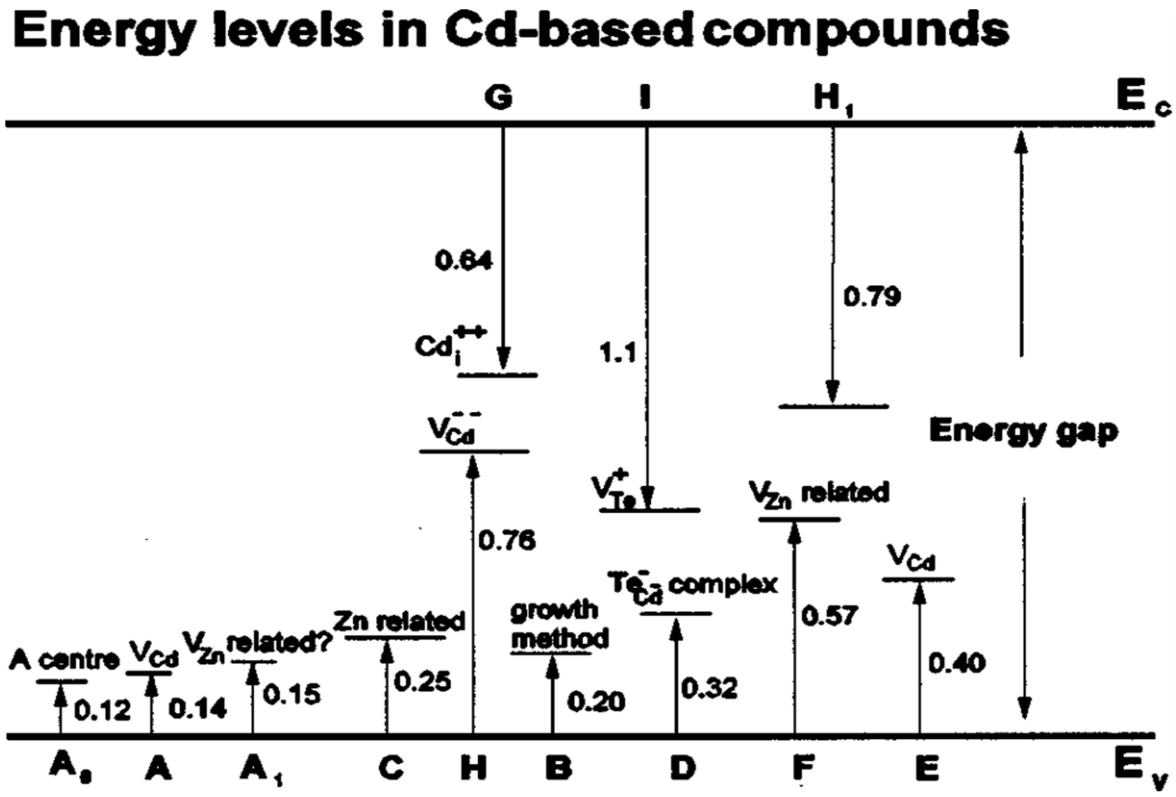

Courtesy of A. Castaldini *et al* [24].

Figure 4

The presence of Te inclusions is in some ways paradoxical: they lower the MT value of the sample, but also act as litmus test that confirms favorable stiochiometry and subsequent compensation scheme necessary in improving the detector's spectroscopic performance. A lack of Te inclusions can infer excess Cd in the ingot, resulting in the formation of V_{Cd} and Cd inclusion that attract extra charges and severely lower resistivity (it has been determined that star-like inclusions that are mostly Cd-rich can easily ruin a detector). Thus, Te-related inclusions and defects are necessary for the moment as a means of assuring the proper balance of starting materials. It is however the size, shape, and distribution (SSD) of remaining inclusions

which affect the spatial variation of CZT ingots. Data acquired from Te inclusions' SSD results can lead to calculations of a standard stiochiometry that could optimize CZT detector functionality. This thesis found that Te inclusions of limited size <4um and low population density define a favorable stiochiometry and competitive compensation scheme that contributes to the production of high-grade detectors.

According to S.A. Awadalla *et al*, a naturally triangular inclusion will take on a hexagonal form during the cooling process if the Te concentration is high enough: "The saturation level of the trapped solvent is likely to control the shape of the inclusion. In <111> oriented growth, the trapped inclusion is initially triangular but when the crystal cools, oversaturated inclusions will precipitate CZT at the corners, effectively infilling them and generating a final hexagonal shape [28]." SEM image given in figure 5 at Pacific Northwest National Laboratory (PNNL) [25] reflects Awadalla's claim. However, this SEM image does not show a fraction of void that is usually coupled with Te secondary phase [25].

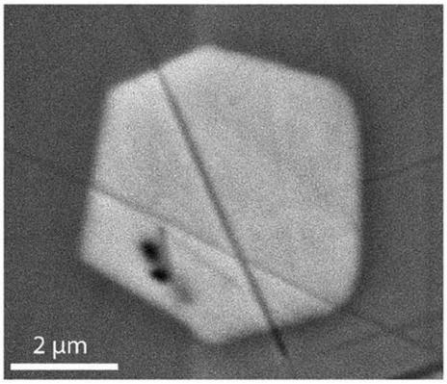

Figure 5: SEM image of Te secondary phase

Courtesy of S. Hu et al.

Note that the perceived shape on a 2D plane at CMR of Te inclusion may be different than the *actual* shape. Therefore, even if Te concentration of a given inclusion shape could be determined, the knowledge remains hypothetical as the true shape of the inclusion and/or cannot be confirmed. If a system could be established to reliably correlate the shape of an inclusion with the concentration of Te within that inclusion, then future ingot growths could be monitored for the shape of their inclusions for the purpose of determining Te concentrations.

On the other hand, the size and distribution of Te inclusions can be explored in light of thermo-migration. Te inclusions migrate from cold to hot zones within the CZT. A fraction of CZT within the zone-interface dissolves on the hotter side of Te inclusions and later redeposits on the colder side [29]. The importance of this mode of migration does not disappear during a regular cool-down process, where Te solvents transform into full-grown Te inclusions, but it does slow down. Depending on the speed of the cool-down, the size and distribution of Te inclusions can vary significantly. This is demonstrated in CG78 and CG80, which were cooled with an imposed gradient of 100 °C, but during different periods. The subsequent CG59, 92, and 93 were cooled with no gradient, but their cool-down time was also varied. In all five cases, the variation in the cooling method/time resulted in wide-ranging Te inclusion SSD that affected electrical properties of each ingot.

A sample extracted from the edge of CG64 is of special interest because it exemplifies the highest MT value of detectors processed at CMR. This sample contains an ideal Te inclusion' SSD value with an optimum spectroscopic functionality in a CZT detector. As shown in figure 6, the distribution of Te inclusions is uncluttered and almost evenly distributed. This detector had a

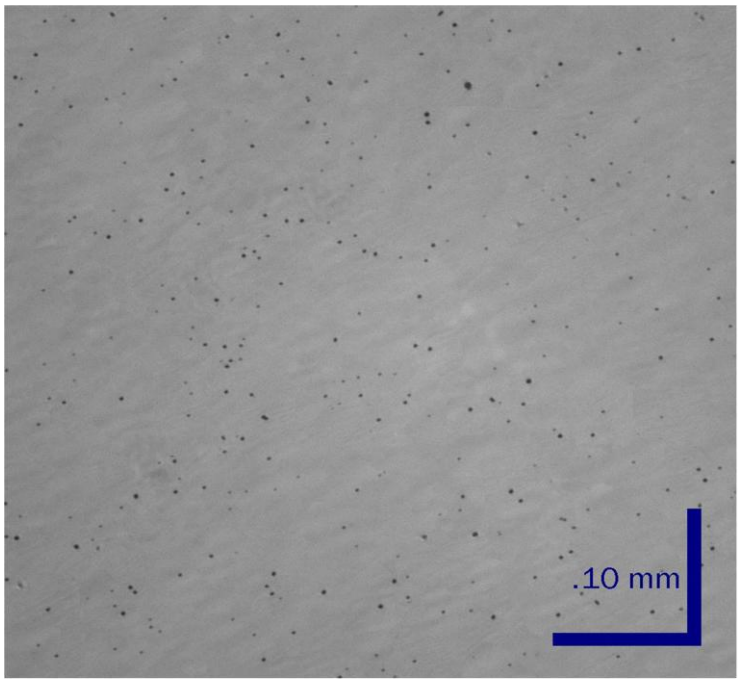

Figure 6: Single DOF image from CG64 Edge sample. The percentage of Te inclusion with average diameter <4um is almost 99%

narrow Te inclusion size range with a diameter range of 1-10um, the majority being under 4um. Other values such as sample thickness, AOI, and Te counts are given in Graph 1.

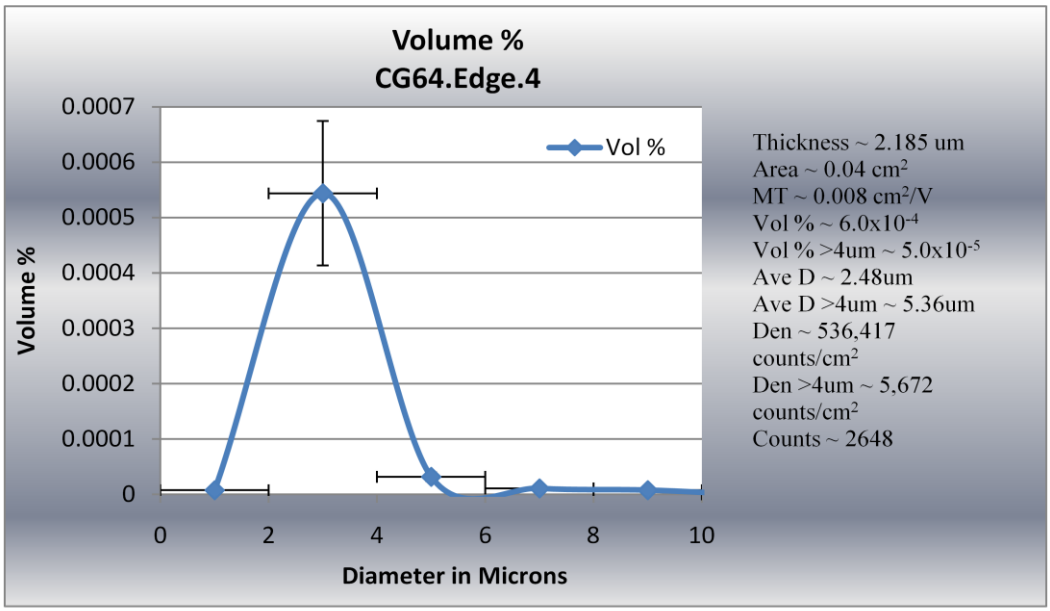

Graph 1:

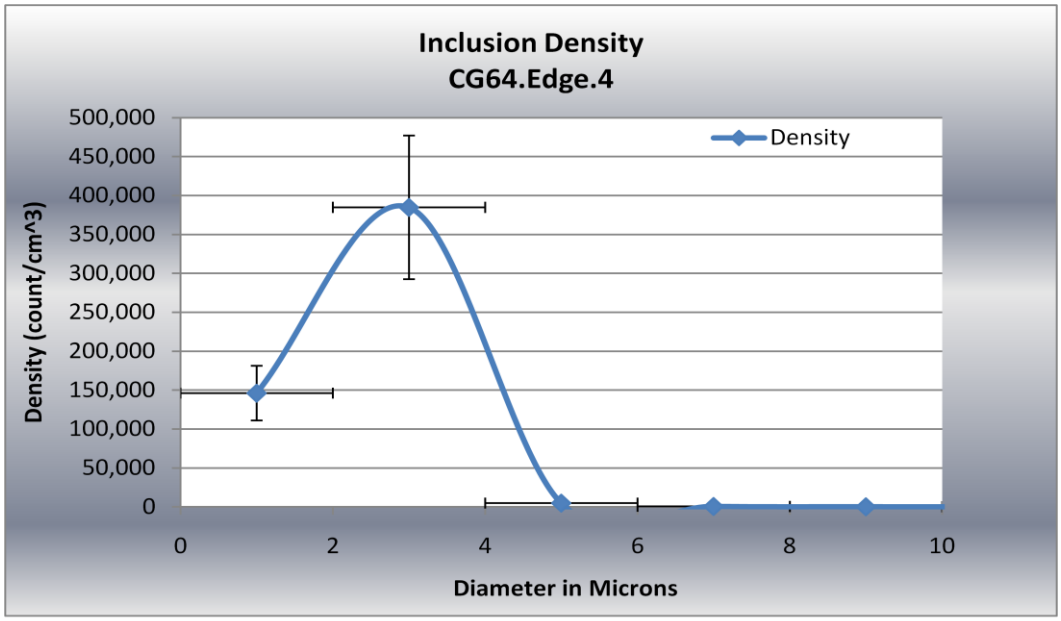

Graph 2:

Graphs 1 and 2 further demonstrate that the majority of Te inclusions are within a diameter range of 1-5 um. The two graphs show that the high population density of these Te inclusions has less effect towards Te inclusions' volume % present in the detector. This is an ideal SSD of Te inclusions, which has long been the objective of ongoing efforts to optimize CZT performance at CMR. Overall, the Te inclusion volume % of $6x10^{-4}$, the average inclusion diameter of 2.48um, high resistivity, and a relative absence of impurities in this detector are the main contributing factors that give the high MT value of 0.008-0.01 cm^2/V (given a standard error of almost 24%).

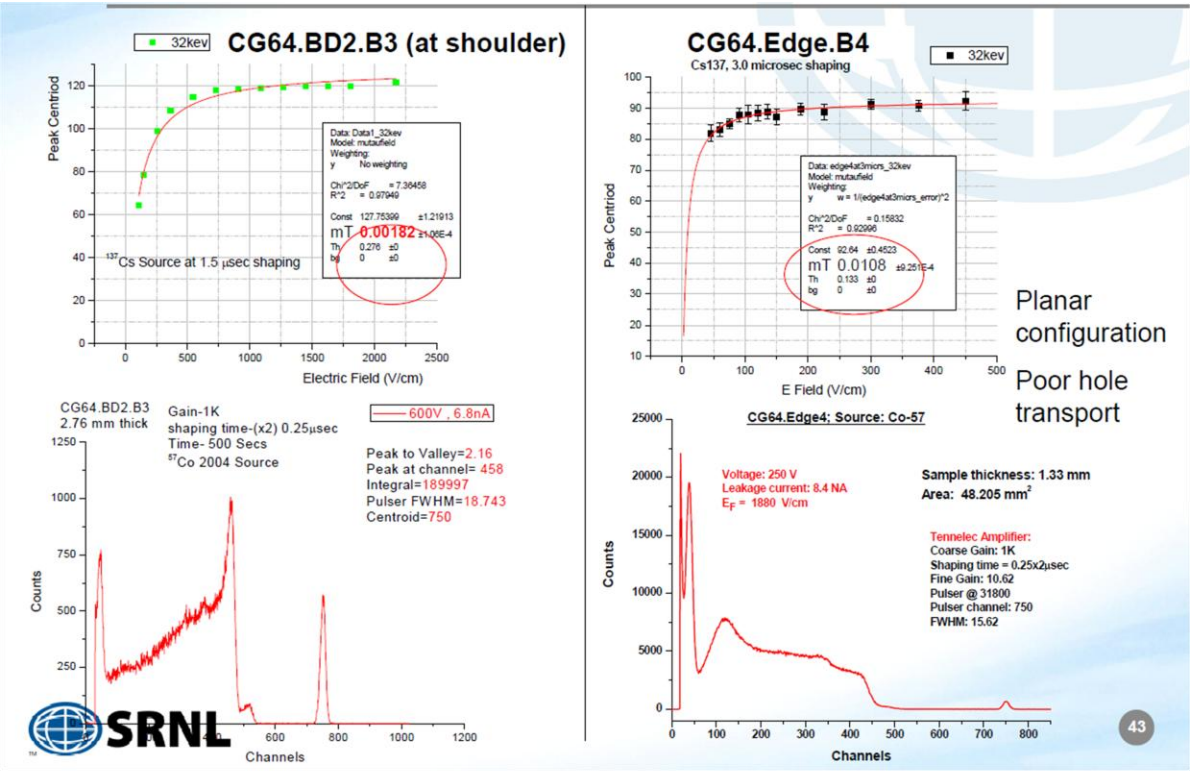

Figure 7: MCA analyses for CG64 detectors. MT measurement ~ CG64.BD2.B3 fitted curve is broader than that of CG64.Edge.B4; Characteristic radiation peak of 14KeV and 122KeV in ^{57}Co source ~ CG64.BD2.B3 can resolve both holes and electrons and CG64.Edge.B4 detector can only resolve electrons. **Courtesy of CMR**

Figure 7 (MCA results and analyses by CMR on CZT detector on SNRL presentation) further analyzes the effect of Te inclusions in CG64.Edge.B4 detector and CG64.BD2.B3, in which ~ 70% of total population density of Te inclusion, had an average diameter >5um. The curve of CG64.Edge.B4 sample is sharp and its MT value is greater than that of CG64.BD2.B3 sample by a factor of ~ 10. CG64.Edge.B4 detector, however, is a poor hole transport; it fails to resolve both holes and electrons as 122KeV gets broader and falls almost flat. A P/V ratio of 2.16 given by CG64.BD2.B3 sample explains how effective this detector can resolve both holes and electrons. This is a strong case which exemplifies the significance of Te inclusion, yet arguably it explains how difficult it is to grow ingots that can produce both competitive MT value and high resolution of not only electrons, but holes as well. Alternatively, the positive impact of Te secondary phases (inclusions) is maximized if detectors from grown CZT ingots meet or better the values shown in the CG64 edge sample. This could be accomplished if a balance could be found in applied stiochiometry, compensation schemes and cooling methods.

CHAPTER 3

I Sample Naming

A general name for CZT crystal ingot starts with prefix CG, which stands for Crystal Growth, followed by a numerical number, which sums the total grown ingot. I.e., CG69 is the 69th crystal grown ingot (figure 8) at CMR. In reference to the sitting position of an ingot in the ampoule, 4 equally spaced points (A, B, C, & D) form the boundaries of the quadrant, Q. Line AC would then be perpendicular to line BD and four Qs around the ingot include: AB, BC, CD, and AD. A slice may then be cut along section AC or BD (axial cut). It can also be cut radially from a region around the shoulder, the mid, the tip, or the heel of the ingot. Radially cut slices, starting from the tip, take the name R1, R2, R3, etc. The slice given in figure 8 is an axial cut along section BD. Then, samples fall within standard rows A-G, and columns fall within standard columns 1-5, hence giving each detector a prefix such as A2, A3, A4, etc. An extended name for any sample can then read CG69.BD2.A2 where CG69 stands for the identification number of grown ingot, BD2 represents the section from which the slice was taken and its assigned number (if more than one slice was cut), and A2 stands for unit sample/detector.

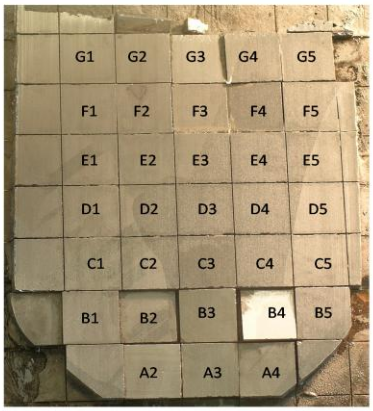

Figure 8: CG69 slice and sample naming

II Sample Selection and Expectation

As discussed earlier, a standard procedure of sample selection for this research incorporates a collective database of as-grown ingots and respective samples' parameters and statistical analyses of detector performance in order to establish a correlation. First, these ingots were selected: CG51, CG58, CG59, and CG67. Each of these ingots were grown with uniform measurements of raw materials and dopants, as well as the same temperature in respective mixing segments of the melt, growth rate, and cool-down period (see table 2). The samples

Name	Exess Te (%)	CdTe (g)	Te (g)	Zn (g)	In (ppb)	Zn (x) (%)	Mixing Segments	G. Rate	Cool D (985C)
CG51	0.5	1267.3	74.86	38.37	5000	0.1	bottom (1180) 30C hotter + quick freeze	variablemm/hr, 70C/inch	38.8hrs
CG58	0.5	1267.3	74.86	38.37	5000	0.1	bottom (1180) 30C hotter + quick freeze	variablemm/hr, 70C/inch	38.8hrs
CG59	0.5	1267.3	74.86	38.37	5000	0.1	bottom (1180) 30C hotter + quick freeze	variablemm/hr, 70C/inch	38.8hrs
CG67	0.5	1267.3	74.86	38.37	5000	0.1	bottom (1180) 30C hotter + quick freeze	variablemm/hr, 70C/inch	38.8hrs
CG71	0.5	1267.3	74.86	38.37	5000	0.1	bottom (1180) 30C hotter + quick freeze	variablemm/hr, 70C/inch	38.8hrs

Table 2: Necessary growing condition for selected ingot

Courtesy of CMR

selected from these ingots, especially CG59, are primarily single crystals, but some with other kinds of extended defect along the growth interface. Of course the latter will show how these other defects, i.e. grain boundary, can corrupt this correlation. All selected ingots contain intra-phase defects including Te inclusions which have a unidentified orientation distribution. They

have high specific resistivity (>10^9 Ω.cm) and varying degrees of energy resolution (high P/V ratio for better resolution). (For additional reference to the cause and effect of higher resistivity, see [1&12].) Sample size ranges from 5x5 (mm^2) to 10x10 (mm^2). The samples are well-polished as presence of a crack or debris left on the sample surface (as shown by IR image) can corrupt the test result. This would weaken any correlation established between the MT values and various parameters such as the volume % of Te inclusions present in a given detector.

Selecting samples with high resistivity (CMR prefer >10^{10} Ω.cm), after considering related growth factors, brings a researcher one step closer to confirming a correlation between the MT and Te inclusion's SSD parameters. Primary SSD parameters include diameter and standard shapes of Te inclusions, as estumated in a processed Tagged Image File Format (TIFF) image. Secondary SSD parameters are volume % and population density of inclusions in any given detector. Other parameters can include the thickness and area of interest (AOI) of the detector studied.

Name	**t after G; furnace**	**Time of Growth**	**Amp Dev**	**SuperC**	**Deposits**	**Ingot L**
CG51	52.25hrs	281.48hrs	0.75	3.06	0.14%	91.4mm
CG58	16.17hrs	282.42hrs	0.75	4.47	0.14%	90.0mm
CG59	20.57hrs	281.53hrs	0.75	0.59	0.11%	90.0mm
CG67	24.00hrs	281.48hrs	2.12	2.00	N/A	91.5mm

Table 3: Other necessary growing condition for selected ingot.

Courtesy of CMR

Selected ingots met the given condition in table 2; all four ingots are 0.5% composition Te-rich grown. Other conditions, which were marginally considered, include time of growth (total

time it takes for an ingot to grow), ingot length (L), super-cooling of the crystal ingot, ampoule devitrification, and a deposited percentage of excess Te [table 3]. These factors may change the crystal composition, structure, and critical properties which include growth impurities associated with growth defects, resistivity, MT value, and Te inclusions' SSD results.

The study of these four ingots will expose the challenges of replicating desirable results in CZT growth. It will show how the presence of impurities in any given ingot as seen in the GDMS report can affect a detector's performance. Furthermore, the variation of extended defects including Te inclusions can exacerbate the impact of these impurities in a detector, hence ruining a detector. It will show how widening of Te inclusions' diameter range can severely lower MT values regardless of high resistivity and low impurity levels of a given detector. In general, it will confirm the proposed theory that it is Te inclusions with average diameter >4um that are the largest detriment to electrical properties of a CZT detector and suggest theories and strategies to rectify the inclusion problem. Finally, it will show that $Den_{<4um}/Den_{Total}$ >80% theoretically contributed to an MT value of $2.0*10^{-3}$ cm^2/V with a an error bar of 24% to most of the samples cut from the area within or around the shoulder of the ingot (these areas may have a better uniformity of Zn concentration and hence uniform resistivity).

II Other selected samples and expectations

Other selected samples came from CG78, CG80, CG92, and CG93. Their respective growing parameters are given in the table 4, 5, and 6. Given table 5, a list of parallel growing conditions for CG78 and CG80 includes the raw material, temperature of mixed segments in the

melt and growth rate. These two ingots were both cooled with a gradient, but over different lengths of time. Other factors such as time period of growth, super-cooling, and so on were different (table 4).

Name	t after G; furnace	Time of Growth	Amp Dev	SuperC	Deposits	Ingot L
CG78	10 hrs	652.17hrs	2.0	3.06	0.30%	100.6 mm
CG80	N/A	1270.2hrs	2.0	4.47	0.63%	86.55 mm
CG92	N/A	281.53hrs	1.5	0.59	0.01%	88.3 mm
CG93	N/A	281.48hrs	N/A	2.00	N/A	82.6 mm

Table 4: Other necessary growing condition for selected ingots, CG78, CG80, CG92, & CG93. **Courtesy of CMR**

Name	Exess Te (%)	CdTe (g)	Te (g)	Zn (g)	In (ppb)	Zn (x) (%)	Mixing Segments	G. Rate	Cool D (985C)
CG78	0.5	1267.3	74.86	38.37	5000	0.1	bottom (1180) 30C hotter + quick freeze	0.5mm/hr, 70C/inch	Horizontal gradient 267hrs
CG80	0.0	1267.3	74.86	38.37	7000	0.1	bottom (1180) 30C hotter + quick freeze	0.5mm/hr, 70C/inch	Horizontal gradient 866.02 hrs

Table 5 : Necessary growing condition for selected ingots, CG78 & CG80

Courtesy of CMR

The major variations in growth circumstances between CG78 and 80 are: the concentration of dopants added in CG80 is higher than that of CG78; when CG80 was grown without

additional of excess Te, CG78 was grown with 0.5% excess Te; and the duration of horizontal gradient imposed upon CG80 during cool-down process is as twice as long as that of CG78.

Name,	Exess Cd (g)	CdTe (g)	ZnTe (g)	Te (g)	Zn (g)	In (ppb)	Zn (x) (%)	Mixing Segments	G. Rate	Cool D (985C)
CG92	0.2137	1836	164.0	108.5	55.6	7500	0.1	bottom (1180) 30C hotter + quick freeze	0.5mm/hr, 70C/inch	70.71 hrs
CG93	0.2137	1836	164.0	108.5	55.6	7000	0.1	bottom (1180) 30C hotter + quick freeze	0.5mm/hr, 70C/inch	70.71 hrs

Table : Necessary growing condition for selected ingots, CG92 & CG93

Courtesy of CMR

Note that even though CG80 was grown with no excess Te, CdTe charge used to grow CZT is reported to be Te-rich and the variation of Te is unclear throughout the charge. The study of these two ingots will illustrate the thermo-migration process of Te inclusion in a CZT matrix. It will demonstrate how a more rapid cool-down period allows less time for Te inclusion transformation. These two ingots will show a decrease of Te inclusion diameter range in comparison to CG59, but an increase in volume % and average diameter. Most of all it will show that a significant decrease of $Den_{<4um}/Den_{Total}$ % (>46%) compared to that of CG59 or CG64 is the reason the MT value drops to an average of $1.11*10^{-3}$ cm^2/V or less. This $Den_{<4um}/Den_{Total}$ % however, is close to >68% if one also considers Te inclusions with average diameter <6um. Te inclusions and/or voids in both CG78 and CG80 are relatively as uncluttered as those shown in CG64 edge sample, but their sizes are much bigger. In fact, the average diameter in all studied samples in CG78 and CG80 are greater than 6um.

The results from these ingots will show that even though narrowing the size range and establishing a more spacious and even distribution is necessary, a decrease of Te inclusion average diameter is most important. In addition, this section will explore the evolution of Te inclusion shape, possibly as a result of temperature variation, Te population density and resulting pressure, other extended defects, Te inclusion composition, and/or imposed cooling period. It will show that a uniform concentration of Te inclusions and voids can more effectively be exhibited on a radial cut slice compared to that of axial cut. Finally, it will show that a high concentration of dopants drops the MT value regardless of high bulk resistivity, $>10^9$ Ω.cm (i.e., CG80 detectors gave poorer MT value than those of CG78). However, it is far more common to find Te inclusions in concentrations large enough to ruin a detector than to find dopants in quantities capable of the same effect.

The unusual and unclear effect of increasing population density of Te inclusion in CG80 compared to CG78 further suggests that CG80 was far off-stiochiometry leading to formation of voids and inclusions. Increasing cool-down period further favored Te diffusion controlled growth and low concentration of Te resulting in the formation of more voids comparable to CG78 [26]. Of course this claim takes into consideration that a radial cut from the shoulder where the cool-down gradient was imposed further contributed not only to uniformity, but also an increasing population density of Te inclusions. The litmus test of Te inclusions present in CG80 strongly suggests so and it produced detectors with relatively low MT value comparable to CG78.

CG92 and CG93 were grown almost in the same conditions as shown in table 6, but CG93 took longer to cool down compared to CG92. Other differences in their growth conditions are

given in table 4. Note that both CG92 and CG93, like CG80, are also both grown without addition of excess Te. Yet it is true that this growth is still Te-rich due to excess Te present in CdTe charge. The results from CG92 and CG93 are markedly different, mainly due to a current fluctuation in the furnace during growth of CG93 which resulted in unnecessary noise. This induced noise, associated with oscillation of the temperature-profile, may have further increased crystal inhomogenity which exacerbated the extended defects, especially at the mid of the ingot. These extended defects include line defects which are thought to be dissolved or condensed Te inclusions.

A remarkable contribution of these two ingots, which were Cd-rich grown, is the fact that added Cd reacted with Te solvent during cool-down to form CdTe, reducing Te inclusion and void transformation rates. The formed CdTe would subsequently integrate into the CZT ingot before it is fully transformed. This further helps in limiting the spatial variation of CZT, besides increasing electron mobility; the electron mobility of CdTe is 1050 $cm^2/V*s$ and that of CZT is 1000 $cm^2/V*s$ [16]. The added Cd, however, may have decreased Te_{Cd} necessary in improving the detector's resolution to both holes and electrons [7]. The result from CG92 shows a partial success from a number of samples, but the full potential was inhibited by the presence of other extended defects (which included grain boundaries and larger sized Te inclusions). Compared to CG59, the diameter range of CG92 decreases, but still falls short of the ideal values of CG64.

CG93's diameter range narrowed compared to CG92, but its overall average diameter did increase. This is only in reference to the region within and around the shoulder of the ingot. Smaller sized inclusions and voids seem to have dissolved into the CZT matrix and others transformed into line defects in other parts of the ingot (from mid to the heel of the ingot). This

resulted in an MT drop from $2x10^{-3}$ to $1x10^{-3}$ cm^2/V or less. The impact of line defects is more harmful as they have a higher surface area to volume ratio which could act as a stronger impurity attractant; these line defects can play the same role as micro-channels [20]. Some CG92 samples which were cut from the mid of the ingot faced this situation of small percentage line defects which lowered the MT value. Also note CG93 samples that were highly populated with line defects are reported to have poor quality detectors. Compared to CG92, the overall increase of population density of Te inclusions and voids with large diameters compared to those with small diameters and their sparseness contribute to a poor MT value (this observation only accounts for detectors extracted from regions that are relatively free from line defects). Also, CG93 raises awareness that the effect of Te inclusions and voids is less damaging than the effect of line defects that are suspected to be condensed Te inclusions and/or voids. The random arrangement of these line defects completely blocks electron mobility. It would be beneficial to explore these line defects: how they are formed, of what they are composed, and how they could be avoided.

CHAPTER 4

I Experimental description and procedure

This experiment involves IR Mapping which employs an Optical Microscope coupled with CCD Camera & Image-Pro Software as discussed below.

II Optical Microscope and CCD Camera

CMR uses a optical microscope attached with high performance quantitative digital CCD (charge-coupled device) Camera (i.e., QImaging Camera; designed for life science microscopy and industrial imaging applications) to study Te inclusions present in CZT. A USB port feeds the computer with images taken by the camera via Image-Pro Micro software. Image-Pro Micro software is used to acquire Depth of Field/Extended Depth of Field (DOF/EDF) image taken by a CCD camera, tile them, and store them in TIFF. An identification (or count/size) command with measurements such as mean diameter, roundness, area, and perimeter maps spots of dark (opaque) particles present in TIFF images in red [30].

Note that the dark (opaque) particles mapped in TIFF images are mostly fraction of Te inclusions and voids, but generalized as Te inclusions Classification of Te inclusions' opaque appearance can theoretically relate to the fact that Te inclusions as group VI semi-metalloid absorb photons transmitted by IR LED light of about 881nm wavelength used at CMR. This wavelength range is much larger than that of CZT, which assumes a Zinc-blend structure, but far smaller than that of a Te inclusion [1]. Estimated CZT photon wavelength is approximately 0.82nm and that of Te inclusions is approximately 3.76um. This makes a pure CZT crystal by

itself transparent to IR LED light, but not Te inclusions. Te inclusions as seen by IR microscopy have several shapes: hexagonal, triangular, trapezoid, round, and other nondescript forms which are distinguishable from the star-like form of Cd Inclusions. The nature of these shapes has been explored in separate studies [15].

III Acquisition of DOF image

The process of acquiring DOF images shows image digitization of detector surface. A single image is divided into its component pixels or (elements). 1x1 binning adjusted exposure is applied as referenced by its row (x direction) and column (y direction) number. Digitized images are referenced in grid fashion; "each pixel in the image is individually sampled, and its brightness is measured and quantified [30]." The charge from adjacent pixels is combined in order to detect and interpret the pixel during CCD readout. Charge in adjacent pixels is combined to create one compressed super pixel in a given image, which will be visible on the monitor. The binning of the pixels of any given image will reduce the noise generated by said image, therefore increasing sensitivity of the detector when exposed to an IR light source. Signal to Noise ratio (S/N) translates the depth of image information, i.e. 1x1 binning has a single bit of signal and a noise. 2x2 binning has 4 bits, each of which has an assigned signal and a noise. When these 4 bits are added together, it assumes a S/N of 1/2. This ratio allows for greater sensitivity, but results in a loss of resolution. This is why CMR prefers to use 1x1 binning which maintains image resolution of a given detector.

Acquired DOF image of a detector in testing using 1x1 binning and a corrected background has better sensitivity and resolution. Background correction compensates for any sensitivity lost as a result of using 1x1 binning instead of 2x2 or higher binning. DOF is the amount of distance

between the nearest and the farthest objects in Z-direction appearing in a sharply focused image. All studied DOF selections are subjective, but every acquisition of these DOF images from IR microscopy maintains a slice size close to 17.5 um in any given Z-depth of known plane/frames. This slice size value was studied at CMR and it was concluded that it effectively results to acquisition of most Te inclusions and/or voids. A 10x eye piece is used as well. DOF applies an automated scheme to read and capture a picture in Z-direction from the first plane and then refocus further into the detector to read and capture the next picture in the second plane. This continues until the microscope moves throughout the entire depth of the detector before it compiles all "in focus" planes into one single picture (without repetition) with maximum contrast. Next, the camera shifts to a new xy coordinate and repeats the process until the entire detector has been examined [30]. The acquired image with local contrast is then saved as TIFF image. A collection of acquired DOF TIFF images are then tiled and saved as a master TIFF image.

Note that there is a significant difference between a DOF image and a single image. Figure 9(a) represents a single image tiled in a 2x2 orientation. Figure 9(b) shows a DOF image tiled in a 2x2 orientation. A scratch on the surface as shown on figure 9(b) suggests that the camera has travelled step by step across the planes and captured all inclusions once, including scratches and debris (surface detects [5]), usually without

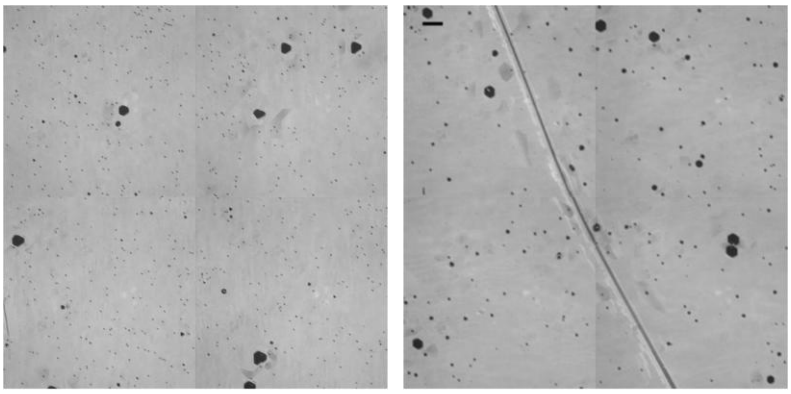

Figure 9: From the left; (a) Detector 1 with single 2x2 tiled image (b) Detector 2 with DOF 2x2 tiled image.

Courtesy of CMR

repetition. In cases where inclusions (and/or voids) are overlapping on the Z-plane, multiple inclusions can be shown as a conglomerate mark in the 2-D TIFF image (see figure 10). This characteristic is a weakness because it can contribute to a less precise SSD test result.

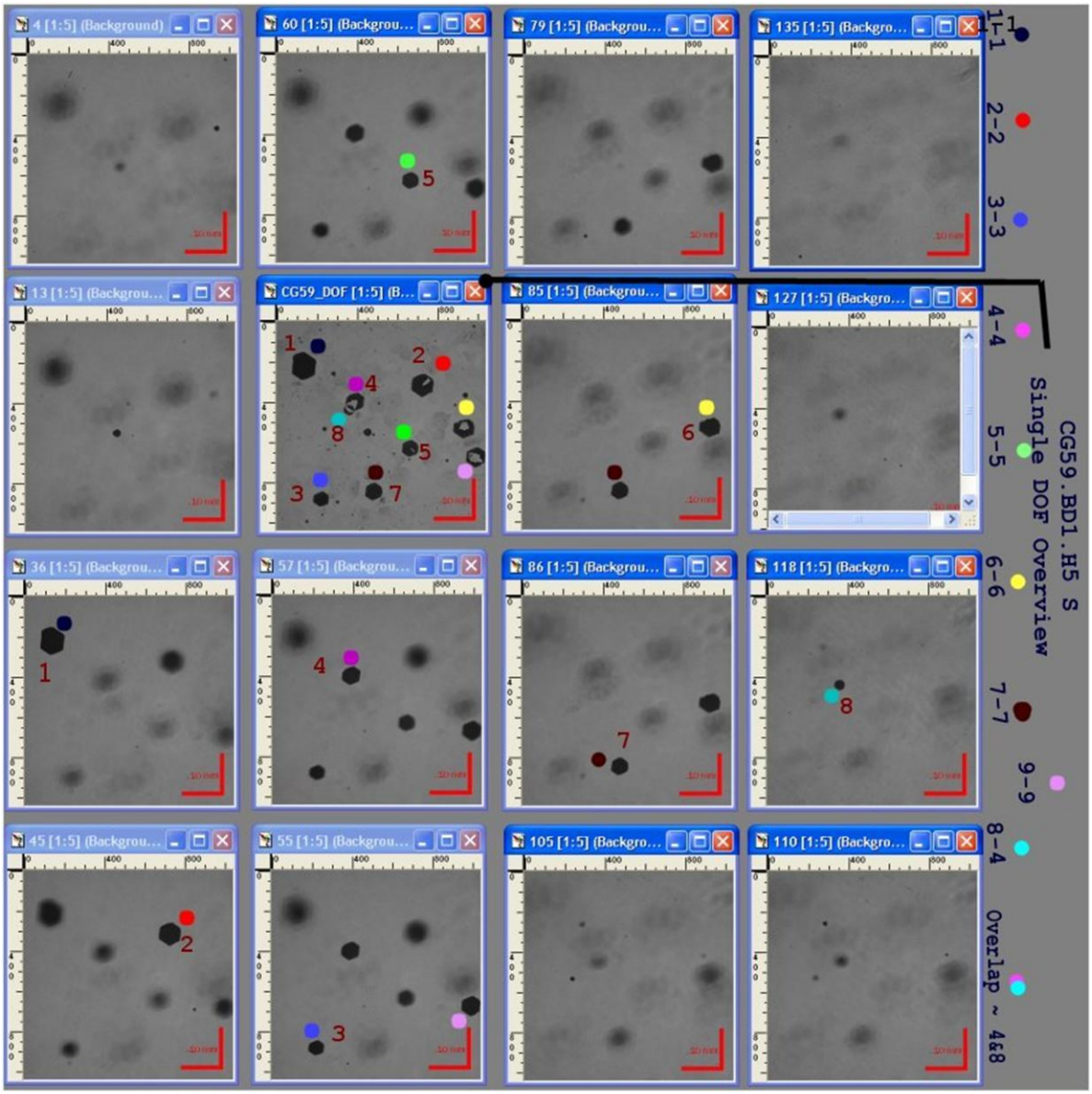

Figure 10: Overlapped inclusions and/or voids ~ Multiple Z plane images (single) and single DOF image. The DOF image is named as CG59.BD1.H5 S. 9 big inclusions were selected. 154 single images, 17.50um apart (z-step of 17.5um) of CG59.BD1.H5 S DOF image shows that no smaller inclusions were spotted in close proximity to the 9 selected inclusions. However, inclusion 4 and 8 overlapped and this is seen in the final DOF image.

Furthermore, DOF image, figure 9(b), is much more detailed and has better resolution than the single image given in figure 9(a).

In addition, proceedings from SNRL conferences reveal that a high percentage of CZT samples contain both Te secondary phases and voids [5]. This characteristic is revealed in figure 10. The higher number of voids leads to inaccurate Te inclusion counts. Smaller inclusions between the voids which are invisible to the camera are not captured and this artificially deflates the volume %. Other larger inclusions which are not fully covered by the voids but show up as fractions of Te inclusions may or may not be counted as whole by the system (count/size command discussed below). Those that show a complete outline (inclusion 6 in figure 10) are counted as whole inclusions and this does not affect the volume %. On the other hand, those whole inclusions which do not show a complete outline are counted only as fractions and this artificially deflates the volume %. On the contrary, it is necessary to consider the possibility that those Te inclusions which are captured as fractions were actually dissolved into the CZT matrix leaving behind complete formation of voids. This then would neutralize a claim that the volume % is artificially deflated when inclusions are counted as fractions and imply that the volume % was artificially inflated in cases where inclusions were counted as whole. Furthermore, a given orientation of an inclusion with respect to the camera's one-dimensional line of vision may inhibit full image capture. This may further add to inaccurate estimation of volume % of Te inclusions, hence corrupting the intended correlation between SSD and MT value.

In order to avoid this mix-up, it is then effective to account both inclusion and/or voids as just one as the system effectively fails to appropriate them, but instead count them as one. This proposal support the assumption made earlier which consider Te inclusions and/or voids as

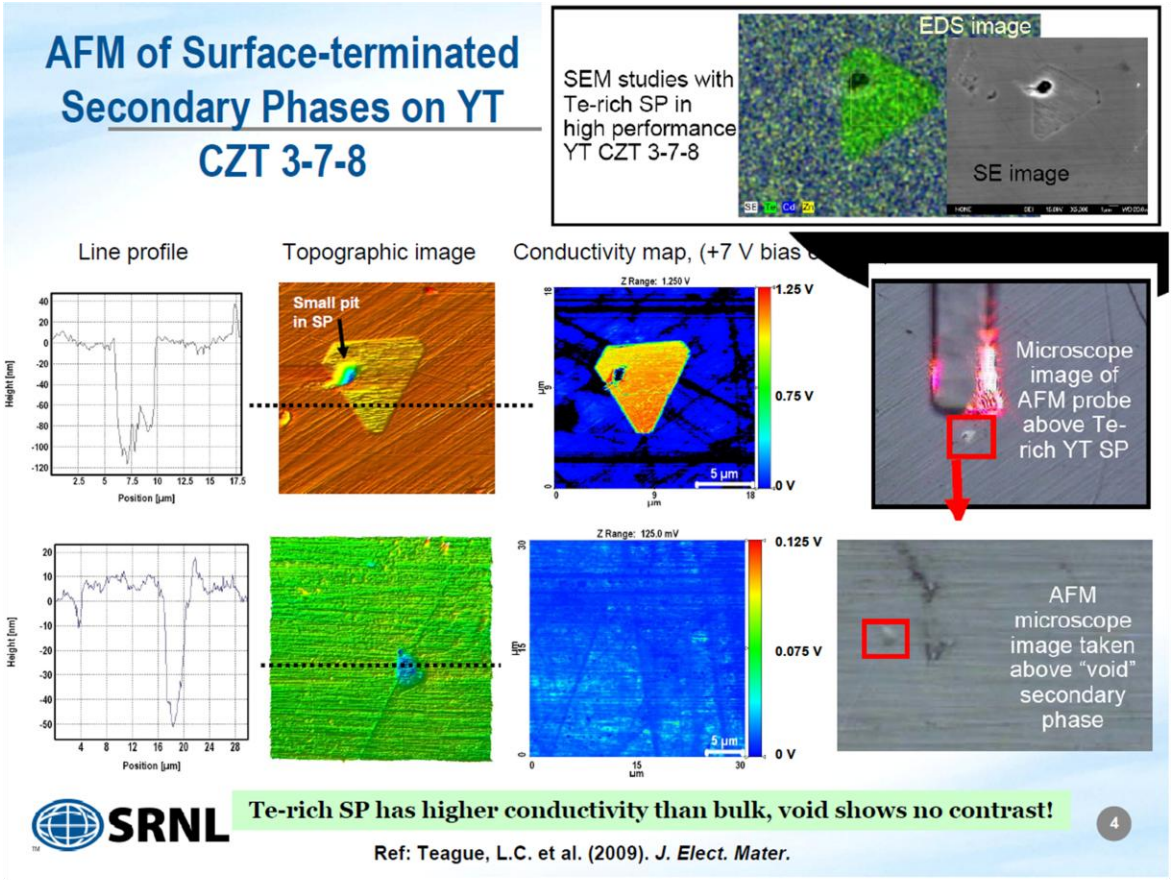

Figure 11: The effect of Te secondary phase and void in a CZT detector. Their conductivity is far much higher than that of CZT bulk. Courtesy of CMR

simply "Te inclusions." The impact of both void and inclusion compared to CZT bulk, remember, is undistinguishable [5] see figure 11.

IV Image tiling and count/size function (Image Pro Software)

The range of distribution given by count/size function is assumed to be symmetrically distributed within a range of segments 0-225, but it is only a far left segment (mostly 0 – 120) which is selected and counted. This range accommodates better counting of Te inclusions with a small average diameter range. Figure 12 is the 26th image from (16x16) CG87.BD2.C5 tiled DOF image. Figure 12(1,2,3,4,5,&6) are contrasting images. Figure 12(2) is the same image with 30

selected segments for count. Figure 12(3,4,5,&6) is also the same image with (40, 85, 115, & 125) selected segments for count respectively. Figure 12(2&3) with far left selected segments for count, covers the majority of inclusions of a bigger average diameter.

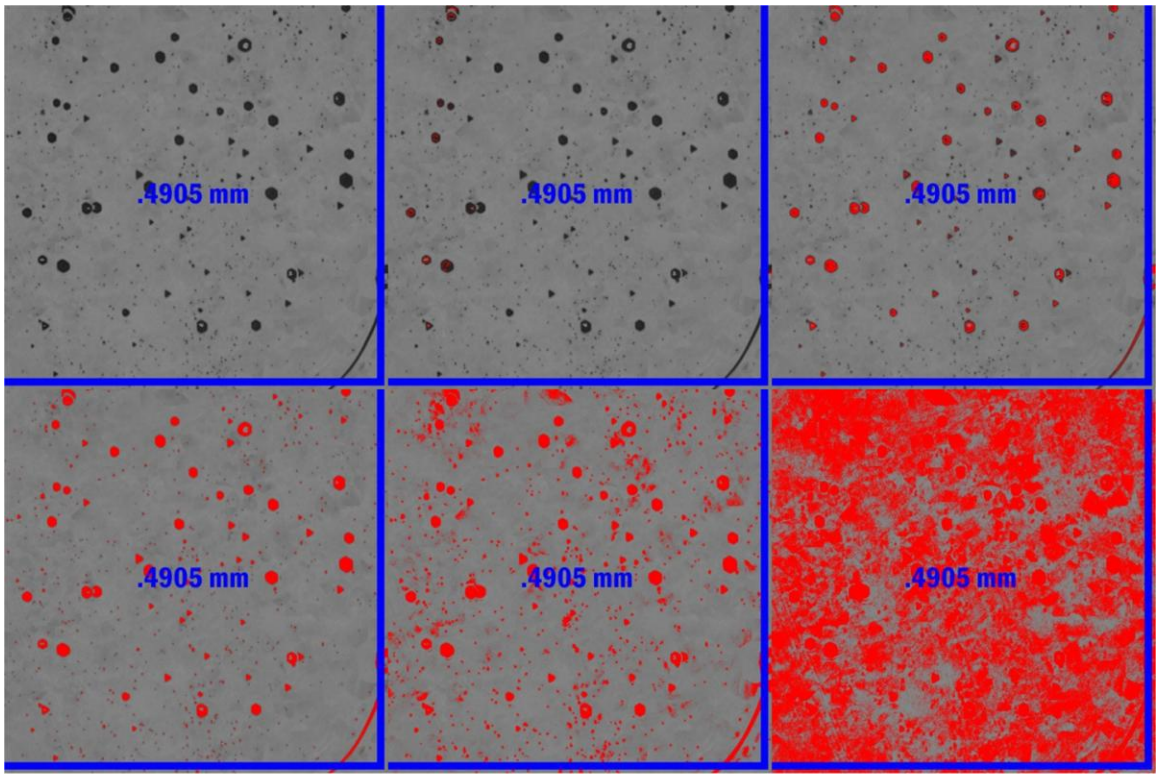

Figure 12: Count segmentations overview ~ 26th image of (16x16) DOF Image of CG87.BD2.C5. (1) Unselected range; (2): 30 selected segments; (3): 40 selected segments; (4): 85 selected segments;(5): 115 selected segments; (6): 125 selected segments.

Figure 12(5&6) with far right selected segments for count, covers most inclusions of a smaller average diameter. Figure 12(4) represents the standard selected segment, which provides a fair opportunity for a precise inclusion count. However, a major flaw in this count/size command is that it counted a lower percent of small-sized Te inclusion in relation to large-sized inclusions. This is because the distinctive intensity between small size and big size inclusion results in the accumulation of unwanted background noise around the inclusion in question (as

shown in [figure 12(6)]) during mapping. The impact of this effect completely alters the expected results. It then forces the user to ignore smaller inclusions and put the majority of the focus on the bigger inclusions. Therefore, variation of Te size distribution is a major player in the effectiveness of this system. Using a random sample from CG78 and CG59, a user error of approximately 23% was calculated. This error accommodates chances of over-counting or under-counting Te inclusions given subjective segments. It also accommodates selective cases where the user misreads the z-depth. The latter is a factor because most of these procedures are performed with the naked eye.

A simple demonstration of this experimental procedure selects the above Single DOF image, option 12(4) with 85 segments for Te count and analysis. These selected segments (85) were first auto-selected by the system and later confirmed as standard. Suspicious marks such as scratches and debris from after-polish dirt selected by the count/size command that fail to match a standard opaque physical presence of Te inclusions are removed from the count (these features are mostly irregular and dull). The net count, which includes measurements such as diameter (mean), is exported to Origin 7.5 software for further analysis.

Count/Size command measurements	
Area	2e-006 ----- 999999
Count (Adjusted)	1 ----- 1000000
Diameter (mean)	0 ----- 1000000
Per Area (Obj/Total)	0 ----- 1
Perimeter	0 ------ 999999.9
Radius Ratio	1 --- 1000000
Roundness	0 --- 1000000

Table 7

Courtesy of MediaCyberanatics

Measurement included in the Count/Size function includes: Area, Count (adjusted), Diameter (mean), Per Area (Obj.//Total), Perimeter, Radius Ratio, Roundness. The "Area" measurement accounts for the area of an object excluding the holes' area if <fill holes> option is

turned off. "Count (adjusted)" measures the size of weighted objects with the clean border option. "Diameter (mean)" measures the average length of diameters which pass through the object's centroid at 2-degree intervals. "Per Area (Obj./Total)" measures the percentage of the object's area in relation to the total area of the AOI. "Perimeter" measures the object's outline. "Radius Ratio" measures the ratio between maximum radius and minimum radius. Last but not least, "Roundness" measures the ratio of the squared perimeter to (4*π*area) [table 7] [30]. Among these parameters, "Count (Adjusted)" and "Diameter (mean)" are further used to process other valuables such as volume % and population density. The "Diameter (mean)" is considered the average diameter. Due to stage calibration error, an estimated average diameter is acquired by subtracting 0.24 um from the average diameter. This value was calculated using Edmund calibration slice that has 2-100um opaque dots [31]. Using 5 different segments 80, 85, 90, 95, and 100 with a 10x objective, a standard DOF image was acquired and a measured value for diameter of opaque dots of each segment range was documented. An average difference per opaque given by 5 varied segments is calculated to be 0.24um.

V Te inclusions Volume % and Density estimation

The analysis of these acquired DOF images is in reference to the two theories that have been proposed concerning the relationship of the size of Te inclusion and electron MT: the first proposes that Te inclusions in general are one of the causes of reduced MT value, while the second notion suggests that it is only those inclusions over the size of 4um which significantly affect the MT value. In order to test these two theories, an excel template [table 8] is created that uses the average diameter of Te inclusions as criteria for classification into one of these two categories: Te inclusions with an average diameter >1um and Te inclusions with an average

diameter >4um. Density and Average diameter of Te inclusions are calculated in this template. Other necessary details with regard to image acquisition are given in this table as well.

Total Count	**4963**
In Range	**2648**

CG64.Edge.4

Volume:	0.004936456 cm^3				
X frames:	4	MT	8.00E-03 cm^2/V		
X frame width:	0.0490 cm	total density	536,417 cm^{-3}	Exposure	00.650.000
Y Frames:	4	$V_{inclusion}$	0.0006 %	Segments	80
Y Frame hieght:	0.0490 cm	$V_{inclusion >4um}$	0.0001 %	Z spacing	17.46 um
Thickness:	0.1285 cm	$V_{inclusion, error}$	0.0002 %	Z distance	2.3578 mm
		ave Diam	2.48	Light source:	881 nm
		ave Diam >4um	+/- 5.36 0.24um	Voltage:	55 v
				Objective:	10X

Raw Data			**Density**		**Percent Volume**			
Diameter (um)	**High (Original)**	**Actual (diam - 0.24um)**	**Density (cm^-3)**	**+/- Density error**	**%V highest**	**%V actual**	**+/- % error**	**Distance**
1	173	721	146,056	35,053	1.8E-06	7.6E-06	1.8E-06	721
3	2437	1899	384,689	92,325	7.0E-04	5.4E-04	1.3E-04	5697
5	33	24	4,862	1,167	4.4E-05	3.2E-05	7.6E-06	120
7	4	3	608	146	1.5E-05	1.1E-05	2.6E-06	21
9	1	1	203	49	7.7E-06	7.7E-06	1.9E-06	9
Sum	2,648.00	2,648.00	536,417		0.0008	0.0006		
Sum >4um	38.00	28.00	5,672		0.0001	0.0001		

The excel template gives a frequency tally of exported diameter (mean) now known as High (Original) from count/size function starting from 1-49um diameter range in 2um step size. The number of steps is estimated to be 25 in cases where the average diameter of inclusions ranges from 1-50um. If there exist inclusions with average diameter >50um, the template steps

are increased, but their sizes remains the same, in order to accommodate additional tallied frequencies. The "actual (diam – 0.24um)" is the frequency tally from Origin 7.5 that includes inclusions of size-less 0.24um diameter (mean), which was initially exported from count/size command.

Upon receiving the result from table 8, a standard allowance for error is applied which correspond to varied count of Te inclusions using different stage setup and segmentations. A calculated Te inclusion volume % error bar using a random sample from CG80 and CG59 was 5-8%. The calculated average diameter error bar was 5-6%. The calculated density error bar was 18-25%. These errors are applied in all reported results in this thesis.

CHAPTER 5

I Results & Analysis: CG(51,58,59&67)

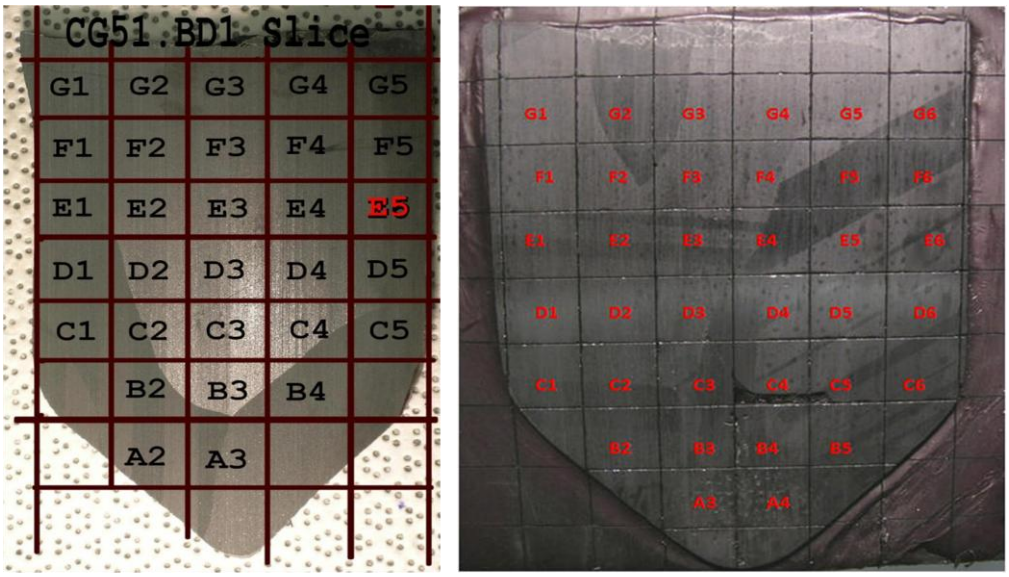

Figure 13(a): From left to right; CG51. BD1 Slice and CG58.BD1 Slice. The slice include various sample cut Courtesy of CMR

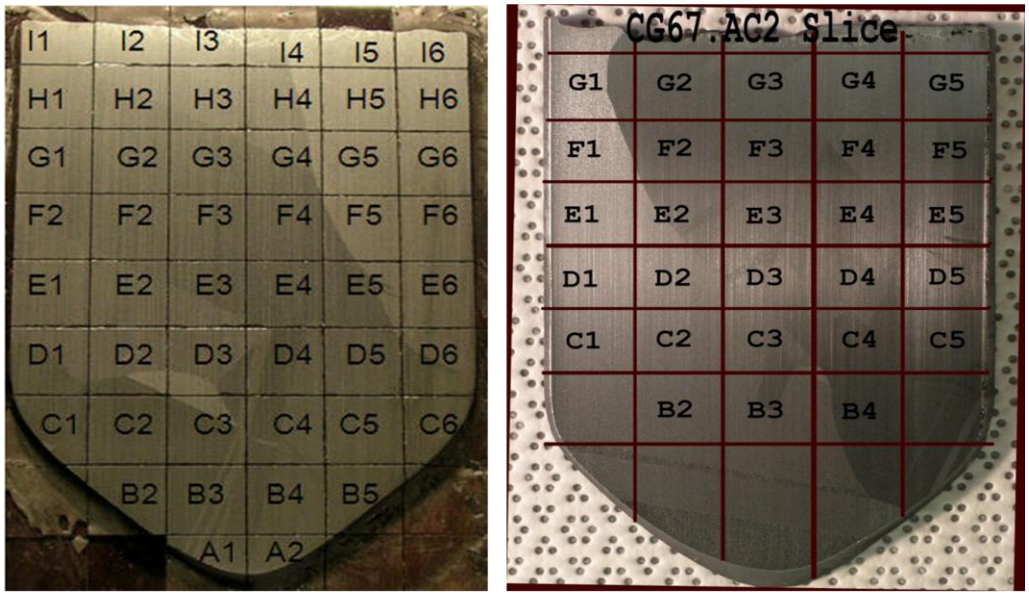

Figure 13(b): From left to right; CG59.BD1 & CG67.AC2 Slice. The slices include various sample cuts. Courtesy of CMR

The four given images in figure 13(a&b) show slices and sample cuts from CG(51,58,59,&67). Each slice reflects an overall approximate percent yield of grains and twins that can be expected of other slices from the same ingot. Of the four, CG59 showed the highest yield of single-crystal detectors, followed by 67, 51, and lastly 58. Given the fact that the four ingots were grown almost in the same conditions, the variation in the percent yield can be traced back to possible zone temperature-profile disturbances. This disturbance, or noise, can be associated to a fluctuation in current flow or power break in the furnace during growth. Other causes include relative variation in ampoule devitrification, super-cooling, total time of growth, and percent deposition of material during growth. Deposition of material can vary markedly along the length of the ampoule and narrowly along the radial perimeter [32]. Ampoule devitrification and the subsequent super-cooling process may or may not affect the final crystal's properties. A more intensive super-cooling was imposed during CG58 ingot's growth. This could have exceeded a critical value at the solid-liquid interface and been exacerbated by the unconventionally low thermal gradient combined with a high growth rate [32].

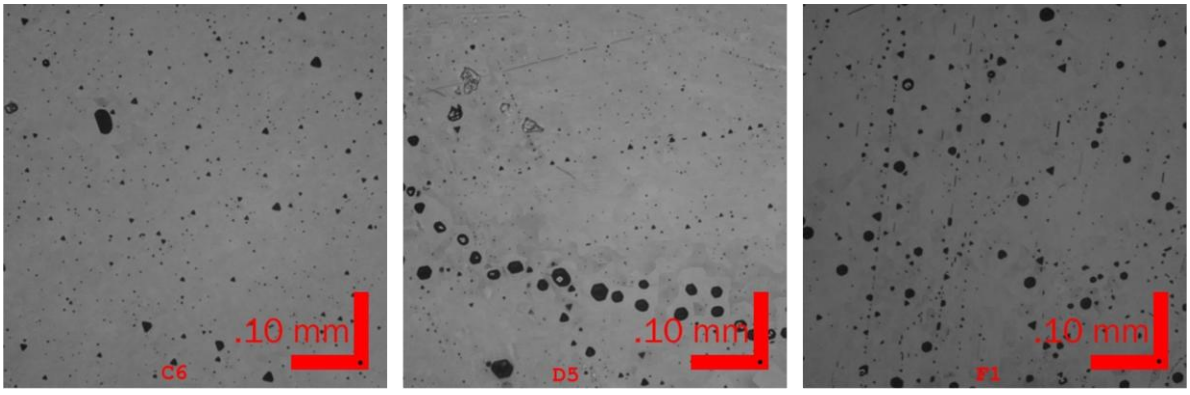

Figure14: Selected DOF images from CG58.BD1.(C6,D5,&F1).

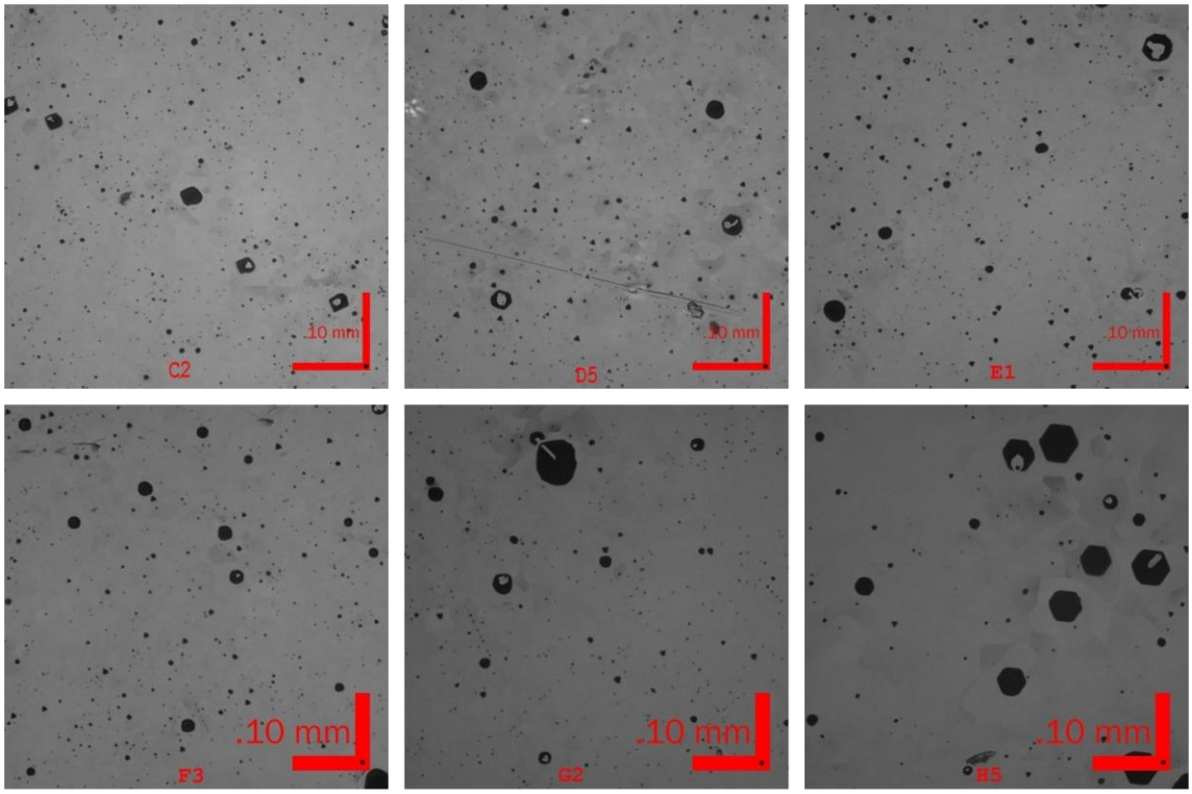

Figure15: Selected DOF images from CG59.BD1.(C1,D5,E1,F3,G2,&H5). The images show the variation in Te inclusion distribution; the range from smaller to bigger inclusions increases towards the heel. Sample C2 has a narrow distribution with a range of 0-35um, while H5 has a wide distribution with a range of 0-75um.

This led to instability of growth interface which resulted in a high yield of extended defects such as twins, sub-grain boundaries, Te inclusions, and dislocations. Variation between detectors' properties from CG58 and CG59 is explored in the light of figures 14 and 15. The MT values given in table 10(a,b,&c) were all acquired using Caesium (Cs)-137 source and 1.5 micro-second shaping time. The error % of MT values at CMR as calculated from 0.5-3.0 micro-shaping time ranges from 3-24% [table 9]. Hence, the MT values of samples from all four given ingots in table 10(a) that are extracted from the mid, C-E, are relatively the same.

Results for CG58.BD1(C6,D5,&F1) with decreasing resistivity and MT value from the shoulder to heel of the ingot are given [table 10(b&c)]. Twins present in this particular slice

MT's in Detector A1; using different micro-shaping time							
	0.5 µs	1.0 µs	3.0 µs		(0.5µs-Mean)^2	(1.0µs-Mean)^2	(3.0µs-Mean)^2
Fit 1	8.80E-04	1.65E-03	1.90E-03		2.78E-10	9.34444E-09	9.00E-10
Fit 2	8.20E-04	1.29E-03	1.89E-03		5.88E-09	2.08544E-07	1.60E-09
Fit 3	9.90E-04	2.30E-03	2.00E-03		8.71E-09	3.06178E-07	4.90E-09
Sum	2.69E-03	5.24E-03	5.79E-03	Sum	1.49E-08	5.24E-07	7.40E-09
Mean	8.97E-04	1.75E-03	1.93E-03	Variance	4.96E-09	1.75E-07	2.47E-09
				S. Deviation	7.04E-05	4.18E-04	4.97E-05
				S. Error	4.06E-05	2.41E-04	2.87E-05
				Error %	7.85	23.93	2.57

Table 9. Error % estimation for MT values using 3 independent fittings. Detector A1 excited by 59.5 keV gamma rays. **Courtesy of CMR**

S	CG51				CG58				CG59				CG67			
	#	MT	#	*P/V*	#	MT	#	*P/V*	#	MT	#	*P/V*	#	MT	#	*P/V*
H									1	7.70E-4	*1*	*1.36*				
G			*1*	*1.68*					1	1.46E-3	*1*	*1.46*	2	1.18E-3	*1*	*1.36*
F	1	1.48E-3	*3*	*2.01*	1	1.24E-3	*1*	*1.40*	1	1.62E-3	*1*	*1.60*	1	1.20E-3	*0*	*NA*
E	1	1.65E-3	*5*	*2.23*	3	1.56E-3	*3*	*2.00*	2	1.70E-3	*2*	*1.82*	2	1.47E-3	*3*	*1.57*
D	2	1.91E-3	*4*	*2.03*	4	1.76E-3	*4*	*1.88*	3	1.83E-3	*2*	*1.54*	3	1.83E-3	*3*	*1.97*
C	1	1.92E-3	*2*	*1.85*	2	1.50E-3	*1*	*1.50*	2	2.07E-3	*2*	*1.63*	4	1.69E-3	*4*	*1.97*
B			*1*	*2.10*	2	7.20E-4	*2*	*1.21*	2	1.80E-3	*1*	*1.37*	2	1.68E-3	*2*	*1.46*
A			*1*	*1.56*												

Table 10(a): MCA averages for CG(51,58,59,&67) along the growth direction A-H. S stands for different as shown in figure 11(a&b) ~ A-H; # stands for number of samples tested for either MT or P/V ratio. All values in the mid (CBEF) are within the same error bar. A, H, & G values vary mildly. **Courtesy of CMR**

gave contrasting images which show unique distribution of Te inclusions (see [figure 14]). Occasionally, a decrease of MT value from the shoulder to the heel of the ingot seems to correlate to increasing volume %, increasing average diameter and density ratio ($Den_{>4um}/Den_{Total}$ %) of Te inclusions.

Table 10(b): Selected CG(58&CG67) Properties				Courtesy of CMR
CG	58_C6	58_D5	58_F1	67_C4
MT (1.5 shaping) ~ $x10^{-3}$	1.57	1.72	1.24	1.69
ρ (Ω.cm) ~ $x10^{10}$	3.98	3.73	2.00	3.80
Peak to Valley Co57	1.50	1.63	1.40	2.01
Count	78649	58721	95522	63165
Volume % (%)	0.0080	0.0075	0.0116	0.0088
Volume % >4um	0.0075	0.0071	0.0112	0.0082
Density (Counts/cm^3)	528959	549898	508676	599349
Density >4um	133704	146490	208126	112355
$Den_{<4um}/Den_{Total}$ %	74.7 %	73.4 %	59.1 %	81.3 %
$Den_{>4um}/Den_{Total}$ %	25.3 %	26.6 %	40.9 %	18.7 %
Ave D (um)	3.72	3.90	4.91	3.38
Ave D >4um	7.37	7.87	8.25	7.23

Further results from CG67.AC2.C4 are given [table 10(b)], and seem relatively smaller than expected. An increase of density ratio, >80%, should have given a relatively better result than those given by CG58 samples. The fact that the MT value of the detector in close proximity, CG67.AC2.C5, was $>2*10^{-3}$ cm^2/V, suggests that the increased percent of grain boundaries did alter the detector's properties. Therefore, the effect of grain boundaries seems relatively damaging to detectors properties compared to twins as it results in alteration of MT values and resistivity. Another factor associated with this relatively lower MT value of CG67.AC2.C5 detector is impurity level. According to GMDS report given

Table 10(c): Averages for CG58 detectors	Courtesy of CMR
	CG58.BD1
MT (cm^2/V)	1.51 E-03
Resistivity $x10^{10}$	3.24
P/V Co-57	1.51
Vol % (%)	0.0093
Vol % >4um	0.0093
Den (Counts/cm^3)	185130
Den >4um	99535
$Den_{<4um}/Den_{Total}$ %	46.3 %
$Den_{>4um}/Den_{Total}$ %	53.7 %
Ave D (um)	6.85
Ave D >4um	8.71

in APPENDIX B, the increasing concentration of Fe from the tip to the heel of the ingot did affect crystal properties. The effect of Fe in detector's properties is also somehow related to dropping MT values in table 10(a), column C of CG58. This column is within the middle, which gave a higher concentration of Fe. CG58 ingot also had multiple twins distributed all over the ingot, but the variation of Te inclusion distribution seems relatively even and non-effective to crystal properties.

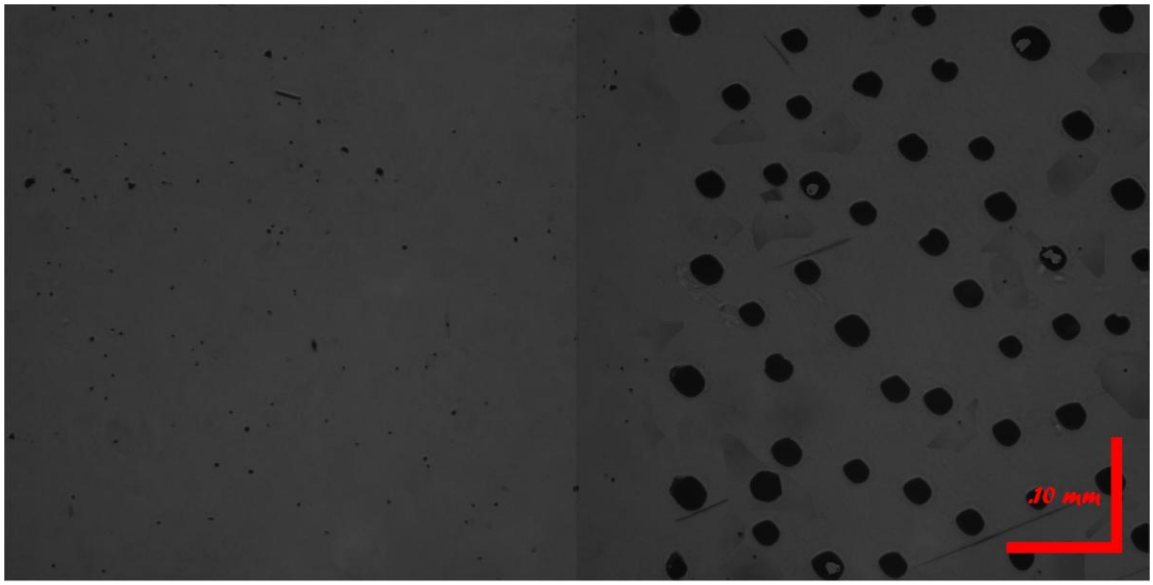

Figure 16: Detector from CG92 Cd-rich grown ingot. Defects distribution within and around the grain boundary

Te inclusions present in CG(51,58,59,&67) generally have a wide distribution. In one case, the size range of Te inclusions present in CG59 samples increases towards the heel. On the other hand, inclusion distribution of CG58 is unique and somehow different due to a higher percentage of twins and grain/multi boundaries which change significantly the inclusion's morphology. Grain boundaries are strong attractants for inclusions and this can be observed in figure 14 (D5, and F1) and figure 14. Te inclusion distribution patterns within and around a grain boundary can be regular or irregular. In figure 16, there appears to be a high concentration

Units	#	#/cm^-3	#/cm^-3	%	%	um	um	Cm^2/V	Ω.cm
Error (+/-)	1801	195116	25049	0.0013	0.0012	0.41	0.11	24%	
Name	Counts	Den	Den >4um	Vol%	Vol% >4um	Ave D	Ave D>4um	MT ~ $*10^{-3}$	ρ ~ $*10^{10}$
C2	103959	665394	123230	0.0081	0.0075	3.46	7.61	2.02	2.64
D5	96865	589292	131407	0.0076	0.0072	3.62	7.53	2.01	3.31
E1	117443	616754	112692	0.0082	0.0077	3.34	7.41	1.52	2.66
E4	100391	551726	122056	0.0082	0.0078	3.56	7.57	1.90	2.90
F3	94475	472070	110469	0.0095	0.0092	3.62	7.50	1.62	2.20
G2	113613	557506	78670	0.0086	0.0081	3.22	7.81	1.46	1.66
H5	68387	364536	67697	0.0086	0.0083	3.68	7.83	0.77	1.15

Table 11: CG59.BD1 SSD results; ρ stands for resistivity.

Table 12(a): CG59.BD1 Samples Properties. **Courtesy of CMR**

CG59.BD1.	B4	C5	D4	E1	B3	C2	D3	D5	E4	F3	G2	H5
Thickness (mm)	2.6	2.64	2.63	2.66	2.707	2.701	2.752	2.736	2.606	2.68	2.74	2.669
Contact Area (sq.mm)	96.03	98.99	95.84	95.35	95.99	94.47	98.33	97.34	97.19	98.82	97.73	97.74
ρ ($x10^{10}$ Ω.cm)	0.74	3.46	3.96	2.66	3.29	2.64	3.65	3.31	2.90	2.20	1.66	1.15
MT ($*10^3$ cm^2/V)	1.51	2.12	1.94	1.52	2.00	2.02	1.54	2.01	1.90	1.62	1.46	0.77
14KeV peak visibility; ^{57}Co	Good	Good	Good	Good	Good	Good	Poor	Good	Good	Good	Good	Good
P/ V; ^{57}Co	1.37	1.95	1.38	1.84	NA	1.30	NA	1.70	1.80	1.60	1.46	1.36

of Te inclusions on the far right where a number of grain boundaries run through diagonally along the detector's plane. High generated pressured in CZT structure within and around the grain boundaries creates micro-channels and/or micro-cracks to which Te inclusions are drawn

[20]. The outside pressure forces Te inclusions to streamline into a short-range or long-range order. Neighboring regions free from grain boundaries (small single-crystal areas) are then filled with lower percentages of Te inclusions as shown by figure 14 (D5, and F1) and figure 16. The

properties of a detector which exhibits these kinds of defect traits include low or immeasurable MT values. The impact of these inclusions in all SSD aspects, especially density and volume % is enormous.

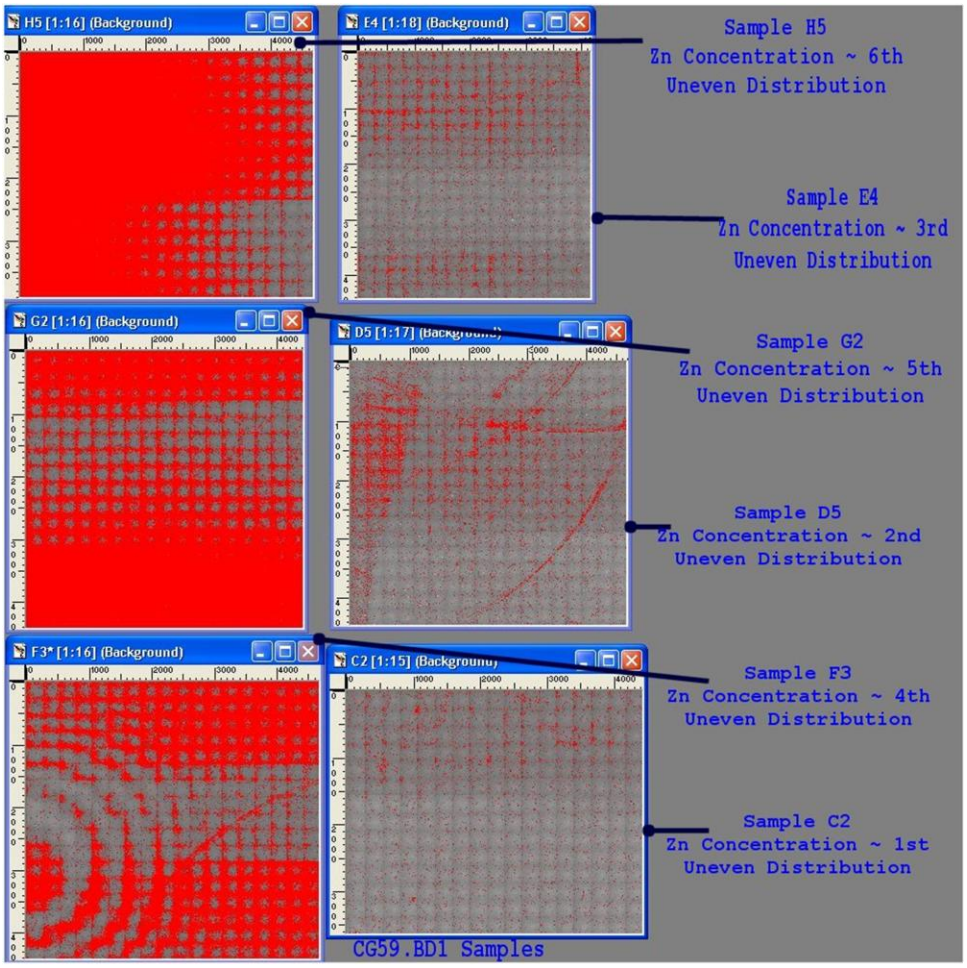

Figure 17(a): Mapping zinc concentration along the growing direction using 110 segments from Count/Size Command/Function. Uneven distribution of red marks around the image explain that Zn or Te Inclusion are unevenly distributed. Zn concentration is rank from the highest, 1st, to the lowest, 6th.

A stronger correlation is further explored in depth in CG59 Te inclusions' SSD results (see table 11). MT values given by detectors C-H from CG59 vary slightly [table 12(a)]. The same

applies to P/V ratio, which analyze how effective a detector can resolve both holes and electrons, and clear visibility of 14KeV peak analyze detectors' electron resolution. It is preferable, however, to first consider detectors within C-E (within and around the shoulder) for a better correlation across ingots as their resistivity is approximately the same.

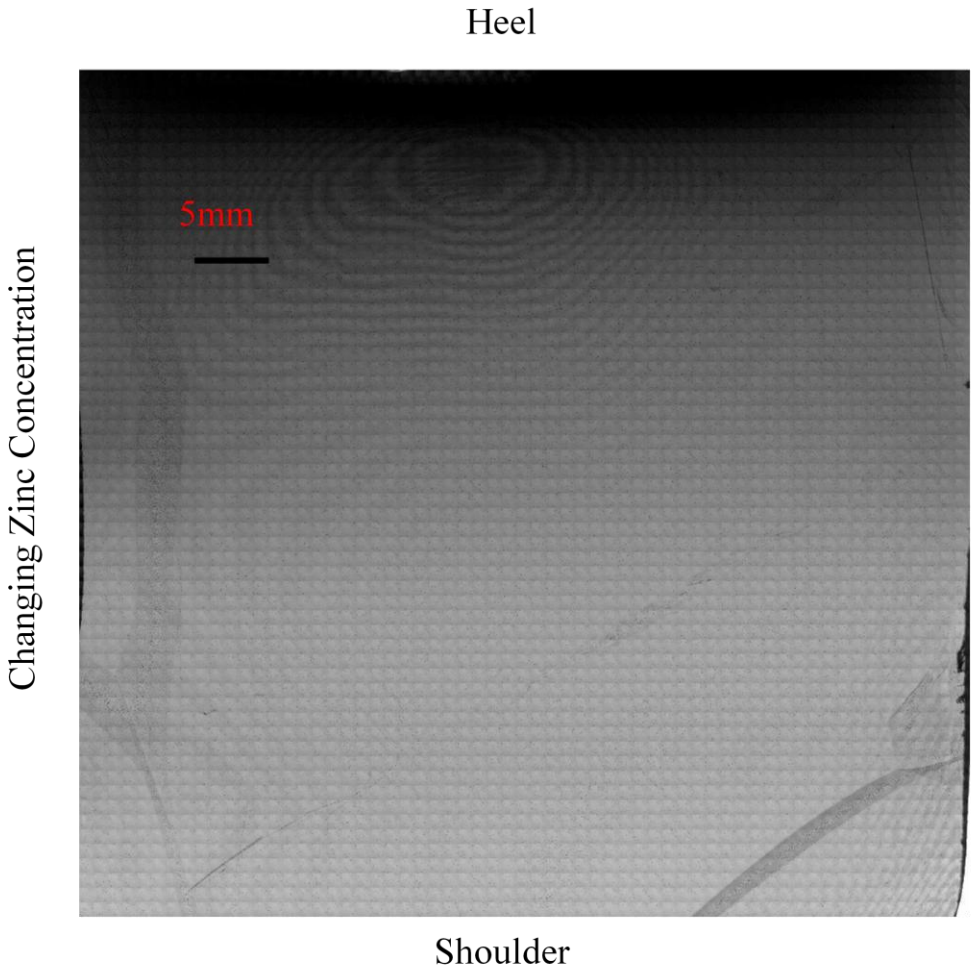

Figure 17(b): Changing Zn Concentration: affect detector's property especially resistivity distribution

IR mapping of a slice shown in figure 17(a&b) further supports a decrease in resistivity towards the heel. This variation in light absorption given in figure 17(a) can also be a result of uneven distribution of Te inclusions, non-uniform slice thickness, and stage movement during

image acquisition. The poor illumination made it difficult to get an accurate inclusion count and may have weakened the projected correlation between Te inclusions' SSD and electrical/optical properties of respective detectors. Detector F3 and H5 are prime examples of this issue [table 11]. The results of these two detectors are not consistent with the projected pattern that proposes a possible increasing concentration of Te inclusions towards the growth direction and a decrease in MT values. Yet, as will be discussed, there are other factors that may have played a major role in the advent of these discrepancies.

In reference to observed discrepancies, it is true that bigger inclusions are more likely to be counted adequately by the system compared to smaller inclusions. Bigger inclusions contribute significantly towards an increase in volume %. This underscores a viable claim that may suggest that inappropriation of smaller Te inclusions compared to the bigger ones may have flawed the desired SSD result. The effect of smaller inclusion as will be shown in table 22 is far less than bigger inclusions. The volume % of both G2 and H5, however, may be slightly underestimated due to the unconfirmed count of small inclusions and close size (diameter) range. Low Zn concentrations in these two samples could also corrupt the image background, resulting in undercounting of not only smaller inclusions, but also bigger inclusions; fewer segments in comparison to the rest were counted in these two samples. This is especially evident given detectors that are extracted in a region close to the heel. The imbalance effect of Zn concentration as shown in figure 17(a&b) may result in deep contrasting of illuminated light hence covering features in low Zn concentrated fraction. The light-absorbing tendencies of low Zn concentration in samples closer to this heel could result in a “blending” of large inclusions and darkened patches of zinc, so that the Te inclusion appears as a barely-visible shadow, difficult to identify.

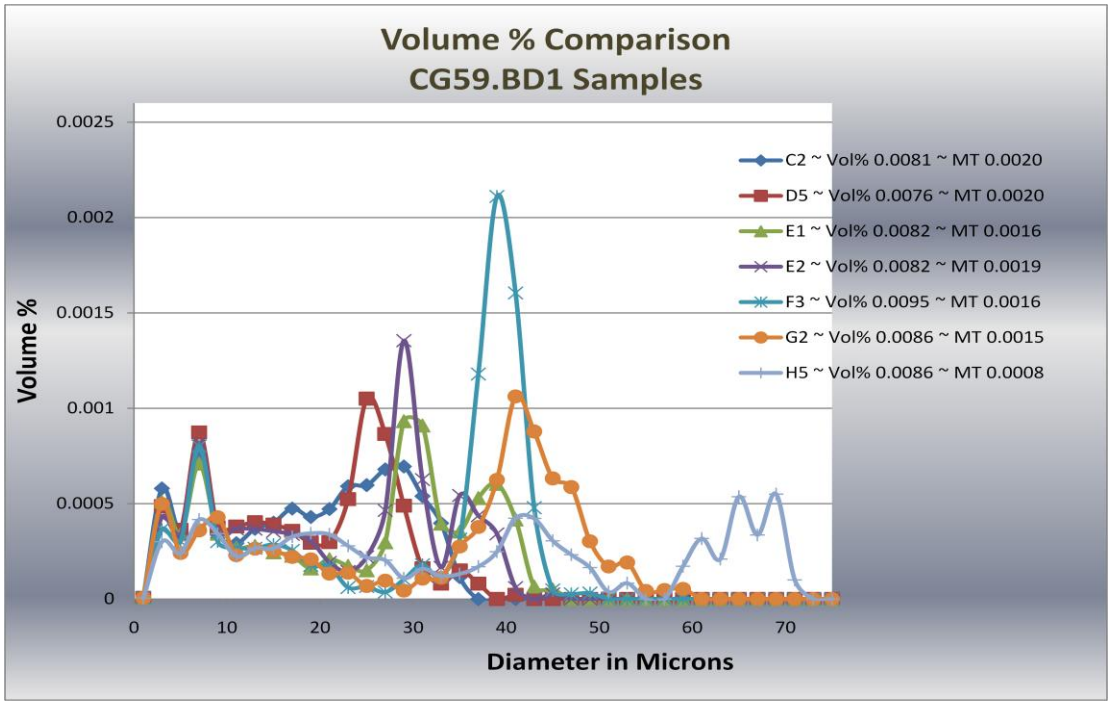

Graph 3: Te inclusion volume % distribution is inconsistent to decreasing MT values from detector C2 to H5. However, the size-range distribution, which increases from detector C2 to H5 is consistent to decreasing MT values.

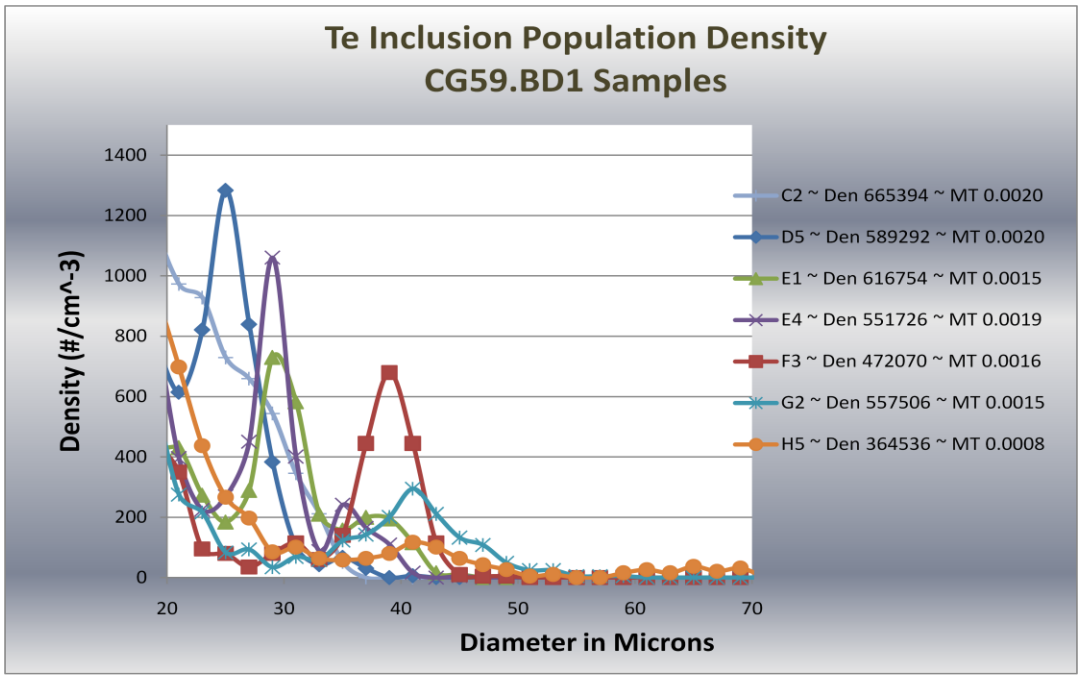

Graph 4: Te inclusion population density distribution is inconsistent to decreasing MT values from detector C2 to H5. However, the size-range distribution, which increases from detector C2 to H5 is consistent to decreasing MT values.

The size of Te inclusions in CG59 samples ranges from 1-75um [graph 3&4]. This distribution widens towards the heel, but its transition is not continuous. Given graph 3, Te inclusion volume % distribution of the studied detectors failed to give a consistent correlation to detectors' MT values. The same applies to population density of Te inclusion given in graph 4. Keep in mind that the measured Te inclusions (inclusions and/or voids) are assumed to be spherical. The size rage of these detectors from C2 to H5 (E1 and E4 having the same size range) is as follows: 0-35um; 0-41um; 0-49um; 0-60um; 0-72um. Furthermore, both population density and volume % comparison plot for Te inclusion shows a consistent decrease of MT values as size range (x-component) increases.

Initially, one may suspect that secondary SSD parameters such as Te inclusions' volume % and total density are supposed to increase towards the heel ([12] claims that it is the heel that has the highest concentration of Te precipitates). This is not always the case in most given detectors cut along a slice from known ingots at CMR. This, however, may apply to Te precipitates if they were visible. Detectors from CG59 strongly suggest that the transition is not continuous. The sharp increase in volume % reported by sample F3 in table 11(a) and shown in graph 3 is an example that discontinues this transition. Given an error bar of 8%, it is clear that the volume % of sample F3 is the highest. This increase of volume % in Sample F3 should trigger a drop in MT value, but the value remains in relatively close proximity to MT values of other samples with a smaller volume %. This effect can be associated with a number of facts: A large error bar of nearly 24% is imposed in all MT value estimations; the amount of Te inclusions in this sample is relatively smaller than the rest (table 11); given the volume % comparison plots in graph 3, this increment is only within a small size range, 35-45um, and its associated density is lower than

800 (counts/cm^-3) (see graph 4). Yet, this density, between the size range 35-45, is the highest of all.

This inconsistency in both volume % and population density then singles out the size range distribution of Te inclusions as a key parameter that is pertinent to MT values.

In addition to the latter, $Den_{<4um}/Den_{Total}$ for detector C2-H5 is > 79% (see table 12(b)). Also, the MT value of detector G2 fails to drop as the concentration of Te inclusions increases and Zn concentration decreases. This is partially due to the fact that even though the size range increases, its volume % remains significantly low throughout the sample (graph 3&4). This anomaly in the relationship between volume % of given detectors and MT values does not cancel out the importance of volume % in a detector, but emphasizes the significance of distribution and population of Te inclusions throughout the sample.

Table 12(b): Averages from CG59.BD1 samples (table 11(a)) MT and Resistivity are average from table 11(a) above Courtesy of CMR

MT (1.5us shaping) cm^2/V	**1.11 E-03**
Resistivity (Ω.cm)	**2.80E+10**
P/V; ^{57}Co	**1.68**
Vol % (%)	**0.0084**
Vol % >4um	**0.0080**
Den (Counts/cm^3)	**545325**
Den >4um	**106603**
$Den_{<4um}/Den_{Total}$ %	**79.9 %**
$Den_{<6um}/Den_{Total}$ %	**20.1 %**
Ave D (um)	**3.50**
Ave D >4um	**7.61**

Lastly, but not least, there is a significant decrease of MT value in sample H5 which is extracted within the heel where Zn concentration is low and so is the resistivity. A decrease in resistivity raises dark current, reduces the depleted layer of the detector, and results in an unconventional increase of electric field, which in turn drops the MT value. This detector's SSD results in graph 3&4 cannot explain sufficiently the reason for a drop in MT value. A decrease in Zn concentration in conjunction with a drop in resistivity and an increase in leakage current

can sufficiently explain this decrease of MT value. Still, this drop of MT value is partially associated with a sharp peak of volume % between size range 55-75 in a low population density <40 counts/cm^3. This again expresses the impact of bigger inclusions regardless of their count or density in a detector.

In addition, the variation of resistivity and MT values along the radial parameter in this ingot is somehow uniform and this is credited partially to higher crystal homogeneity. In fact, sample E1, and E4 measured a close MT and resistivity value, as well as a close P/V ratio of gamma spectrum with 0.5 micro-second shaping time and ^{57}Co source as reported in table 12(a). Te inclusions' SSD in these two samples is uniform as well; the counts, volume %, and average diameter of Te inclusions of average diameter >1um and >4um are approximately the same. They are bound within the same % error bar of 5-8%. On the other hand, samples C2 & D5 have almost the same SSD as E1 and E4 discussed above.

Furthermore, GDMS report for CG59 shows low or no deep donor level impurity [see table 29 in the APPENDIX B]. This gave an edge to passivated Te_{Cd} and In_{Cd} impurities that are more favored in CZT in order to yield a better compensation scheme. The following facts are evident in CG59 ingot: recorded resistivity of all tested samples is greater than 10^{10} Ω.cm; reported deep level, Carbon, nitrogen, and oxygen (CNO), and total impurity values are low; and total twin and sub-grain boundaries are sparse (these yielded higher percent single crystal samples). A fresh experimental fact from SSD analyses of CG59 detectors now suggests that MT values are severely affected by increasingly widening distribution throughout the sample along the growth direction. An increase of average Te inclusion sizes towards the heel further inhibits electron mobility, hence lowering the reported MT values. A decrease in Zn concentration towards the heel is also a factor which reduces resistivity, as well as MT values.

Given Sample CG64.Edge4, which had an uncluttered, evenly distributed population of Te inclusions with a small size range (1-10um) and the best MT value of 0.009 cm^2/V, one can claim that the overall effect of MT values (and other electrical properties) of all cut samples from CG51, 58, 59, & 67 is a result of inclusions with average diameter >4um. CG59 samples are uncluttered and the smaller inclusions (<10um) are almost uniformly distributed. The large Te inclusions are sparse, but their count increases along the growth direction. It is then these larger inclusions which lower the MT value from 0.009 to 0.002 cm^2/V. From this set of information, it can be proposed that the larger the inclusion, the more strongly it attracts impurities which induce poor compensation and hence lower the MT value. This larger inclusion further deforms localized areas of the crystal structure. It is highly possible that experimental results for an electric field of a detector with these larger inclusions will show non-uniform distributions within and around it; electric field concentrations would be higher at those localized points where large inclusions reside as well as its neighbors. The impact of these large inclusions, which are partly voids and inclusions) can further be exacerbated by micro-cracks.

One major factor drawn from this study is that the effect of Te population density and their distribution can be explored in the light of establishing a correlation with MT values across the ingot. The variation in inclusion size range distribution can further be explored to establish a correlation within an ingot. Keep in mind that these findings are bounded by conditions such as purity, higher resistivity $>10^9$ Ω.cm, single crystals and growing conditions. Subsidiary conditions that strengthen this experimented correlation are drawn from SSD analyses and include the nature of Te inclusions' distribution; is it wide? is it narrow? is it cluttered? is it uncluttered?

In simple terms, the change in distribution from wide to widest in CG59 is a factor which contributed to increase of MT values towards the heel. As for general correlation across the ingots ($Den_{<4um}/Den_{Total}$ %) is by far a better correlation between MT value and SSD results. This values applies to reported CG67, CG58, and CG59 SSD results above. In all cases, $Den_{<4um}/Den_{Total}$ is greater than 75% (in exception to CG58_F1) and this gave them an MT value close to or > 0.0015 cm^2/V. At >80 %, the MT value is close to or > 0.002 cm^2/V. The best MT value of 0.09 cm^2/V is finally given by $Den_{<4um}/Den_{Total}$ >99%

II Result & Analysis: CG78 & CG80 Ingots

A number of slices were cut radially from the heel and shoulder of these two ingots, CG78 and CG80 [Figure 18(a&b)], among them slices 2 and 3. Results from these two slices are reported in this thesis. A number of samples from slice CG78.R2 are also reported. These samples were tested for IV and MT measurement. Results from IV include resistivity. Results from multichannel analysis (MCA) include MT values and P/V ratio. The same test was conducted on detectors cut from CG78.R2 slice. CG78.R3 and CG80.R2 slices [figure 18(c&d)] are also IR mapped. A number of regions which are single crystals are randomly selected and tested for SSD analysis.

CG78.R3 selected regions were compared and confirmed uniformity and continuity of SSD of Te inclusions in CZT. Also, selected regions Q(AB, BC, AD, & CD) in CG80.R2 slice, some of which are in close proximity to CG78.R3 region given below, are examined [figure 18(d)]. These results were further correlated to the MT values of detectors cut from CG80.R3 Slice, which also must have the same features as CG80.R2's AOI. Regions studied in CG78.R3 slice included varied AOI within quadrants, Q_(AB, BC, AD, CD, M [M is AOI at the center]).

Courtesy of CMR

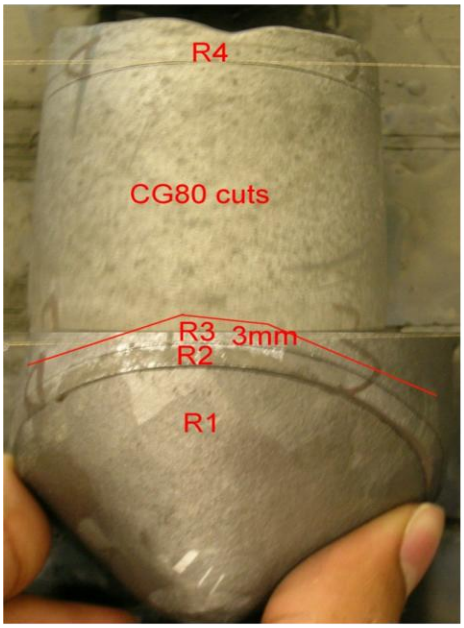

Figure 18(a): CG80(R2&R3) radial cut within the shoulder ~ (R3: Samples cut for MCA measurement. R2: General IR mapping)

Figure 18(b): CG78(R2&R3) radial cut within the shoulder ~ (R2: Samples cut fort MCA measurement and IR mapping; R3: General IR mapping)

Courtesy of CMR

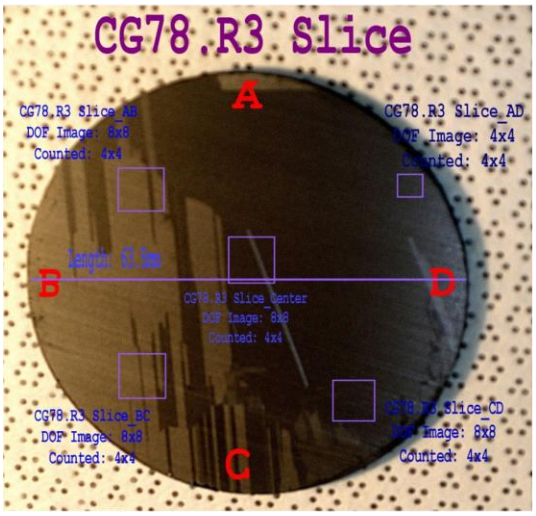

Figure 18(c): CG78.R3 Slice; IR Mapped region on Slice 3. Region includes: CG78.R3 Slice_(AB, BC, AD, CD & Center or M). Frames counted for Te inclusion distribution and size analysis: 4x4. Dimension of each frame: 0.49x0.49 (mm^2)

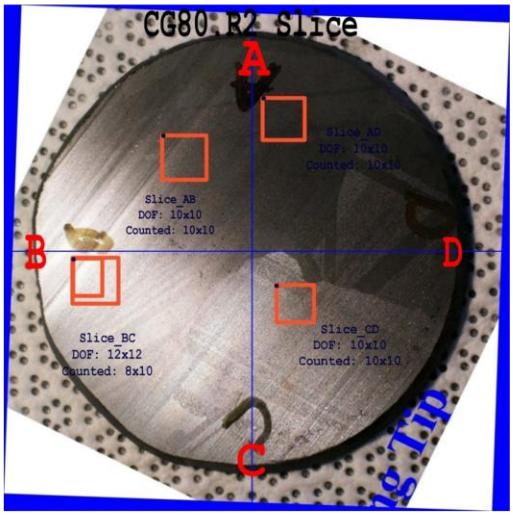

Figure 18(d): CG80.R2 Slice; IR Mapped region on Slice 2. Region includes: CG80.R2 Slice_(AB, BC, AD & CD. Frames counted for Te inclusion distribution and size analysis: 4x4. Dimension of each frame: 0.49x0.49 (mm^2)

Samples studied from CG78.R2 slice are CG78.R2.(13_BC, 17_CD, 32_AD, 36_CD, & 44_CD); AB, BC, etc stands for the corresponding quadrant from which the respective samples were extracted.

A uniform area of 0.04 (mm^2) for 4x4 frames DOF image of 0.49x0.49 (mm^2) dimension was studied in each AOI CG78.R3_(AB, BC, CD, AD & M) & CG80.R2_(AB, BC, AD, & CD).

Table 13: CG78.R3 Slice Te Inclusions SSD Overview. Slice thickness ~ 0.27 cm; Area of Interest (AOI) ~ 0.04 cm^2

	AB	BC	AD	CD	Center (M)	Units
T. Count	4948	2952	4014	3691	3595	#
In Range	2269	1640	1854	1901	1898	#
Den	219651	158760	179477	184027	183736	**#/cm^3**
Den>4um	111326	74443	109487	105614	96805	**#/cm^3**
Vol%	0.0075	0.0070	0.0093	0.0137	0.0093	**%**
Vol%>4um	0.0073	0.0069	0.0093	0.0136	0.0092	**%**
Vol%,error	0.0004	0.0004	0.0005	0.0006	0.0005	**(+/-)**
AveD	6.22	6.27	7.36	7.59	6.79	**um**
AveD>4um	9.74	10.69	10.39	11.30	10.74	**um**
Den ~ Density, Vol % ~ Volume %, AveD. ~ Average diameter						

Table 14: CG80.R2 Slice Te Inclusions' SSD Overview. Slice thickness ~ 0.25 cm; AOI ~ 0.04 cm^2

	AB	BC	AD	CD	Units
T. Count	3578	4773	4870	3880	#
In Range	2590	2718	2574	2279	#
Den	267539	280761	265886	235414	**#/cm^3**
Den>4um	241302	146888	168684	179737	**#/cm^3**
Vol%	0.012	0.0098	0.0095	0.0095	**%**
Vol%>4um	0.012	0.0096	0.0094	0.0095	**%**
Vol%,error	0.001	0.0009	0.0008	0.0005	**(+/-)**
Ave D.	8.32	6.45	7.01	7.74	**um**
AveD.>4um	8.96	10.09	9.69	9.42	**um**

These selected AOI are free from potential high percentage of debris, scratches, and grain boundaries. AOI Q_CD shows a high volume % of Te inclusions in CG78.R3 slice [table 13]. This is followed by Q_AD, Q_M, Q_AB, and finally Q_BC [table 13]. Volume % of Q_M, Q_AD, Q_AB, and Q_BC are approximately the same. As for CG80.R2 slice, Q_AB is the highest and Q_BC, Q_AD, and Q_CD volume % are approximately the same [table 14].

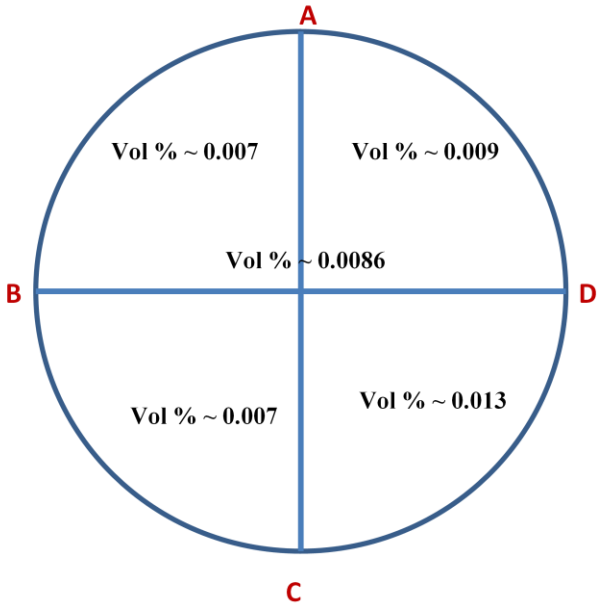

Chart 1: CG78.R3 slice volume % overview ~ Q's; AB, AD, CD, BC, & ACN.

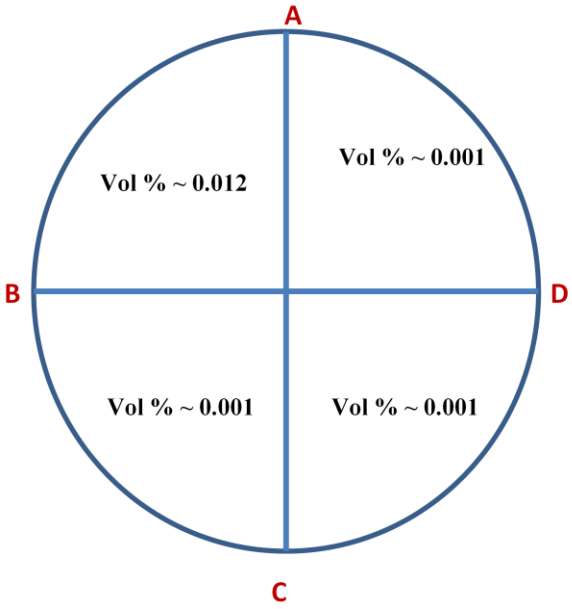

Chart 2: CG80.R2 slice volume % overview ~ Q's; AB, AD, CD, BC, & ACN.

A detailed tread of these variations in volume % between AOI studied in CG78.R3 and CG80.R2 slice is shown in chart 1 and 2 below. Region AB, which is the hot side of both slices shows a decrease in volume % in CG78.R3 slice as compared to CG80.R2 slice (CG78 ingot was cooled at a faster rate than CG80). On the contrary CG80.R3_AB shows a significant increase of Te inclusion volume %. This suggests that thermo-migration of Te inclusions and voids is more favorable in cases where cooling takes place at a slower rate. This rate also favors nucleation and growth of Te inclusion, which happens at a much lower melting point than that of CZT (<450 °C).

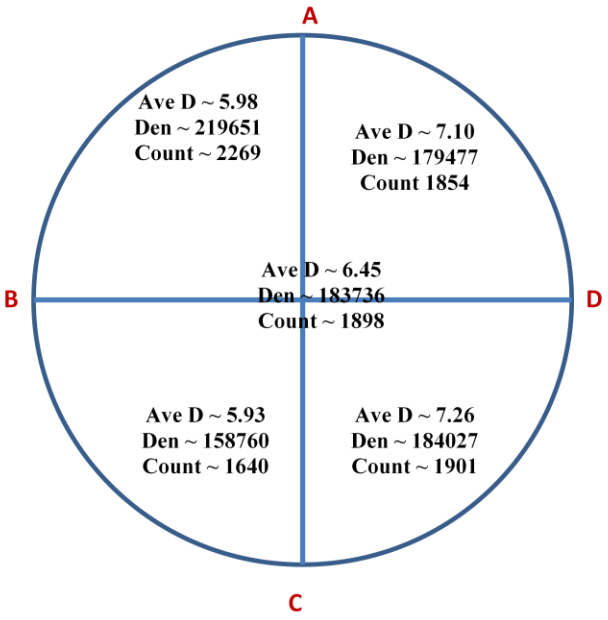

Chart 3: CG78.R3 Slice diameter, count, and density overview. Average diameter (Ave D) in Micron; Density (Den) in count/cm^3

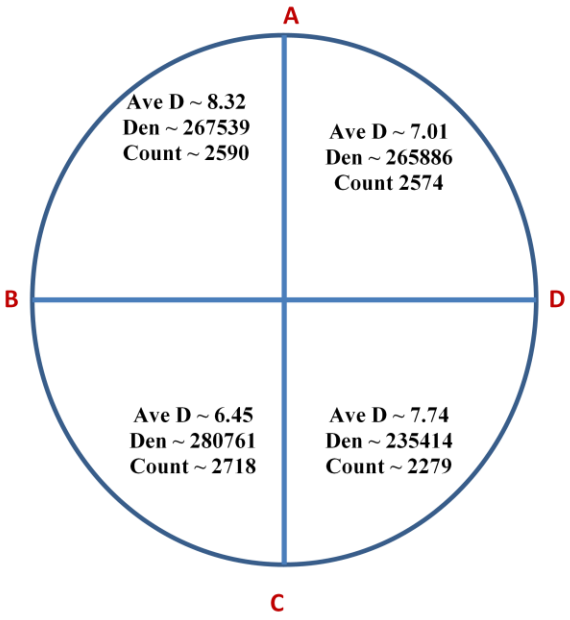

Chart 4: CG80.R2 Slice diameter, count, and density overview. Average diameter (Ave D) in Micron; Density (Den) in count/cm^3

In reference to table 13 and 14, "Total Count" records the number of inclusions, debris, and dark background specs estimated to be present in a given acquired DOF image. "In Range" counts only an estimated number of features that exhibit Te shape and characteristics discussed earlier

These two tables show a standard result of both CG78.R3 and CG80.R2. From both tables, it is shown that Te inclusions' count, density, and average diameter from CG78.R3 AOI(s) are lower than that of CG80.R2 in all four Q's (see charts 3&4). This increase in Te inclusions' SSD properties is suspected to be a major cause of

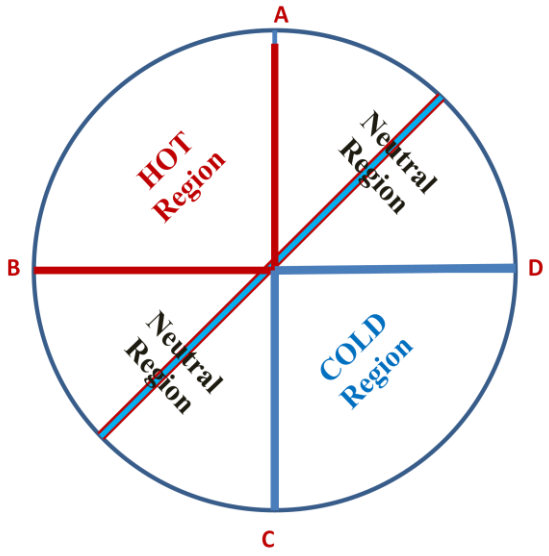

Chart 5: CG(78&80) representations of hot to cold Q's. Both ingots were cooled with a horizontal gradient of 100°° C

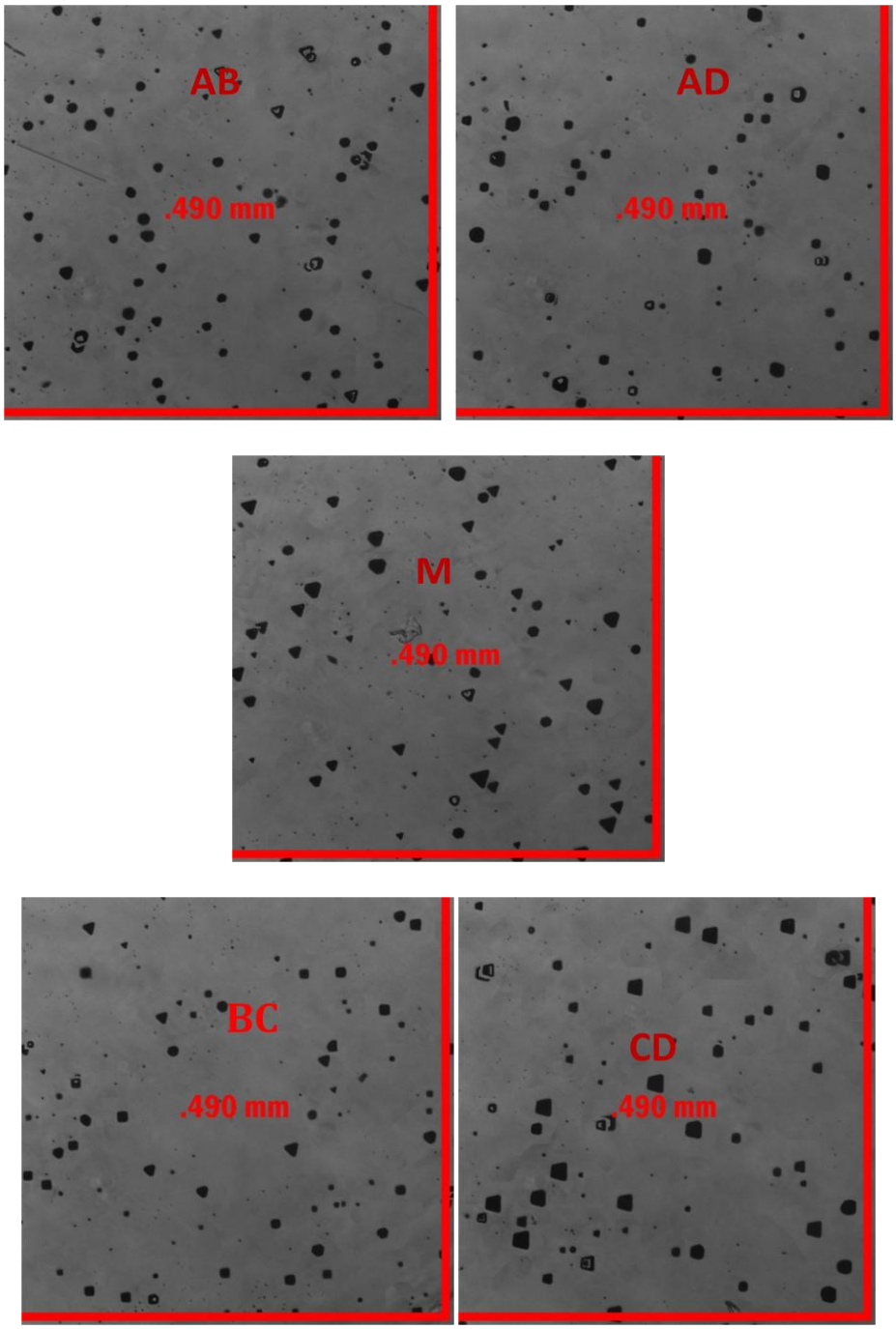

Figure 19(a): Selected Single DOF Image from CG78.R3 Slice_(AB,AD,M,BC,&CD. M is also known as the Center.

poor optical and electrical properties reported in CG80.R3 detectors as compared to CG78.R2 detectors (see table 15-19 for further clarity well). Figures 19(a) give a number of selected DOF

images taken from AOI(s) studied in CG78.R3 slice. Figure 19(b) are images from CG80.R3 slice AOI(s).

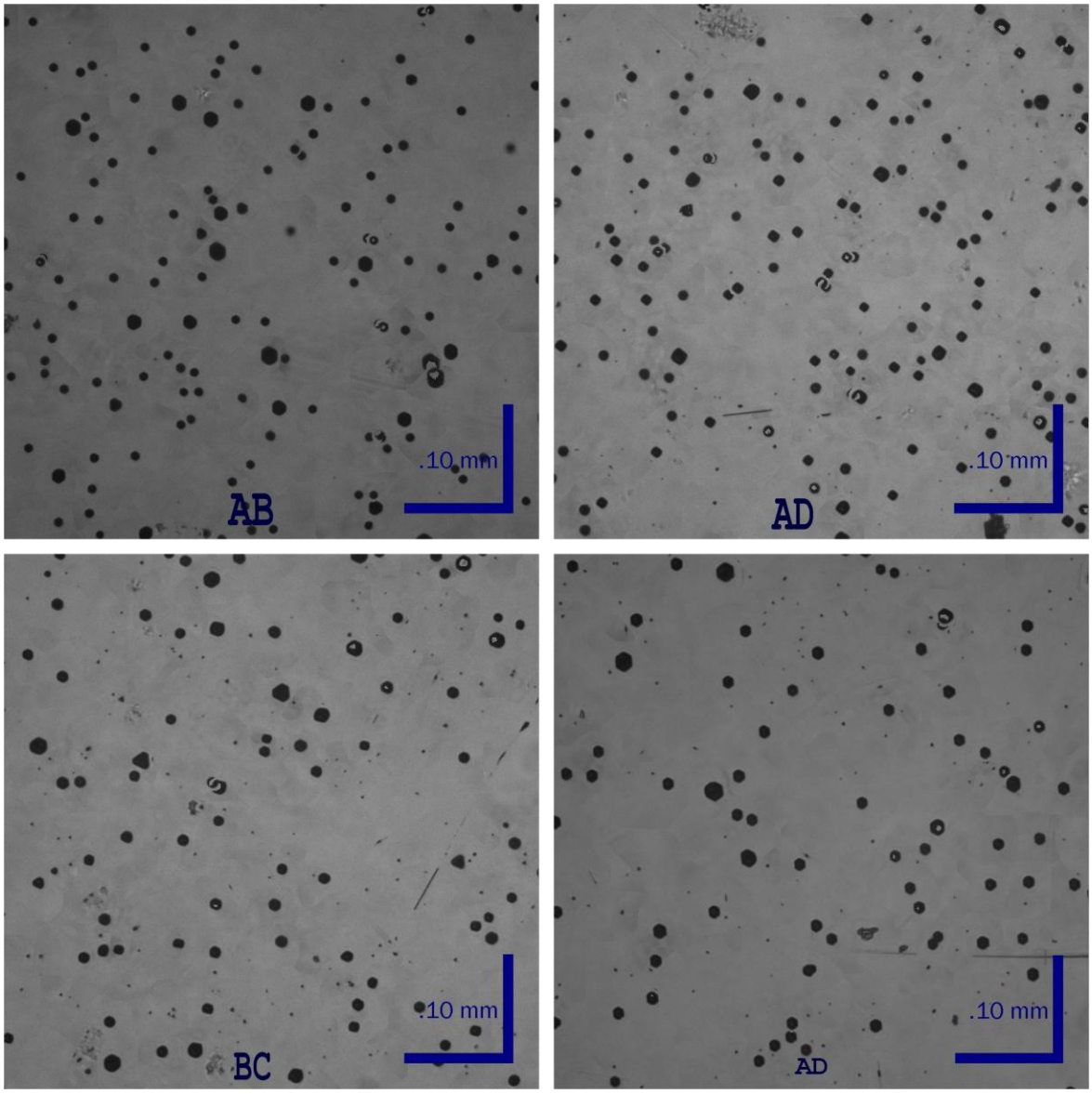

Figure 19(b): Selected single DOF image from CG80.R2_AB, AD, BC, & CD.

Charts 6 and 7 list the unique pattern of evolution of Te inclusions' SSD given in Figures 19(a) and 19(b) respectively. Chart 5 gives a schematic temperature difference in all four

quadrants during growth of CG78 and CG80 ingots (these two ingots were cooled with an imposed temperature gradient of 100 °C within the shoulder of the ingot).

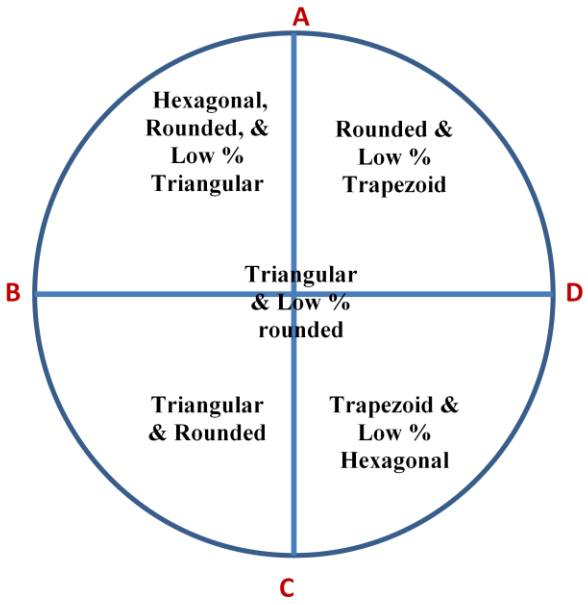

Chart 6: CG78.R3 Slice shape distribution

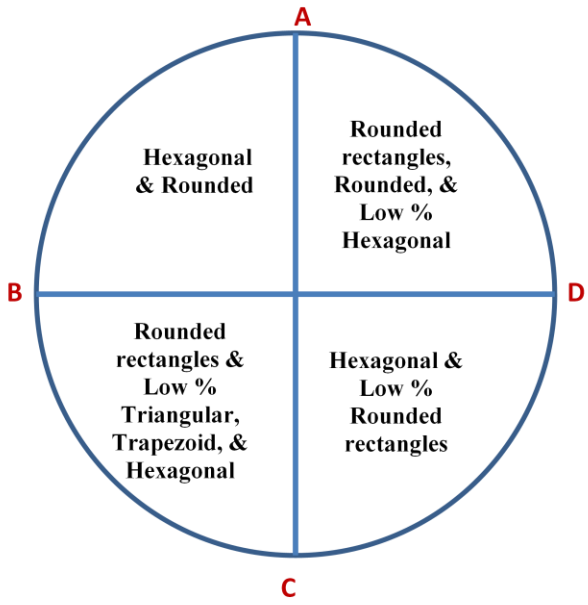

Chart 7: CG80.R2 Slice shape distribution

An overview of the shape of Te inclusions present in CG78.R3 slice reveals that inclusions' shapes are varied from region to region. The transition of shape observed from one quarter to the next is consistent. The majority of Te inclusions in Q_AB [figure 19(a)] are hexagonal and rounded, with a minority of triangles. Q_AD is heavily populated by rounded inclusions, but the previous quadrant's minority of triangles is now reshaped into trapezoids. These shapes are repeated in Q_CD as well, but now the percentage of hexagons is lower and the trapezoids are more numerous. Triangular inclusions reemerged in Q_BC, and are almost evenly mixed with rounded inclusions. A low percentage of hexagons are seen as well. At the center, inclusions take on an almost exclusively triangular shape with a small representation of round and no trapezoids.

In general, the pattern of shape evolution of CG78.R3 seems to be as follows: rounded and hexagons turn into trapezoids; triangles turn to trapezoids; trapezoids turn to triangles (while maintaining blunted edges). One can claim that this evolution of shape is consistent with the imposed temperature gradient of 100 °C applied during cool down of the crystal ingot (see chart 5). It is also consistent with the fact that the growth of this ingot was Te diffusion-controlled as the excess Te competed to occupy available Cd vacancies [25]. Feature shown in figure 19(a) with varied shapes are then Te-rich inclusions surrounded by unconventional void fractions. As shown in Chart 5, a lower temperature applied around Q_CD favors high nucleation of Te inclusions and voids as they diffuse throughout the ingot. The breakdown and simultaneous recombination of Te inclusions could have resulted in a more rapid transformation of shape and increase in size. A higher temperature applied around Q_AB favors a higher rate of inclusion breakdown, but less transformation in shape. It is possible that this resulted in decreased size and a higher number of inclusions.

Chart 3 (direct results from CG78.R3 Slice [AB, BC, CD, AD & ACN]) further supports the above argument by demonstrating a significant gap of population densities between Q_AB and Q_CD; Q_AB, which was 100 °C warmer than Q_CD during cool-down, not only has a larger population density, but also a much smaller average diameter of Te inclusions than the colder Q_CD. The line in temperature difference is further illustrated by the clear transition of inclusions' average diameter from Q_AB to the center to Q_CD: a clear increase in diameter.

On the other hand, the pattern of shape evolution of CG80.R2 from Q_(AB-AD-CD-BC) is almost non-transformable with the exception of a few inclusions which seem to barely turn into triangular and/or trapezoids. Q_AB is primarily dominated by hexagonal and rounded inclusions. Hexagonal inclusions' edges seem to have dissolved into the CZT matrix and hence

turn into rounded rectangles and/or rounds. Q_BC and Q_AD, which are neutral zones, have Te inclusions with relatively the same shape; rounded rectangles, rounded, and a low percentage hexagonal. An extended time that was applied in cool-down must have allowed optimal saturations of Te inclusion throughout the ingot resulting in shape uniformity (see figure 19(b)). This could have allowed more time for transformation of Te inclusions, hence increasing their population and average diameter. Also, a much smaller amount of excess Te in this ingot during growth may have resulted in Cd vacancy controlled growth. This resulted in the increase of void fractions comparable to that of Te, which subsequently grew as the size surpasses that of critical nucleus [25].

Graphs 5&6 give various plots which compare the results from relative Q's of CG78.R3 and CG80.R2. All 4 plots in graph 5(a,b,c,&d) for Q_(AB, AD, BC, & CD) respectively show an increase of volume % almost throughout the given AOI(s). Q_M of CG78.R3 is also included in graph 5(d). It is comparative to CG78.R3_BC. An increase in population density of Te inclusions in CG80.R2 compared to CG78.R3 throughout AOI of respective Q's is shown in graph 6(a,b,c,&d). The plots also show a narrowing of distribution range throughout given AOI(s). Both Q_BC of CG78 and 80 have a bimodal distribution as well as CG80_AD and CG78_AB. Others have either a trimodal or multimodal distribution. This distribution contrast may relate to the radial parameter of these AOI(s). The presence of twins and grain boundaries contributed less, but notable effects slightly skewed size distribution ranges and gave those plots a multimodial distribution (the effect of a radial cut slice with uniform Te inclusion distribution).

Variation in temperature and pressure around Te inclusions could have contributed towards this slight non-uniform distribution of Te inclusions within the shoulder. Note that the concentration of inclusions, especially those in CG80.R2 that have a narrowed size distribution

could force the conclusion that Te inclusions have a normal orientation. However this may not be the fact, and if it is, then this orientation is limited to a short range as shown in figure 19(b).

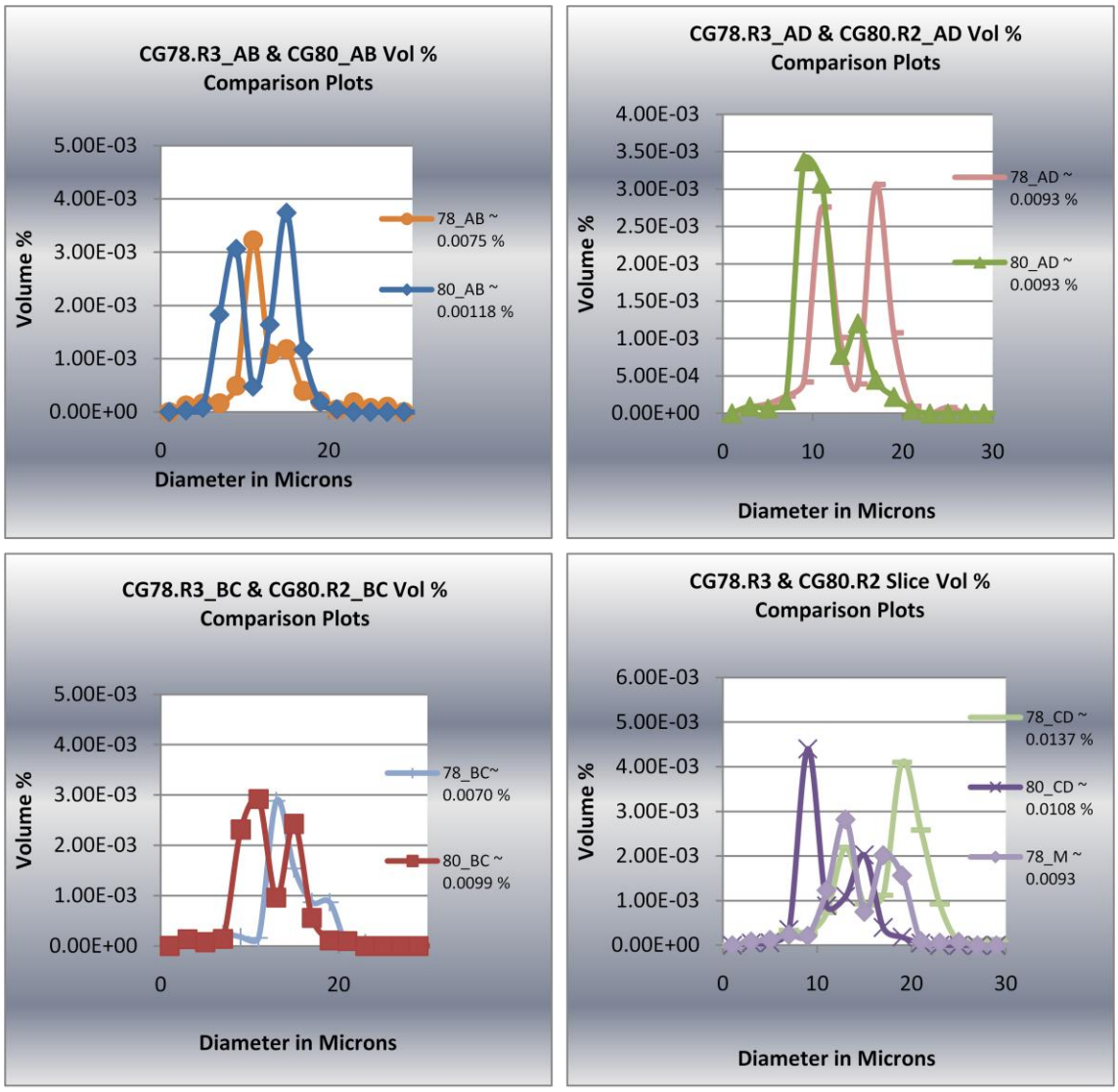

Graph 5: from top left ~ 5(a,b,c,&d)

The total impurity level of CG78 compared to that of CG80 is much greater than that of CG78 [APPENDIX B]. This contradicts a possible claim, which might suggest that a partial effect of poor MT values in CG80.R3 detectors is a direct result of this high levels of impurities.

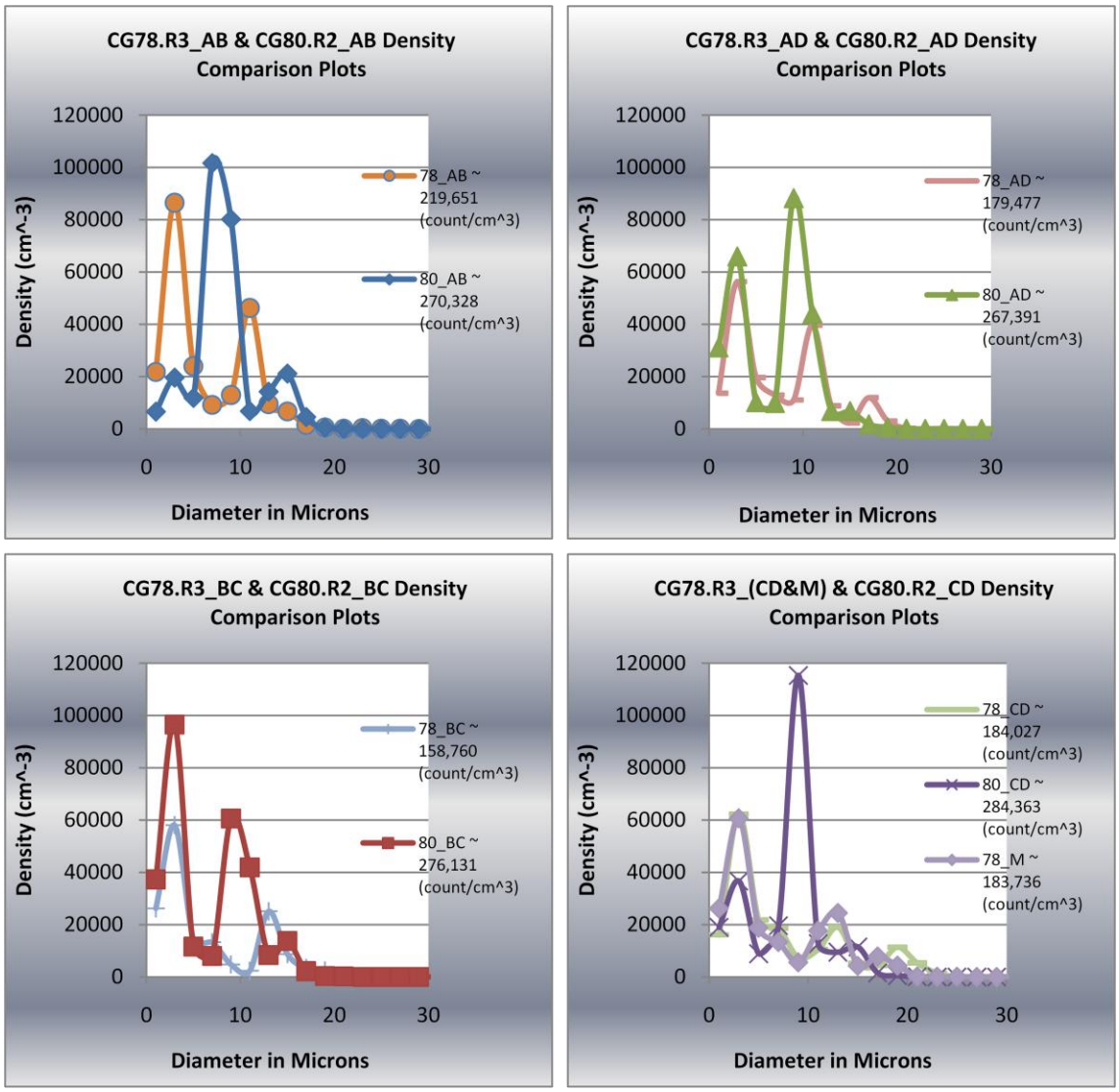

Graph 6: from top left ~ 6(a,b,c,&d)

Table 15: CG78.R2 Properties Overview — Courtesy of CMR

	BC		CD		AD		AB	
CG78.R2.Overview	5	13	9	17	32	33	36	44
Thickness (mm)	2.35	2.29	2.45	2.34	2.39	2.43	2.36	2.33
Contact Area (mm^2)	51.18	51.12	50.26	50.26	51.05	50.76	50.33	50.68
MT (1.5 shaping) ~ 10^{-3}	NA	1.55	1.03	1.18	1.36	1.28	1.16	0.72
Resistivity (Ω.cm) ~ 10^{10}	1.56	2.84	2.46	2.71	3.30	3.16	3.20	3.46
14KeV peak Visibility; ^{57}Co	Poor	Good	Fair	Good	Good	Good	Good	Good
P/V; ^{57}Co	NA	1.67	NA	1.96	1.58	1.24	1.78	1.69

Table 16: Te Secondary Phases Overview (Area counted ~ 0.24 cm^2)								Courtesy of CMR
Count		37096		17765	29636		11045	29191
Volume % (%)		0.0074		0.0130	0.0092		0.0084	0.0076
Volume % >4um		0.0072		0.0129	0.0091		0.0083	0.0075
Density (Counts/cm^3)		283722		230648	255124		200708	279061
Density >4um		132169		159059	155869		116245	139049
$Den_{<4um}/Den_{Total}$ %		53.4 %		31.0 %	38.9 %		42.1 %	50.2 %
$Den_{<6um}/Den_{Total}$ %		46.6 %		61.0 %	61.1 %		57.9 %	49.8 %
Ave D (um)		5.41		7.55	6.65		6.74	5.77
Ave D >4um		8.70		9.76	9.28		9.72	8.89

However the concentration of Fe around the tip where both slices (CG78 and CG80) were cut is significantly high in CG80 [APPENDIX B]. In theory, the reported discrepancies between the qualities of the detectors extracted from these two ingots more strongly point to Te inclusions' SSD. These factors include: an increase in average diameter and an increase in Te inclusion population density and Vol %.

Table 17: Averages from CG78.R3 Slice (AB,BC,AD,CD,M) MT and Resistivity are average from table 15 above	Courtesy of CMR
MT (1.5 shaping) cm^2/V	1.11 E-03
Resistivity	2.80E+10
P/V Co-57	1.68
Vol % (%)	0.0093
Vol % >4um	0.0093
Den (Counts/cm^3)	185130
Den >4um	99535
$Den_{<4um}/Den_{Total}$ %	46.3 %
$Den_{<6um}/Den_{Total}$ %	53.7 %
Ave D (um)	6.85
Ave D >4um	8.71

Worst of all, a decrease in $Den_{<4um}/Den_{Total}$ from 46% in CG78 detectors to 30% must have contributed to weakening or nullifying of CG80 detectors (see table 15,16&17). This increase of Te population density and average diameter is much more damaging than a positive narrowing of size distribution as given by graphs 10 and 11. The imposed gradient during ingot cool-down also seems to have contributed towards weakening or strengthening of the detector properties.

Q_AD (neutral Q) in CG78 reported a fair quality detector compared to Q_BC (neutral Q), which is complimentary to the former. Detectors from Q_AB (hot Q) and Q_AD (neutral Q) had better visibility of 14KeV peak than those from Q_BC (neutral Q) and Q_CD (cold Q) [table 15]. This visibility of 14KeV peak is only better in detectors from the hot Q of CG80.R2 (see table 18). The results of CG80.R2 detectors, however, are below CMR standards [table 18&19].

Table 18: CG80.R3 Samples Properties Overview

	Cold				Hot			
	BC		CD		AD		AB	
CG80.R3.Overview	5	6	7	8	19	20	22	23
Thickness (mm)	1.61	1.6	1.67	1.73	1.82	1.77	1.82	1.89
Contact Area (mm^2)	67.06	67.97	65.12	65.73	69.14	69.55	68.34	68.31
Resistivity (Ω.cm)	2.93E+10	3.05E+10	2.70E+10	2.56E+10	1.00E+06	1.24E+10	2.18E+10	2.03E+10
MT (1.5 shaping)	3.30E-04	8.61E-04	7.21E-04	4.92E-04	NA	6.42E-04	8.12E-04	6.92E-04
P/V	NA	NA	1.20	NA	NA	NA	NA	1.40
14KeV peak visibility	fair	fair	fair	fair	NA	Good	Fair	Good

Referring back to tables 15-17 which are both MCA and IR results for regions studied in CG78.R3 and CG78.R2 detectors, an increase of $Den_{<4um}/Den_{Total}$% in CG78.R2.36 in Q_AB compared to CG78.R2.13 in Q_BC further supports a theory that it is Te inclusions with average diameter >4um that hinder the electron mobility. There is in fact a fair correlation across the 4 given detectors in table 15 (excluding CG78.R2.44_AB). This claim is further supported by CG80 detectors'

Table 19: Averages from CG80.R2 Slice. MT and Restively are average from table 18 above

MT (1.5 shaping)	0.65 E-03
Resistivity	2.21E+10
P/V Co-57	1.15
Vol % (%)	0.0103
Vol % >4um	0.0102
Den (Counts/cm^3)	262400
Den >4um	184153
$Den_{<4um}/Den_{Total}$ %	29.4
$Den_{<6um}/Den_{Total}$ %	70.6
Ave D (um)	7.38
Ave D >4um	9.54

values. In contrast to CG64.Edge4 sample that had a better MT and Te inclusion $Den_{<4um}/Den_{Total}$ of 99%, the MT values given by CG78 and CG80 detectors decreased as a result of decreasing $Den_{<4um}/Den_{Total}$ to <50%. The size distribution range in studied regions in CG78.R3 slice were narrowed compared to CG59. This would generally help in improving detector properties, but this is not the case: the average diameter of all counted Te inclusion in CG78 samples was >5um.

Almost every region studied in CG78.R3 shows that $Den_{<4um}/Den_{Total}$ is <50% and $Den_{<6um}/Den_{Total}$ is <65%. The majority of Te inclusions fell within 4-10um size range. CG78 detectors had an average of ~$1.11*10^{-3}$ cm^2/V. A decrease of $Den_{<4um}/Den_{Total}$ in CG80 detectors to a value <35% further dropped the MT value to $6.5*10^{-4}$ cm^2/V or less. An additional decrease of $Den_{<4um}/Den_{Total}$ % will completely ruin a detector.

III Result & Analysis: CG92 & CG93 Ingots

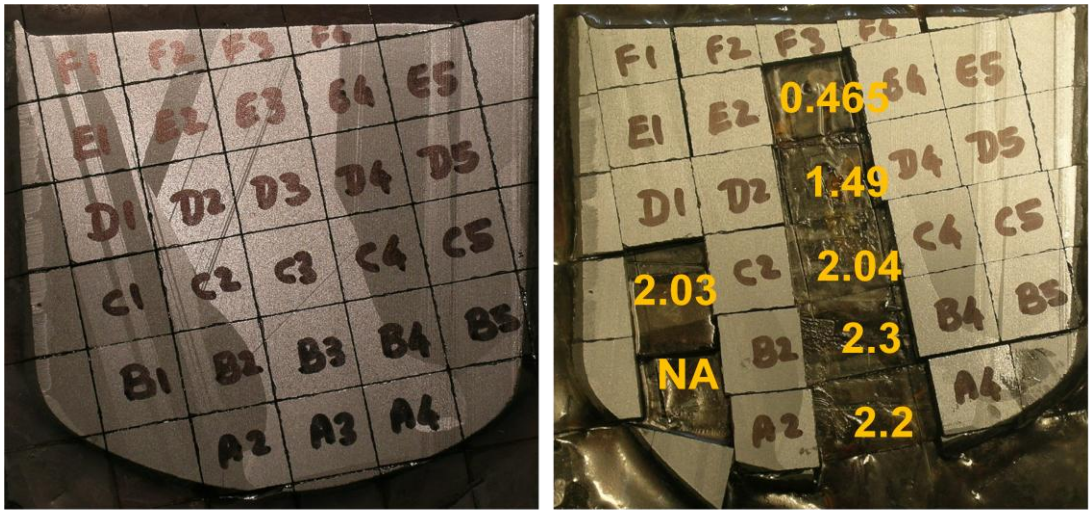

Figure 20: Marked slice on the left represents CG92 sample cuts. The next slice, still CG92.BC.CD2 Slice represents MT values in $x10^{-3}$ cm^2/V for samples A3,B3,C3,D3,E3,C1,&B1.

Courtesy of CMR

Figure 20 shows a number of tested samples for MCA and IR mapping of CG92 ingot. Along column 3, there seems to be a linear increase of resistivity and MT value as shown in figure 20 and table 20. Sample E3 and D3 had a multigrain and a twin respectively with overcrowded large-sized Te inclusions. The increase, however, of volume % for sample A3-D3 is barely noticeable and falls within the same error bar. Graph 7 still shows an inconsistent distribution of volume % of single crystal detector A3-C3. Similar to CG59, the increasing size range of Te inclusions in CG92 is pertinent to decreasing MT value.

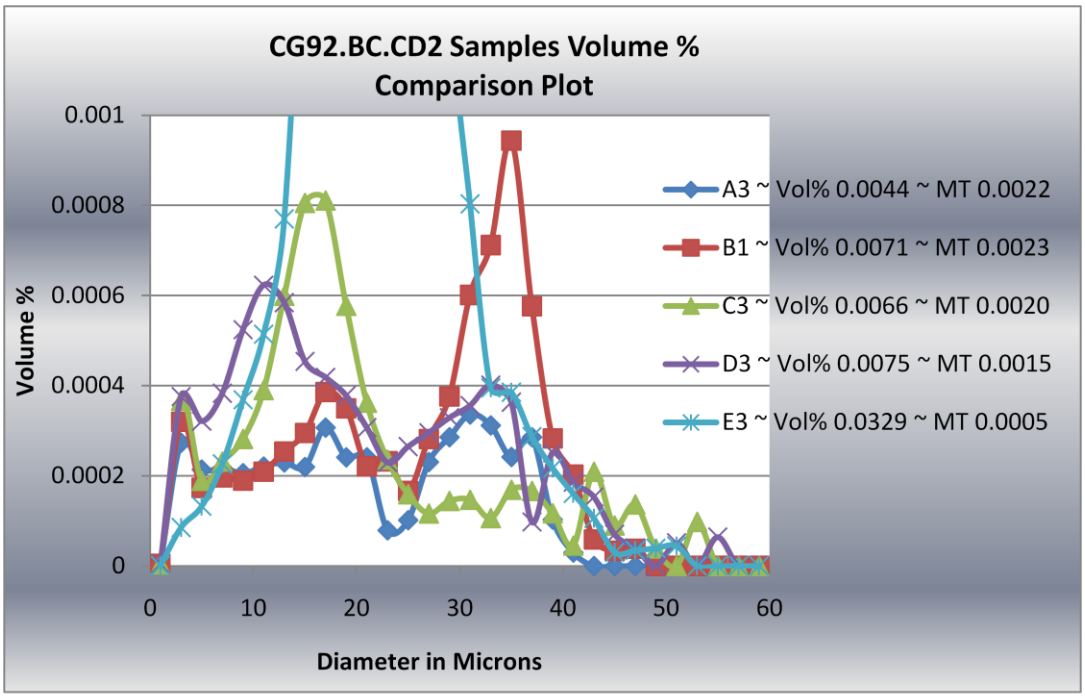

Graph 7: Te inclusion volume % distribution is inconsistent with decreasing MT value from A3-E3. Apart from E3, the volume % range of A3-D3 detectors is significantly small.

Tiled DOF image of detector D3 shows Te inclusion growth instability in one of its corners. This must be an effect of inclusions migrating towards a twin which crosses the detector on the far top left as shown in figure 20. Another growth defect reported in this detector

is a line defect. There is a higher population density of disoriented lines in some fractions of the CZT ingot as noted in studied detector's AOI (or various slice AOI), especially in the region far from low energy sites given by the grain boundaries.

This is unique and recently reported in excess Cd grown ingots. Note that other cases where line defects were earlier reported in small percent seem to have taken a more uniform pattern around a twin boundary. Possible causes of these line defects could be a result of dissolved Te inclusion in the CZT matrix. These lines could then disorient themselves in micro-channels which were formed by formation of CdTe before it integrated into the CZT matrix during cool-down process. Remnants of unstable Te of sizes smaller than that of critical radius, could have dissolved into the CZT matrix to form these disoriented lines. Solvent nuclei of unreacted Te, small in size, could have also failed to overcome the threshold size which would allow for transformation [24] into Te inclusions, hence partially dissolving into the CZT matrix.

Table 20: MCA and SSD Results for CG92 samples. MT ~ cm^2/V; ρ ~ Ω.cm; Den ~ $count/cm^3$; AveD ~ um

	Count	Den	Den >4um	$Den_{<4um}/Den_{Total}$	Vol %	Vol % >4um	AveD	AveD >4um	MT (10^{-3})	ρ (10^{10})
A3	40410	335105	60329	82 %	0.0044	0.0041	3.35	7.62	2.2	3.33
B3	52240	366051	54894	85 %	0.0071	0.0068	3.39	8.70	2.3	2.49
C3	63657	399556	71278	82 %	0.0066	0.0062	3.71	8.91	2.0	3.33
D3	61427	451973	106093	77 %	0.0075	0.0071	3.81	7.95	1.5	1.32
E3	31243	198653	122614	38 %	0.0329	0.0328	9.85	14.35	0.5	0.88

Furthermore, the size of formed voids could have later shrunk or grown; if the size of formed "bubble" or void is greater than that of critical nucleus, then the void would grow; otherwise the size shrinks [25].

Therefore, the presence of small percent line defects in detector D3 could also have been a factor that lowered the measured MT value. Next, the poor MT value of E3 is directly related to overcrowding of Te inclusions in half of the detector AOI (Figure 13 discussed in CG59's results is a fraction of detector E3 IR image).

Table 21: CG92.BC.CD.2 Properties Overview					Courtesy of CMR
	A3	B3	C3	D3	E3
Thickness (mm)	2.21	2.15	2.27	2.17	2.25
Contact Area (mm^2)	87.46	90.15	90.21	90.8	92.73
Resistivity (Ω.cm)	3.33E+10	2.62E+10	1.82E+10	1.32E+10	8.75E+09
MT (cm^2/V)	2.20E-03	2.30E-03	2.04E-03	1.49E-03	4.65E-04
P/V ratio	Nil	Nil	Nil	Nil	Nil
14KeV peak visibility	Good	Good	Good	Poor	Poor

Worst of all, more than 62 % of these inclusions have a diameter >4um. This is automatically far over the limit that favors production of a detector with standard properties. A drop in resistivity is a direct result of high concentration of Te inclusions and low Zn concentration.

Table 22: Averages for CG92.BC.CD.2. (A3,B3,C3)	
MT (cm^2/V)	**2.18 E-03**
Resistivity	**2.59E+10**
P/V	
Vol % (%)	**0.0064**
Vol % >4um	**0.0061**
Den (Counts/cm^3)	**388172**
Den >4um	**73149**
$Den_{<4um}/Den_{Total}$ %	**83.1 %**
$Den_{<6um}/Den_{Total}$ %	**16.9 %**
Ave D (um)	**3.56**
Ave D >4um	**8.30**

Table (21&22) gives electrical properties of CG92 detectors. Detector A3-C3 had good visibility to 14KeV peak given ^{57}Co as an electron excitation agent, but nil P/V ratio. This effect suggests that these detectors, extracted from Cd-rich grown ingots, can only resolve electrons.

The reported $Den_{<4um}/Den_{Total}$% of 83.1% in detectors A3, B3, and C3 resulted to a competitive MT value relative to those given by a number of CG59 detectors of $>2*10^{-3}$ cm^2/V. The volume % and average diameter of most samples in CG92 detectors which match the detectors in CG59 values are within the same error bar [table 20], thus backing their standard $Den_{<4um}/Den_{Total}$ of 83.1 %. However a decrease in size range distribution seems to have favored a slight increase of MT value. Other factors that support better MT value in CG92 include high resistivity, low impurity levels, narrow Te inclusion size distribution range, and total population density of Te inclusions <650,000 in a 0.22 cm^3 (assuming the detector thickness is roughly 2 mm). In fact, the total density of these 3 detectors in CG92 with MT value close to or > $2x10^{-3}$ cm^2/V is almost the same as that of CG64. However, the volume % and average diameters are further apart.

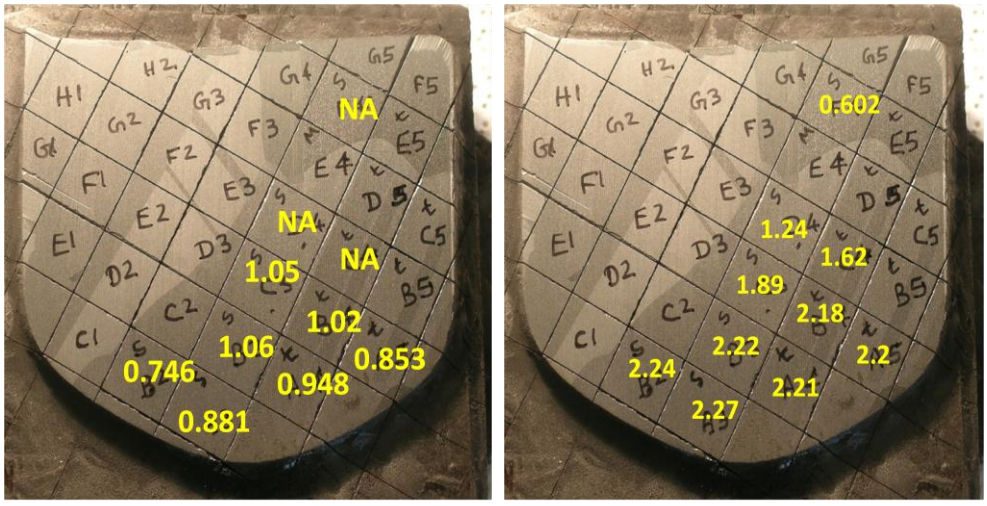

Figure 21: Both are CG93.BC.CD.2 Slice. The left values are tested MT ($*10^{-3}$ cm^2/V) values for respective sample cut. The right values are tested resistivity ($*10^{10}$ Ω.cm) values. [Courtesy of CMR]

Figure 21 above shows a number of detectors which were tested for MT and resistivity values from CG93 slice. The resistivity of detectors cut at a region close to the tip was relatively uniform. The drop in value from 2-1 (*10^{10} Ω.cm) at a region close to the mid of the ingot may be associated with increasing population density of line defects described above. The effects of Te inclusion SSD were studied in CG93.BC.CD.1 slice which was

Courtesy of CMR

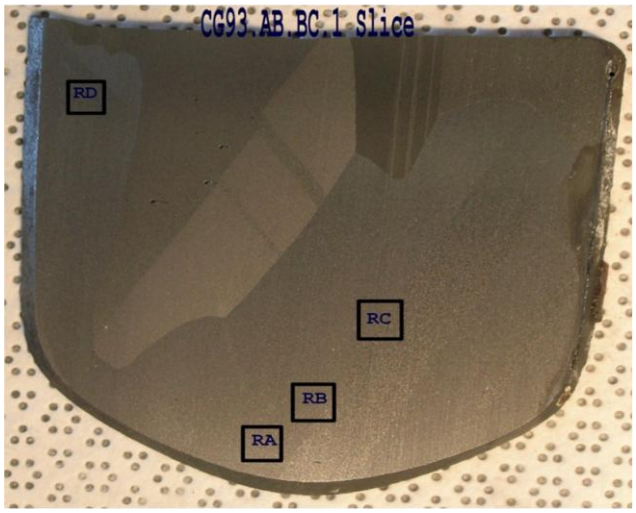

Figure 22: CG93.BC.CD.1 Slice. Selected AOI (0.24 cm^2). AOI include RA, RB, RC, and RD. Line defects are seen through the ingot, but are dominant at a region closer to RC (mid of the ingot)

Table 23: CG93.BC.CD.1 Slice_(RA,RB,RC,&RD) SSD results. RC SSD is first calculated using the regular procedure and it estimates these lines to be spherical. Line defects are given 2D dimension and their SSD is calculated as small rectangles.

	Count	Den	Den >4um	$Den_{<4um}/Den_{Total}$	Vol %	Vol % >4um	Ave D	Ave D
RA	6243	94749	57278	40 %	0.0087	0.0086	7.69	11.16
RB	14989	227486	39930	82 %	0.0096	0.0094	3.52	8.56
RD	15702	238838	59291	75 %	0.0051	0.0049	3.72	7.03
RC	43405	660219	174695	74 %	0.0067	0.0061	3.62	6.37
Units	#	#/cm3	%	Um	um			
	Count	**Den**	**Vol %**	**Ave. Width**	**Ave. Length**			
RC (2)	8355	1083003	0.1	2.17	4.41			

a cut close to CG93.BC.CD.2. Regions studied in BC.CD.1 slice include RA, RB, RC, and RD (figure 22). Region RD is not reported in this thesis as MT values were not tested for detectors

extracted at a region closer to it. IR results for regions studied in slice BC.CD.1 are given in table 23.

Table 24(a) gives an average of BC.CD.2 detector properties overview which can be correlated to Te inclusions SSD of BC.CD.1 slice. A single DOF image from RC is given in figure 23. The number of regular Te inclusions is far less than the number of line defects. These defects are scattered throughout the image with no oriented direction. These lines are not sufficiently elongated along the growth direction to be a crack or an outline of an inclusion; they might be dissolved Te inclusions along a micro-channel.

Table 24(a): Averages for CG93.BC.CD.1 Slice(RA&RB)	
MT(1.5 shaping)	**0.93E-03**
Resistivity	**1.89E+10**
P/V ratio	**Nil**
Vol % (%)	**0.0078**
Vol % >4um	**0.0077**
Den (Counts/cm^3)	**121946**
Den >4um	**47662**
$Den_{<4um}/Den_{Total}$ %	**65 .0%**
$Den_{>4um}/Den_{Total}$ %	**35.0 %**
Ave D (um)	**4.74**
Ave D >4um	**10.05**

GDMS report given in the APPENDIX B, shows a decline in purity level in ingot 92 compared to 93. A significant increase of Si, O, and Na in CG93 compared to CG92 within the mid is given in APPENDIX B as well. This affected the crystal properties and corrupted the projected correlation especially of detectors extracted from a region close to AOI RB, whose $Den_{<4um}/Den_{Total}$ is ~ 80 % [table 23]. Detector B2 in figure 20, which is extracted from a region close to RB had a MT value of $1.06*10^{-3}$ cm^2/V cm^2/V instead of a value ~ $2.00*10^{-3}$ cm^2/V.

In addition, the effect of defect lines explained earlier in detector 92_D3 is very much present in most detectors cut from the mid of the ingot. Figure 22 shows these line defects which seem to have no form of identified orientation. Their standard volume % is given in table 24(b)

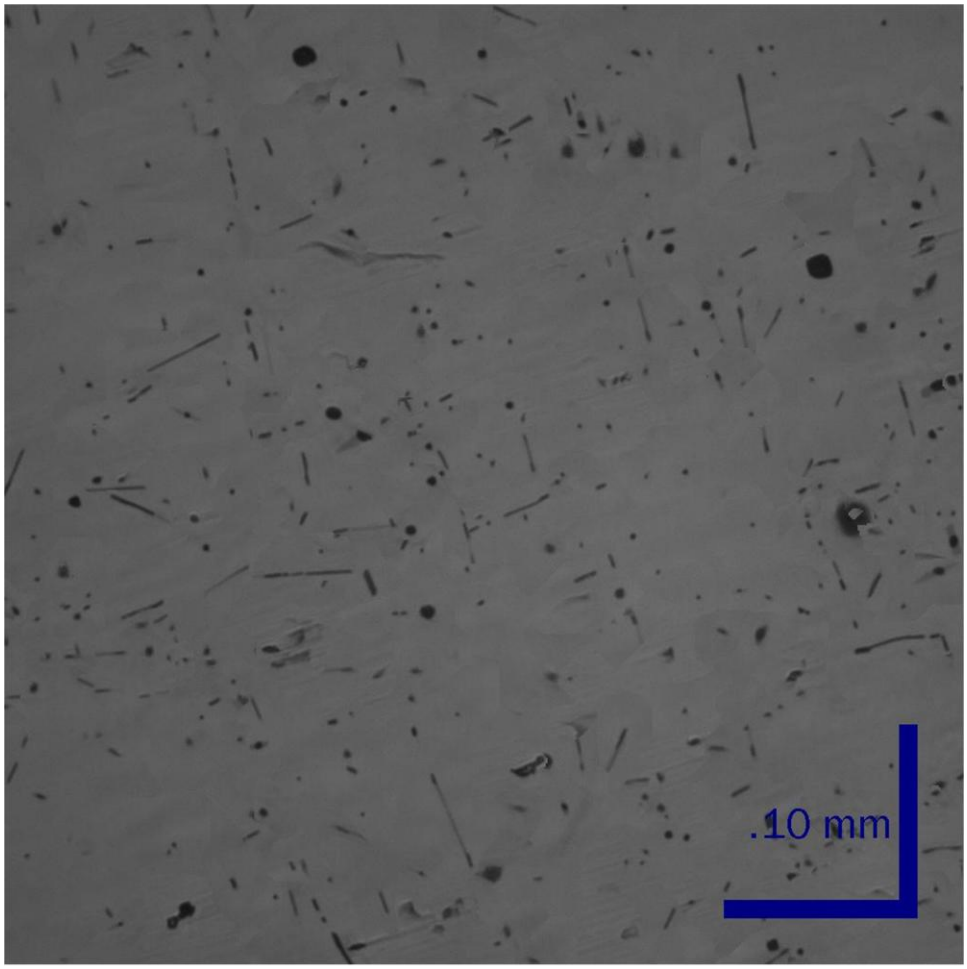

Figure 23: Single DOF image from AOI_RC . The number of regular Te inclusion is far less than that of line defects. These defects are scattered throughout the image with no oriented direction. These lines are not elongated along the growth direction (the image was taken perpendicularly to the growth direction). These defects are suspected to be dissolved Te inclusions along a micro-channel

as 0.1 % which is extremely high compared to normal calculated volume % of RC which assumes these lines to be spherical (see table 23). The impact of these line defects, which have a

higher surface area to volume ratio is more delicate and tends to completely block electron mobility in a CZT detector. As shown in figure 21, those detectors close to RC are nullified. They include C4, D4, and F4 (table 23). As mentioned earlier, a current fluctuation during ingot growth at this mid point is a strongly causative factor which triggers these named flaws.

Detectors close to the tip, A3-B2, reported a lower MT value ($<1x10^{-3}$ cm^2/V) [table 23]. These regions were relatively free from discussed defect lines. However, a drop in

$Den_{<4um}/Den_{Total}$, close to 40 %, at this AOI may have contributed to this negative effect. The SSD properties of this section match those of CG78 or CG80 detectors. Detector B2-C3 reported a value approximately close to $1x10^{-3}$ cm^2/V. This is because of a decrease in average diameter, but with a mix of line defects which may have attracted impurities susceptible to trapping electrons.

Table 24(b): Averages for CG93.BC.CD.1 Slice_RC

MT(1.5 shaping)	Nullified
P/V Co-57	Nil
Vol %	0.1
Den	1083003
Den % of line defects	>80%
Average width (um)	2.17
Average length (um)	4.41

CHAPTER 6

CONCLUSION

Table 25: CG(64,59,78,80,92,&93) growing condition, MCA, and SSD overview. C-D stand for cool down period in hrs; T-G stand for total time of growth in hrs. ExTe ~ Excess Te

CG	64_E	64_B3	59_C2	59_H5	78_13	78_44	80_Slice	92_A3	92	93_RA
CdTe (g)	1267.3		1267.3		1267.3		1267.3	1836		1836
ZnTe (g)	0		0		0		0	164		164
Zn (g)	38.37		38.37		38.37		38.37	5.6		5.6
Te (g)	78.86		78.86		78.86		78.86	108.5		108.5
ExTe (%)	0		0.5		0.5		0	0		0
Ex Cd (g)	0		0		0		0	0.2137		0.2137
In (ppb)	5000		5000		5000		7000	7500		7500
C-D (hrs)	RQ ~ 23.74		38.8		HG ~ 267		HG ~ 886	70.71		141.42
T-G (hrs)	441.91		281.53		652.17		1270.2	483.89		552.77
Ave MT		1.50		1.85		1.11	0.65		1.75	0.94
ρ (Ω.cm) ~ $x10^{10}$		2.29		2.63		2.74	2.38		2.08	1.85
MT ~ $x10^{-3}$	8.80	1.48	2.02	0.77	1.55	0.72		2.2	1.5	
ρ (Ω.cm) ~ $x10^{10}$	0.5	1.05	2.64	1.15	2.84	2.21		3.33	1.32	
P/V Co57 ~	Nil	2.16	1.30	1.6	1.67	1.69	Ave 1.15	Nil	Nil	Nil
14 KeV	Good	Good	Good	Good	Good	Fair/Good	fair	Good	Good	Poor
Area (cm^2)	0.31	0.73	0.58	0.71	0.024	0.024	0.024	0.55	0.62	0.04
Vol %	0.0006	0.0041	0.0081	0.0086	0.0074	0.0076	0.0103	0.0044	0.0075	0.0087
Vol % >4um	0.0002	0.0040	0.0075	0.0083	0.0072	0.0075	0.0102	0.0041	0.0071	0.0086
Vol % >6um	0.0001	0.0005	0.0071	0.0082	0.0069	0.0072	0.0101	0.0039	0.0071	0.0086
Vol % <6um	0.0005	0.0036	0.0009	0.0009	0.0004	0.0004	0.0001	0.0005	0.0007	0.0001
Dens ($count/cm^3$)	707,470	805,285	665,349	364,536	283,722	279,061	262,400	335,105	451,953	94,749
$Den_{<4um}/Den_{Total}$ %	99.1 %	69.4 %	81.5 %	77.8 %	53.4 %	50.2 %	29.8 %	82.0 %	76.5 %	39.5 %
$Den_{>4um}/Den_{Total}$ %	0.9 %	30.6 %	18.5 %	22.2 %	46.6 %	49.8 %	70.2 %	18.0 %	23.5 %	60.5 %
$Den_{<6um}/Den_{Total}$ %	99.7 %	97.3 %	89.8 %	87.9 %	68.4 %	65.0 %	33.9 %	91.8 %	87.4 %	52.5 %
Ave D (um)	1.90	4.00	3.46	3.68	5.41	5.77	7.38	3.35	3.81	5.94
Ave D >4um	6.17	5.09	7.61	7.83	8.70	8.89	9.54	7.62	7.95	11.52
Size Range (um)	1-6	1-19	1-35	1-60	1.35	1-33	1-22	1-41	1-55	1.39

Table 25 lists a number of studied ingots' growing conditions, detector properties, and Te inclusions' SSD results. Various error bars are estimated as follows: volume % (Vol %) ~ 5-8%, average diameter (Ave D) ~ 5-6%, density (Den) ~ 18-25% and MT value ~ 24%. Besides secondary SSD parameters such as volume %, other parameters such as density, average diameter, $Den_{<4um}/Den_{Total}$% are estimated as well. Other density ratio of inclusions with average diameter <6 to <20, including that of <2 are estimated as well; i.e., the density ratio of inclusions with average diameter is given as $Den_{<6um}/Den_{Total}$% (see table 26).

Table 26: Establishing a Correlation Between $Den_{<?um}/Den_{Total}$ of Selected Detectors and Their Respective MT values given in $*10^{-3}$ cm^2/V; <?um can be <2um, <4um and so on.

Name	<2um	<4um	<6um	<8um	<10um	<12um	<14um	<16um	<18um	<20um	MT
CG64.Edge	56.3	99.1	99.7	99.9	99.9	100.0	100.0	100.0	100.0	100.0	8.8
CG58.BD1.C6	19.8	73.4	85.1	91.0	94.0	96.2	97.8	98.9	99.4	99.7	1.7
CG59.BD1.C5	19.8	81.5	89.8	96.1	97.4	98.1	98.5	98.9	99.2	99.3	2.12
CG78.R2.13	11.2	46.2	56.9	64.2	68.7	81.3	90.7	93.6	96.7	99.1	1.11
CG80.R2 S Ave.	9.0	29.8	33.9	47.1	80.0	90.0	93.7	98.8	99.8	100.0	0.65
CG92.BC.CD2.A3	24.2	82.0	91.8	95.4	97.0	97.9	98.5	98.9	99.3	99.5	2.2
CG93.BC.CD1(RA Ave)	19.3	65.0	75.3	80.0	83.3	87.4	90.8	93.1	94.7	96.1	0.94
CG64.BD2.B3	23.8	30.6	97.3	99.5	100.0	100.0	100.0	100.0	100.0	100.0	1.48

Detectors selected for further plotting: CG80.R2 Slice Average; CG93.BC.CD1 (RA) average; CG58.BD1.C3 (Within the shoulder); CG78.R3 Slice Average; CG59.BD1.C5 (Within the shoulder); CG92.BD2.CD2.A3 (Within the shoulder); and CG64.Edge (Close to shoulder)

A plot of this density ratio fitted in Boltzmann function is given in graph 8 (the error bar for density ratio is relatively 18-23 %, which is a assumed to be that of calculated total density of Te inclusions.) In this plot, $Den_{<2um}/Den_{Total}$% is an outlier and fails to correlate with most tested

MT values of varied detectors at CMR. Starting with $Den_{<4um}/Den_{Total}$% to $Den_{<20um}/Den_{Total}$%, the projected

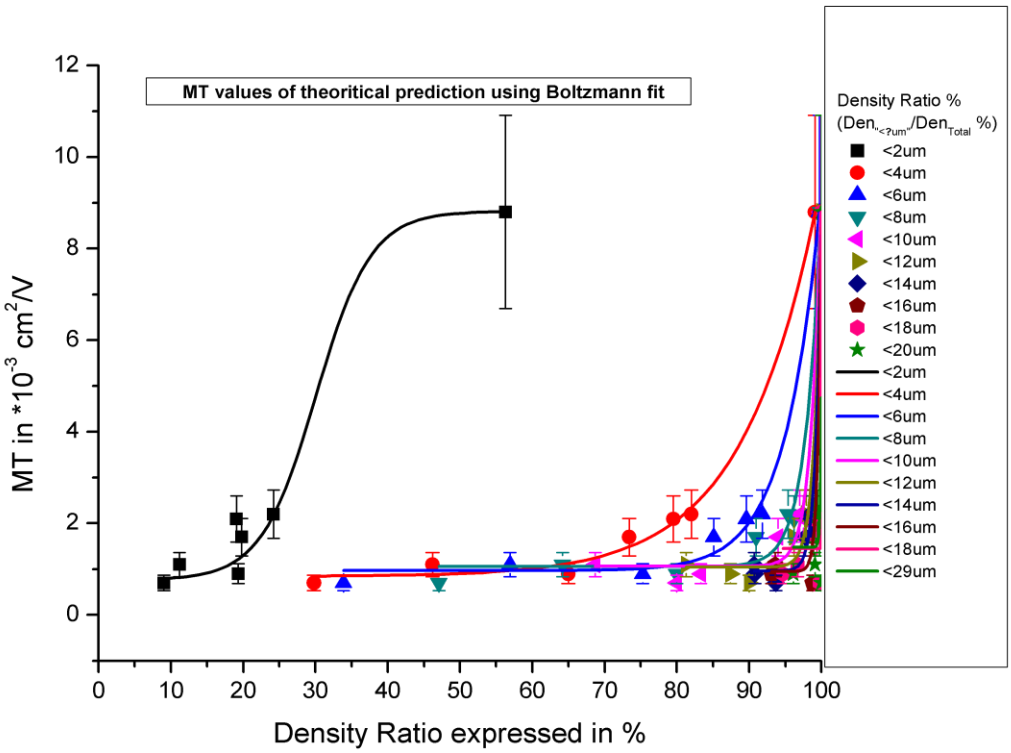

Graph 8: The density ratio of inclusions with average diameter < (2-20) to that of total density of Te inclusions.

correlation takes a common pattern, which seem to converge as the density ratio of bigger inclusion (>4um) is considered. Two curves, that of <4um and <6um seem pertinent to projected MT value. However, it is that of <4um that clearly established a stronger correlation not only to studied inclusion in this thesis, but also to other tested detectors' values. Its plot is given in graph 9. The variation between these two curves, that of <4um and <6um represents those inclusions which may fall in the grey area of 4-5um and may have less of a negative impact on detector's

quality. Boltzmann function fitted in this correlation between $Den_{<4um}/Den_{Total}$% and MT value is indication that detectors properties are limited to unconventional values.

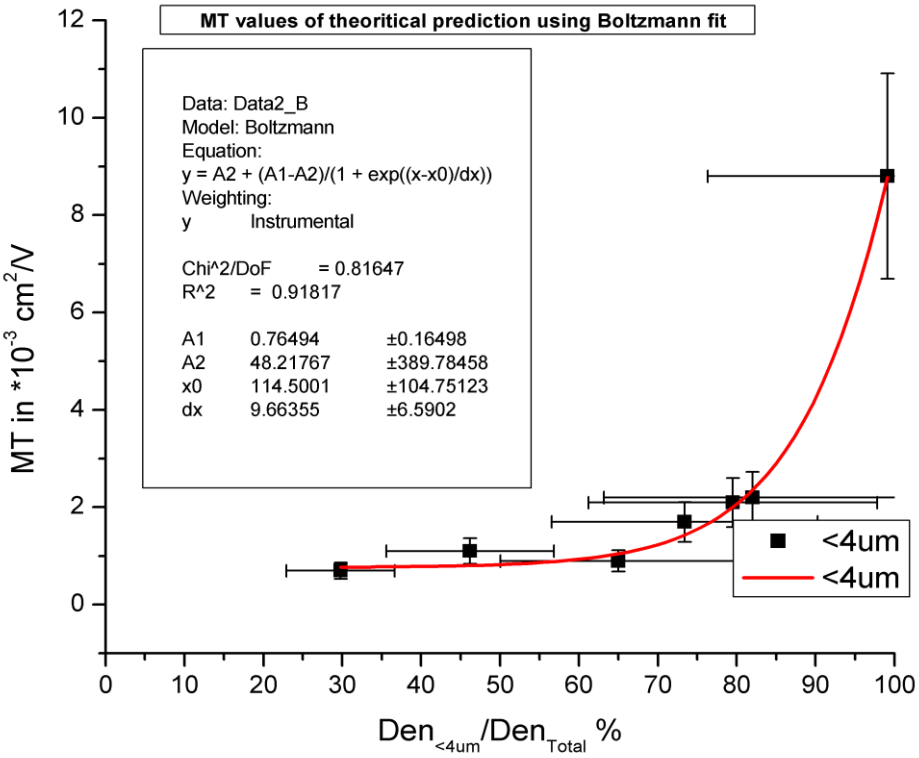

Graph 9: The density ratio of inclusions with average diameter < (2-20) to that of total density of Te inclusions.

For this correlation to work, a list of prerequisites or conditions is set. Fundamental conditions include crystal purity and detector resistivity $>10^9\Omega$.cm. Secondary conditions consist of ingots' growing conditions, which include applicable raw materials and dopants. The amount of raw material and dopants is given in table 25. Note that even though some ingots were grown without addition of excess Te necessary to improve crystal resolution (i.e., CG64), used CdTe charge is reported to be already Te-rich. This explains why Te inclusions'

parameters, like volume % and density ratio, of detectors extracted from those ingots is given. Otherwise detected features in this ingot were rich in voids. Also, remember that this thesis refers to Te inclusions and/or voids as simply "Te inclusions."

Table 27: MT values of theoretical prediction fitted in Boltzmann function. Carried Over % error of 24%.			
Condition 1: Purity (free from impurity ~ GDMS)			
Condition 2: Detector resistivity ~ $>10^{9}$ Ω.cm			
Condition 3: Ingot growing conditions: i.e., raw materials & dopants. Including single crystal			
Favorable in uncluttered and even distribution of Te inclusion. Also favors single crystal detectors and narrow range distribution.			
$Den_{<4um}/Den_{Total}$ %	**MT<**	**MT**	**<MT**
30	0.59	0.77	0.96
35	0.59	0.78	0.96
40	0.60	0.79	0.97
45	0.61	0.80	0.99
50	0.63	0.82	1.02
55	0.66	0.87	1.07
60	0.71	0.93	1.16
65	0.80	1.05	1.30
70	0.94	1.23	1.53
75	1.18	1.55	1.92
80	1.57	2.06	2.56
85	2.21	2.91	3.60
90	3.23	4.25	5.27
95	4.81	6.33	7.85
100	7.16	9.42	11.68

Another favorable condition is that of uncluttered and even-narrow distribution of Te inclusions throughout a detector. However, if the majority of Te inclusions have an average diameter >4um, the detectors' MT value decreases; i.e., detectors from CG78 ingot. Simulated values of projected correlation between $Den_{<4um}/Den_{Total}$% and MT values is given in table 27.

Table 28: MT values of theoretical prediction fitted in Boltzmann function. Carried Over % error of 24%.			
Condition 1: Purity (free from impurity ~ GDMS)			
Condition 2: Detector resistivity ~ $>10^{9}$ Ω.cm			
Condition 3: Ingot growing conditions: i.e., raw materials & dopants. Including single crystal			
Favorable in uncluttered and even distribution of Te inclusion. Also favors single crystal detectors and narrow range distribution.			
$Den_{<6um}/Den_{Total}$%	MT<	MT	<MT
30	0.63	0.83	1.03
35	0.63	0.83	1.03
40	0.63	0.83	1.03
45	0.63	0.83	1.03
50	0.63	0.83	1.03
55	0.63	0.83	1.03
60	0.64	0.84	1.04
65	0.64	0.84	1.05
70	0.66	0.86	1.07
75	0.69	0.91	1.13
80	0.79	1.04	1.28
85	1.02	1.34	1.66
90	1.60	2.10	2.61
95	3.03	3.98	4.94
100	6.53	8.59	10.65

These predicted values were tested on other detectors from ingots grown at CMR and not studied in this project and the results were positive. Another simulated values of projected correlation between $Den_{<6um}/Den_{Total}$% to MT values given in table 28 fails to predict precise results. As $Den_{<6um}/Den_{Total}$% increases, MT values converges.

So far, it is evident that these accumulative SSD analyses of Te inclusions and/or voids establish a concrete characteristic of Te inclusions present in detectors at CMR. In retrospect, there is a strong correlation between the presence of Te inclusions and MT values of CMR-processed detectors. This correlation exists in samples that are single crystals, high resistivity ($>10^9\Omega$.cm) and partially free from impurity (according to GDMS report given in APPENDIX B, all tested ingots reported a measurable amount of impurity). Single crystals are free from notable extended defects such as grain boundaries, cracks, voids, pipes, and wires which not only increase the concentration of Te inclusions, but also increase the concentration of foreign impurities [20]. Keep in mind that it is hardly possible to make a detector which is 100% single crystal; one can only create a detector in which the named defects are only present in small percentages. The same applies to analyzed impurities as given by GDMS report. The presence of these minor defects accounts for distribution instability and non-uniform orientation of Te inclusions and/or voids. Foreign impurities and oversaturation of native defects due to a poor compensation scheme supply extra charges which increase the leakage current hence reducing resistivity and MT values. A high concentration of Te inclusions acts as an impurity sink, which traps charges hence increasing their residency time and destabilizing the Fermi level. This inhibits electron mobility, resulting in low MT value.

A working correlation within an ingot is favored when one considers the size distribution which seems to widen predictably from the tip of the ingot to the heel. In conjunction with reduction of Zn concentration which lowers resistivity, MT value decreases towards the heel as well. An increasing size range as a result of formation of bigger inclusions impinges a strong attraction of impurities that increasingly inhibits electron mobility and lowers the MT values.

Keep in mind high concentrations of Te precipitates remain unconfirmed within and around the heel of the ingot. On the other hand, a working correlation from ingot to ingot is established between detectors that are extracted within and around the shoulder, but not the heel, whose resistivity is high and approximately the same. This uniformity in detectors' properties is exposed in the light of detectors cut from a CG78.R2 radial slice within the shoulder.

Parallel to characterizing Te inclusions, study of Te inclusion evolution from CCG78 and CG80 SSD analysis gave no concrete information that can help to correlate the shape of its inclusions to its MT values. This is probably because CMR uses a 2D analysis technique to characterize Te inclusions and the viewable image is not a true representation of the shape of the inclusion. Hence, an advanced software capable of categorizing the shape of inclusions is necessary to tabulate frequencies of various shapes and their volume % or $Den_{<4um}/Den_{Total}$% of relative densities that can be associated with their respective MT values. Another feature adjoined to Te inclusion is voids. Their presence seems realistic and proceedings from SNRL support this. Their effect is intertwined with the characterization of Te inclusions and demands coupling analyses which contribute to this discovered correlation.

Another relevant factor that continues to hinder full realization of Te inclusions' characteristics and their correlation with MT value is poor understanding of Te precipitates, Zn and Cd secondary phases, and standard measures of foreign impurities as reported by GDMS report. In reference to Te precipitate, an advanced technology which is capable of acquiring and displaying images at the nano-level scale is necessary. More importantly, a more advanced technology capable of acquiring features of less than <1 um and distinguishing them from much larger features is critical to the full realization of Te inclusion characteristics.

Conclusively, Te inclusions are a litmus test that can predict:

1.) An effective stiochiometry with a balanced reaction of Te with Cd and Zn during growth

2.) Given an effective stiochiometry, an effective compensation scheme is established between Te_{Cd} and stable In_{Cd}.

3.) An effective reaction of Cd with excess Te to form CdTe during cool-down in Cd-rich grown ingot

The consequences of the above event during both growth and cool-down of the ingot can result in different SSD of Te inclusions with varied effects as follows:

1.) Formation of inclusions >4um with wide distribution which suggests that the litmus test failed in parts and at times entirely throughout the ingot. Imposed cooling period may have allowed growth to take place resulting in increased size of Te inclusion and/or voids.

2.) Formation of inclusions >4um with narrow distribution that suggests that the litmus test partially worked, but extended cooling time may have allowed for prolonged transformation of Te solvents and linked voids which led to transformation of bigger inclusions and/or voids.

3.) Formation of smaller inclusions <4um with narrow distribution (size range 1-4) suggests that the litmus test worked. Less transformation of Te solvent to inclusions took place because of controllable amount of Te, less cooling time, and low diffusion rate.

Most of all, the majority of Te solvents was successfully used in reaction of Zn and Cd during cool-down.

4.) In case of test (3) above, reaction of Cd with excess Te in Cd-rich grown ingot is necessary as it results in the formation of CdTe which integrates into CZT matrix resulting in low transformation of Te inclusions and voids. It is necessary, however, to maintain low concentrations of V_{Cd} and Cd inclusions as its increasing frequency will completely ruin a detector.

The third result given above is developed from the ideal result comparable to that of CG64 Edge sample which became a success at CMR. A detector which adhered to effect (2) of Te inclusions with MT value $<10^{-3}$ cm^2/V confirms the impact of Te inclusions with average diameter >4um as severe. Finally, SSD results of various detectors from the same ingot established a correlation between size range distribution of Te inclusion and MT values. Collective SSD results, bounded by conditions such as purity and resistivity, from detectors cut within and around the shoulder of various ingots at CMR establish a correlation between $Den_{<4um}/Den_{Total}$% and MT values. In essence, there is finite range between the lowest and the highest measurable MT value. The lowest MT value has been set, but the highest is still inaccessible due to other factors such as acute compensation of charges, acute stiochiometry, and technical variation experienced during growth. Last, but not least, Te inclusions are characterized as: (1) <4um ~ litmus test to effective stiochiometry and subsequent favorable compensation scheme necessary in improving detector's performance; (2) >4um ~ inhibitors to electron lifetime, which lowers the MT value (weaken detector's performance).

CHAPTER 7

RECOMMENDATION

Maximization of MT values lies in regulation of Te used in growth of CZT ingots. So far, we have managed to regulate Te inclusions in CZT to $Den_{<4um}/Den_{Total}$ >80%. The distribution is still relatively wide and it must be narrowed. The total density of Te inclusions is still relatively high and must be decreased in conjunction with size reduction to <4um. An effective measure of dopants and raw material is critical, but the an effective cool-down technique will finally bring this project one step closer to full realization of high MT value. A low diffusion rate of inclusions in a fast cool-down ingot has decreased transformation rates of inclusions, hence reducing their size. This can result in better MT values, especially when more than 95% of Te inclusions present in CZT have a diameter range <4um.

REFERENCES

1. Schlesinger, *et al.* (2001). Cadmium Zinc Telluride and Its Use as a Nuclear Radiation Detector Material. *Material Science & Engineering, 32,* 103-189.

2. C. Braggio, *et al.* (2006). Massive Silicon or Germanium Detectors at Cryogenic Temperature. *Nuclear and Methods in Physics Research, 568(A),* 412-415.

3. A.E. Bolotnikov *et al.* (2007). Effects of Te Inclusions on the Performance of CdZnTe Radiation Detectors. *IEEE Nuclear Science Symposium Conference Record, N27-2,* 1788-1797

4. A.E. Bolotnikov. *et al.* (2009). Extended Defects in CdZnTe Radiation Detectors. *IEEE Transactions on Nuclear Science, 4(56),* 1775-1783.

5. K.G. Lynn. *et al.* (2008-2009). View Graph Presentations. Proceedings from Savannah River National Lab. Retrieved from Center for Material Research (CMR) at Washington State University.

6. A.E. Bolotnikov. *et al.* (2007). Cumulative Effects of Te precipitates in CdZnTe Radiation Detectors. *Nuclear Instruments and Methods in Physics Research, 571 (A),* 687-698

7. M. Chu *et al.* (2003). Effects of Excess Tellurium on the Properties of CdZnTe Radiation Detectors. *Journal of Electronic Materials,* 32(7), 778-782

8. M. Fiederle *et al*. (2003). Growth of High Resistivity CdTe and (Cd,Zn)Te Crystals. *Cryst. Res. Technol., 38(7-9),* 588-597.

9. Tewari, A., & Gokhale, A.M. (2000). Estimation of Three-Dimensional Grain Size Distribution from Microstructure Serial Section. *Material Characterization, 46,* 329-335.

10. Rustom, *et al.* Low Temperature Thermal Annealing of Detector Grade CdZnTe (CZT) Crystals. *Physics Department, Fisk University, 1-76.*

11. G. Li. *et al.* (2004). Characteristics of Doped Indium in $Cd_{0.9}Zn_{0.1}Te$ Grown By the Bridgman Method. *Semicond. Sci. Technol*. 19, 457-460.

12. Institute for National Measurement Standards. (2007-2009). *Glow Discharge Mass Spectrometric Report (GDMS) - ppb(atomic).* Lancaster, Canada: A. Mykytiuk & B. Methven.

13. J.W. Carson, *et al.* (1986). Understanding and Eliminating Particle Segregation Problems. *Jenike & Johanson Incorporated International, 6(1),* 139-144.

14. S. Terterian *et al.* (2004). Distribution of the High Resistivity Region in CdZnTe and Its Effects on Gamma-Ray Detector Performance. *Journal of Electronic Materials, 33(6),* 640-643.

15. C. H. Henager Jr *et al*. (2009). Preferential Orientation of Te Particles in Melt-Grown CZT. *Journal of Crystal Growth,* 311, 2641-2647.

16. K.A. Jones. (2009). Optimization of Cadmium Zinc Telluride Crystals Growth for Room Temperature Radiation Detector. (Doctoral dissertation, *Washington State University,* 2009)

17. A. Triboulet. (2005). Fundamentals of the CdTe and CdZnTe Bulk Growth. *Phys. Stat. Sol, 2(5),* 1565-2005.

18. V. Babentsov *et al.* (200(9). Characterization of Compensation and Trapping in CdTe and CdZnTe: Recent Advances. *Crystal. Res. Technol, 44(10),* 1054-1058.

19. S. Kumar. (2006). Effects of Subtrate Dislocations on the Hg in-Diffusion in CdZnTe Substrates used for HgCdTe Epilayer. *Growth Journal of Crystal Growth, 297,* 311-316.

20. R.B. James *et al.* (1998). Material Properties of Large-Volume Cadmium Zinc Telluride Crystals and Their Relationship to Nuclear Detector Performance. *Journal of Electronics Materials, 27(6),* 788-799.

21. G. Yang (2009). Internal Electric Field Investigations of a Cadmium Zinc Telluride Detector Using Synchrotron X-ray Mapping and Pockels Effect Measurements. *Journal of Electronics Materials, 38(8),* 1563-1567.

22. V. Babentsov *et al.* (2009). Compensation and Trapping in Large Bandgap Semiconductors: Tuning of the Defect System in CdZnTe. *Journal of Crystal Growth, 311,* 2377-2380

23. G. Yang *et al.* (2008). Impurity Gettering of Te Inclusions in CdZnTe Single Crystals. *Journal of Crystal Growth, 311,* 99-102.

24. C.R. Barret, W.D. Nix, & A.S. Tetelman. (1973). *The Principles of Engineering Materials,* Chapter 5. Englewood Cliffs, NJ: Prentice-Hall, Inc.

25. S Hu. *et al.* (2009). Phase-field Simulation of Te-Precipitate Morphology and Evolution Kinetics in Te-rich CdTe Crystals. *Journal of Crystal Growth, 311,* 3184-3194.

26. A. Castaldini *et al.* (1998) Deep Energy Levels in CdTe and CdZnTe. *Journal of Applied Physics,* 4(83), 2121-2126

27. Carvalho *et al*. (2009). Intrinsic Defects in CdTe and CdZnTe Alloys. Physics B, 404, 5019-5021.

28. S.A. Awadalla *et al.* (2010) Characterization of Detector-Grade CdZnTe Crystals Grown by Travelling Heater Method (THM). *Journal of Crystal Growth, 312*, 507-513.

29. B Faulkner. (2009). *Thermomigration of Tellurium Inclusion in CZT*. Property of CMR.

30. Media Cybernetics, Inc. (2006). *Image-Pro Plus: The proven Solution for Image Analysis*. Silver Spring, MD: MediaCyberanatics.

31. Edmund Optics. (2000). *Calibration Data: PN 59273*. Barrington, NJ: Edmund Optics Inc.

32. A. Yeckel & J.J. Derby. (2005). Bridgman Growth of CZT: Axisymetric Analysis. In P. Capper (Ed). *Bulk Crystal Growth of Electronic, Optical & Optoelectronic Materials*, (102-104). West Sussex, England: John Wliey & Son Ltd.

APPENDIX

APPENDIX A: GROWTH DETAILS

GROWTH	CG51	CG58	CG59	CG67	CG78	CG80	CG92	CG93
Date	7/09-21/2007	01/24/08-02/05/08	02/15-27/2008	7/14-26/2008	12/18/09-1/08/10	1/15/10-2/07/10	12/18/09-1/08/10	1/15/10-2/07/10
Charge (g)	1387.5	1387.46	1387.45	1387.46	2000	2000	2000	2000
Composition %Zn	Cd0.9Zn0.1Te	Cd0.9Zn0.1Te	Cd0.9Zn0.1Te	Cd0.9Zn0.1Te	Cd0.9Zn0.1Te	Cd0.9Zn0.1Te	Cd0.9Zn0.1Te	Cd0.9Zn0.1Te
Raw Material	CdTe, Te, Zn	CdTe, Te, Zn	CdTe, Te, Zn	CdTe, Te, Zn	CdTe, Te, Zn	CdTe, Te, Zn	CdTe, ZnTe, Te, Zn	CdTe, ZnTe, Te, Zn
Excess Te	0.50%	0.50%	0.5%	0.50%	0.5%	0	0	0
Excess Cd	0	0	0	0	0	0	0.2137g (Cd)	0.2133g (Cd)
Dopants ppb	In ~ 5000	In ~ 5000	In ~ 5000	In ~ 5000	In ~ 5000	In ~ 5000	In ~ 7500	In ~ 7500
Growth rate	Variable mm/hr, 70C/inch	Variable mm/hr, 70C/inch	Variable mm/hr, 70C/inch	Variable mm/hr, 70C/inch	0.55mm/hr, 50C/inch	0.55mm/hr, 50C/inch	0.55mm/hr, 50C/inch	0.55mm/hr, 50C/inch
Cool Down (985C)	38.8hrs	38.8hrs	38.8hrs	38.8hrs	70.71 hrs	141.42	70.71 hrs	141.42
Time after growth in furnace	52.25hrs	16.17hrs	20hrs34mins	24hrs	N/A	N/A	N/A	N/A
Time of growth	281.48hrs	282.42hrs	281hrs32mins	281.48hrs	483.89 hrs	552.77	483.89 hrs	552.77
Ampoule Devitrification	0.75	0.75	0.75	2	1.25	1	1.25	1
Deposit	0.14%	0.14%	0.11%	N/A	0.01%	0.60%	0.01%	0.60%
Length	91.4mm	90mm	90mm	91.5mm	88.3mm	82.6mm	88.3mm	82.6mm
								Courtesy of CMR

APPENDIX B: GROWTH IMPURITIES

Ingot	CG51			CG58			CG59			CG64			CG67			CG78		CG80		CG92		CG93		
	T	M	H	T	M	H	T	M	H	T	M	H	T	M	H	T	H	T	H	T	H	T	M	H
X/Xo Ingot	0.306	0.514	0.886	0.388	0.666	0.9	0.378	0.644	0.889	0.378	0.597	0.816	0.319	0.572	0.825	0.52	0.90	0.33	0.81	0.516	0.9	0.33		0.81
Li	0	6	20			4												<2	<2	19	5	20	<2	<2
B				91														<4	<4	<4	<8	<3	<5	<4
C	110	30	120	22	11	90	120	35	16	80	260	65	130	75	130	330	220	8	15	180	50	250	290	260
N	10	140	25	9	10	14	30	5	3	4	25	7	1	2	3	11	8	1	5	8	45	60	40	30
O	90	45	130	230	130	200	360	80	100	100	250	90	120	100	220	240	250	50	30	110	170	610	600	420
Na	0	71	180	0	0	10				180	140	110	0	14	42	33	36	5	<3	99	36	79	260	59
Mg	24	12	13	92	72	47	38	30	40	44	22	45	57	42	21		16	92	21	13	<6	35	14	8
Al	210	370	970	720	1600	2400	57	56	140	11	800	1400	14	25	28	11	42	32	52	26	42	27	410	65
Si			40	5	13	7				6	0	0	0	0	6		19	6	23	<3	46	<3	3400	17
P																		<2	<1	<2	7	<2	9	8
S			78	0	72	61	93	40	52	50	0	0	0	0	36	56	93	11	54	<10	42	<25	<25	<25
Cl			20	0	8	11	18	10	0	15	9	12	0	0	0	18	40	10	38	<4	<10	<6	240	23
K																		<15	<15	<50	<45	<100	<130	<160
Ca																		<20	<15	<15	<45	<50	<40	<35
Sc	0	0	0	0			0	0	0	0			0				0	<0.5	<0.5	<0.5	<1	<1	<0.8	<0.6
Ti	0	0	2	0	0		0	0	0	0			0				0	<0.5	<0.4	<0.4	<0.9	<0.4	3	<0.4
V	0	0	0			0	0	0	0	0			0				0	<0.3	<0.3	<0.3	<0.6	<0.9	<0.4	<0.3
Cr	0	0	0	0	4	3	0	0	0	0			0				0	<5	<2	<2	<15	<5	<5	42
Mn	0	0	0			0	0	0	0	0			0				0	<10	<10	<10	<10	<10	<10	<10
Fe	0	0	64	0	30	0	0	0	55	0			29	67	71	0	74	45	24	<5	140	<5	<5	<5
Co	0	0	0			0	0	0	0	0			0				0	<0.5	<0.5	<0.6	<1	<0.9	<0.9	<0.6
Ni	0	0	0	0	0	11	0	0	0	0			0				0	<3	<2	<3	<8	<4	<4	65
Cu	0	0	130	0	37	0	0	0	0	0			0				0	<20	<10	<25	<30	<15	<40	160
Ge	0	0	0			0	0	0	0	0			0				0	<30	<50	<30	<25	<25	<30	<20
As						0	0	0	0	0			0				0	<15	<15	<20	<25	<25	<25	<50
Se	0	30	0	25	0	0			0	0			0	30	80		0	<10	<10	<15	<30	<15	<15	<15
Y	0	0	0			0			0	0			0				0	<0.2	<0.2	<0.2	<0.4	<0.9	<0.3	<0.3
Nb	0	0	0			0			0	0			0				0	<0.4	<0.4	<0.2	<0.4	<2	<0.3	<0.3
In	1400	2800	22000	1400	2900	7200	1400	2800	8600	5400	1400	1800	1100	2400	7900	2300	8700	3900	11000	2400	22000	1600	2600	8500
Sn	0	0	0			0			0	0			0			0	0	<20	<20	<30	<40	<45	<35	<25
Pt	0	430	0	0	0	0	0	0	0	0			0			0	0	<5	<3	<15	<15	<7	<9	<3
Pb					140					0			0			0	0	<1	<0.9	<0.9	<2	<2	<1	<1
Bi	0	0	0	0	0	0	0	0	0	0			0			0	0	<0.6	<0.6	<0.6	<1	<0.9	<1	<0.7
Zn %	5	3.2	2.3	6.8	5.4	3.8	6.2	4.1	2.8	4.3	5.1	5.2	4.6	4.2	3.3	4.1	4.1	5.2	4.0	4.1	2.1	7.7	4.2	2.9

Impurities in ppb with (+/-) 5 uncertainty. T ~ Tip of the ingot, M ~ middle, and H ~ heel.

Courtesy of CMR